Spring 2019

# Hardware architectures for compact microwave and millimeter wave cameras

Matthew Jared Horst



Department: Electrical and Computer Engineering

# HARDWARE ARCHITECTURES FOR COMPACT MICROWAVE AND MILLIMETER WAVE CAMERAS

by

MATTHEW JARED HORST

A DISSERTATION

Presented to the Faculty of the Graduate School of the

MISSOURI UNIVERSITY OF SCIENCE AND TECHNOLOGY

In Partial Fulfillment of the Requirements of the Degree

DOCTOR OF PHILOSOPHY IN ELECTRICAL ENGINEERING

2019

Approved by

Dr. Reza Zoughi, Advisor
Dr. Mohammad T. Ghasr
Dr. R. Joe Stanley
Dr. Daryl Beetner
Dr. Akim Adekpedjou

## PUBLICATION DISSERTATION OPTION

This dissertation consists of the following three papers, formatted in the style used by the Missouri University of Science and Technology, listed as follows:

Paper I (pages 16-40), M. Horst, M.T. Ghasr, and R. Zoughi, "Effect of instrument frequency uncertainty on wideband microwave synthetic aperture radar (SAR) images," IEEE Transaction on Instrumentation and Measurement, vol. 68, no. 1, pp. 151-159, Jan. 2019. DOI: 10.1109/TIM.2018.2834098

Paper II (pages 41-76), M. Horst, M.T. Ghasr, and R. Zoughi, "Design of a compact V-band transceiver and antenna for millimeter wave imaging systems," accepted for publication in IEEE Transaction on Instrumentation and Measurement, 2018.

Paper III (pages 77-116), M. Horst, M.T. Ghasr, and R. Zoughi, "A compact microwave camera based on chaotic excitation synthetic aperture radar (CESAR)," under review in IEEE Transaction on Antennas and Propagation, 2018.

## ABSTRACT

Millimeter wave SAR imaging has shown promise as an inspection tool for human skin for characterizing burns and skin cancers. However, the current state-of-the-art in microwave camera technology is not yet suited for developing a millimeter wave camera for human skin inspection. Consequently, the objective of this dissertation has been to build the necessary foundation of research to achieve such a millimeter wave camera. First, frequency uncertainty in signals generated by a practical microwave source, which is prone to drift in output frequency, was studied to determine its effect on SAR-generated images. A direct relationship was found between the level of image distortions caused by frequency uncertainty and the product of frequency uncertainty and distance between the imaging measurement grid and sample under test. The second investigation involved the development of a millimeter wave imaging system that forms the basic building block for a millimeter wave camera. The imaging system, composed of two system-on-chip transmitters and receivers and an antipodal Vivaldi-style antenna, operated in the 58-64 GHz frequency range and employed the $\omega$-$k$ SAR algorithm. Imaging tests on burnt pigskin showed its potential for imaging and characterizing flaws in skin. The final investigation involved the development of a new microwave imaging methodology, named Chaotic Excitation Synthetic Aperture Radar (CESAR), for designing microwave and millimeter wave cameras at a fraction of the size and hardware complexity of previous systems. CESAR is based on transmitting and receiving from all antennas in a planar array simultaneously. A small microwave camera operating in the 23-25 GHz frequency was designed and fabricated based on CESAR. Imaging results with the camera showed it was capable of basic feature detection for various applications.

# ACKNOWLEDGMENTS

First, I would like to thank my wife Astrid Horst for her dedication and optimism over the course of my graduate career. Her encouragement helped me during difficult times, and I cannot say I would have completed my research without her.

I would like to thank my advisor, Dr. Reza Zoughi, for providing me with the resources to pursue a career in science and engineering. I would also like to thank him for his enduring support during my bachelor's, master's, and doctoral degree programs at Missouri University of Science and Technology.

I would also like to thank Dr. Mohammad Tayeb Ghasr for his overall guidance during my graduate career and for mentoring me in design engineering. Thank you to Dr. Stanley, Dr. Beetner, and Dr. Adekpedjou for serving on my committee and for assisting me with my research endeavors.

Thanks to the National Science Foundation for awarding me with the Graduate Research Fellowship. I would also like to thank Mrs. Joni Matlock, Mrs. Carol Lay, and Mrs. Erin Karr for their administrative support with my Graduate Research Fellowship and for their logistical support during my graduate career.

Thanks to Mr. Jeffrey Birt for his machining services. His manufacturing capabilities helped create the imaging hardware presented in this dissertation.

Thank you to all of my colleagues at the Applied Microwave Testing Laboratory (*amntl*), both present and alumni, for your guidance and support.

Finally, I would like to thank my family and friends for their love and support.

# TABLE OF CONTENTS

# LIST OF ILLUSTRATIONS

Figure Page

PAPER I

PAPER II

PAPER III

# LIST OF TABLES

Table Page

PAPER I

# 1. INTRODUCTION

## 1.1. MICROWAVE AND MILLIMETER WAVE IMAGING

Microwaves and millimeter waves are signals that span the 300 MHz – 30 GHz and 30 GHz – 300 GHz frequency ranges of the electromagnetic spectrum, respectively [1]. Interactions between microwaves and millimeter waves and physical materials are governed by the dielectric constant of the material, which is a complex quantity that determines how electrical energy is stored and lost within a material [1]. The dielectric constant also describes how electromagnetic signals propagate through a material [1]. Due to this property, these signals can be used to detect changes in material composition (e.g., a flaw), even when the dielectric change is contained within a complex multi-layered structured. Microwave and millimeter wave testing has become a major component of nondestructive testing (NDT) for this reason. Nondestructive testing is the field of science where properties of a material are studied and diagnosed without affecting the material's usefulness [2]. In recent years, microwave and millimeter wave NDT has found applications in structural health monitoring, biomedical, aerospace, and security applications [2].

One form of microwave NDT is microwave and millimeter wave imaging (herein referred to as microwave imaging), which is the process of creating a 2D or 3D visual representation of a sample under test (SUT) [2]. In microwave imaging, an antenna or small probe is raster scanned on a measurement grid over a SUT radiating electric fields and measuring the reflections from the SUT. This is referred to as a mono-static imaging configuration. For a bi-static imaging configuration, an antenna raster scans over the SUT, and signals that transmit through are measured on the opposite side of the SUT. For both

configurations, dielectric contrast produces variations in the received electric field. A material with high dielectric constant reflects more of the electric field than a material with a low dielectric constant. Measurements are processed and arranged into a 2D or 3D data structure (i.e., image) identical to the points on the measurement grid, and a gray-scale image is made, where brightness is directly proportional to SUT reflectivity. The benefit of microwave imaging is that it visually shows relative change within a material. The absolute dielectric properties of a material are not required when a flaw can be detected by a change in brightness at its location in the microwave image.

Microwave imaging is subdivided into three categories, namely: near-field imaging, lens-focused imaging, and synthetic aperture radar (SAR) imaging. Near-field imaging is the basic method for generating microwave images. A single antenna is raster scanned on a 2D measurement grid over the SUT, where the SUT is positioned in the near-field of the antenna. The magnitude of the reflection from the SUT is used to create the 2D image. Image resolution is determined by the size of the radiating antenna. Near-field imaging has been employed for surface and sub-surface metal crack detection as well as diagnosis of corrosion precursor pitting [3]-[6].

Lens-focused imaging is a more powerful form of microwave imaging and enables imaging in the far-field of the antenna. Lens-focused imaging is accomplished by placing a dielectric lens between the antenna and SUT, which focuses electric fields to a small location on the SUT. Image resolution is determined by the focal properties of the lens. Lens-focused imaging has been employed for detecting disbonds and voids in spray-on-foam insulation (SOFI) from the external fuel tank of the Space Shuttle [7]-[9]. However,

this imaging methodology is limited to single frequency operation, since the focusing properties of the lens are frequency-dependent.

Synthetic aperture radar (SAR) imaging is the most powerful imaging methodology and allows for the creation of high-resolution 2D and 3D images [10]. Similar to the previous methods, an antenna raster scans over the SUT (typically located in the far-field of the antenna) on a 2D measurement grid. However, for SAR, the measurements must be phase-coherent, such that the recorded data is either a vector (magnitude and phase) or scalar (real or imaginary part) of the complex reflected signal [10]. Additionally, the step size in the measurement grid, otherwise referred to as the electric field spatial sampling interval, is determined by the Nyquist sampling theorem. The theorem states that for a mono-static imaging configuration, the step size must be no greater than $\lambda/4$, where $\lambda$ is the wavelength measured at the operating frequency. Similarly, for the bi-static imaging configuration, the step size must be no greater than $\lambda/2$ [10].

The complex electric field data measured at the antenna is focused into an image of the SUT through a SAR image reconstruction algorithm. Unlike lens-focused imaging where electric fields are physically focused, a SAR reconstruction algorithm mathematically focuses the measurement data by correcting for the physical propagation of the propagating electric field between the antenna and SUT. For SAR, image resolution is determined by several factors, namely: operating frequency, distance between measurement grid and SUT, and step size of the measurement grid [10].

Using a bandwidth of frequencies with SAR imaging allows for increased signal-to-noise ratio (SNR) in 2D images and the ability to generate 3D volumetric images [10]-[11]. When using a bandwidth of frequencies, a collection of 2D images are made of the

SUT at each frequency point in the operating frequency range. These images are coherently integrated, and the indications of the SUT constructively add. Consequently, surrounding noise in the images is random and therefore destructively interfere, which raises the overall SNR of the image. This procedure can be repeated for multiple depths to create 3D images, where depth refers to the distance between the measurement grid and SUT. For 3D imaging, operating frequency bandwidth is inversely proportional to depth resolution, and frequency step size is inversely proportional to maximum unambiguous depth [10].

While SAR imaging traditionally involves mechanically raster scanning a single antenna, recent advances in microwave imaging technology have trended towards electronic raster scanning with antenna array imaging systems [12]-[13]. In this case, an antenna array is employed instead of a single antenna, where the apertures of the antennas form the measurement grid, and the spacing between antenna elements determines the electric field spatial sampling interval. Measurement data is generated by electronically raster scanning along the array, where antennas transmit electric fields and measure the reflections sequentially. The benefit of electronic raster scanning is the decrease in measurement time by orders of magnitude. A mechanical raster scan takes minutes to hours to complete, and an electronic raster scan takes fractions of a second to complete. Combined with the application of Fast Fourier Transforms in the SAR reconstruction algorithm, 2D and 3D images can be generated at video frame-rate, thus enabling a real-time microwave imaging system commonly referred to as a “microwave camera” [12]-[13].

The ability to detect and diagnose dielectric flaws and generate high-resolution representative images in real-time makes a microwave camera an invaluable tool for

inspection. For example, a microwave camera can be made readily portable to be taken into the field by a technician for real-time inspection of aging infrastructure. Similarly, a camera can be deployed in populated areas (e.g., airports, sporting events, etc) for detection of concealed contraband without opening and searching through personal luggage.

One emerging application for microwave cameras is human skin inspection [14]. Skin injuries, such as burn and skin cancers, are typically diagnosed via visual inspection, which is subjective and often inaccurate [15]. Microwave imaging allows for the diagnosis of skin injuries by detecting the relative size and change in dielectric properties of skin, even under medical dressing or clothing [14]. It is also particularly valuable for the elderly population, where performing a biopsy on skin can be potentially harmful and painful. With microwave imaging, a physician can be much more informed on the state of a potentially dangerous skin lesion before performing a biopsy, thus reducing the number of unnecessary biopsies.

For human skin inspection, the ideal camera is one that operates at millimeter wave frequencies. According to [14], the lower end of the millimeter wave frequency range, namely V-band (50-75 GHz), is suitable for detecting changes in human skin composition. This is due to the fact that millimeter waves in this frequency range are maximally sensitive to the individual layers of human skin, and they do not penetrate past skin. Furthermore, if such a camera is to be developed as an effective tool for human skin inspection, among other high frequency imaging applications, it must be designed compact at a fraction of the size of current microwave cameras [12]-[13]. There are a few key reasons for the compact size requirement, namely: small enough to be hand-held and convenient for use in a clinical environment, and for imaging a small, localized portion of skin at any given time.

Additionally, the measurement grid used for imaging typically scales with frequency, such that increasing operating frequency to V-band decreases the imaging area. With the current state-of-the-art in microwave camera technology, significant research must be conducted if a millimeter wave camera is to be developed for imaging human skin. For this reason, the objective of this dissertation is to build the necessary foundation of research to achieve a millimeter wave camera specifically designed for human skin inspection.

## 1.2. RECENT WORK

To determine the necessary research required to achieve a millimeter wave camera for human skin inspection, it is important to review the technological developments that have led to the current state-of-the-art in real-time microwave and millimeter wave imaging. These technological steps include: modulated elliptical slot antenna for electric field mapping, 30-element elliptical slot-based microwave imaging system, 576-element elliptical slot-based microwave camera at 24 GHz, elliptical slot-based linear imaging system at 30 GHz, wideband imaging system based on varactor-tuned elliptical slot antennas, novel Schottky diode-based reflectometer, real-time and wideband 3D microwave camera, and rapid wideband microwave imaging system based on the 3D microwave camera.

The evolution of 3D real-time microwave imaging first began with the development of a 24 GHz resonant elliptical slot antenna for use in mapping the scattered electric field from a SUT [16]. The concept for microwave imaging was based on a bi-static imaging configuration where a single-frequency electromagnetic source irradiates a SUT, and the scattered electric field is spatially tagged (mapped) on the opposite side of the SUT with

an array of elliptical slot antennas. The scattered electric fields are then collected in a receiver for detection after passing through the elliptical slots.

Spatial tagging was achieved via slot load impedance modulation [17]. The elliptical slot antenna was designed to be resonant at 24 GHz with high quality (Q) factor, which meant the slot was exceptionally low-loss. A circular load was placed close to the bottom edge of the slot. When an electric field passed through the slot, the field was concentrated between the slot and load. A PIN diode was then placed in this region such that when it was forward-biased (i.e., ON), the load was short-circuited to the slot, and the slot was effectively closed with a high impedance at 24 GHz. By modulating the PIN diode state, and consequently the slot impedance, the electric field passing through the slot was amplitude-modulated, where this modulation could be measured by the receiver. The modulation depth, which is a figure of merit related to modulation efficiency, was calculated for the designed antenna and was found to be close to 100 % (i.e., highly efficient).

After experimentally verifying the modulated elliptical slot antenna, it was employed in a prototype real-time imaging system at 24 GHz [18]. This imaging system employed 30 elliptical slot antennas in a planar array of 5 rows and 6 columns using the microwave imaging technique outlined in [16]. For this system, an open-ended rectangular waveguide was used as an electromagnetic source, and a metallic sphere was used as a SUT. The imaging system had a high dynamic range and was capable of imaging the metallic sphere at frame-rates exceeding 30 frames-per-second. This system was a demonstration tool to show how a microwave camera can be constructed using elliptical slot antennas and load impedance modulation principles.

The imaging methodology outlined in [16] was fully realized in the development of the portable real-time microwave camera at 24 GHz [12]. This camera expanded upon the system in [18] by employing a 576-element elliptical slot array (24 rows, 24 columns). This camera was designed to be readily portable by integrating the slot array with the receiver through a series of waveguide combiners. Operating at 24 GHz, the camera was capable of reconstructing images of complex dielectric targets at 22 frames-per-second. This camera had the unique feature that it could operate in bi-static mode (similar to [16]), where the electromagnetic source and slot array are on opposite sides of the SUT, and reflection mode, where the source and array were on the same side of the SUT enabling a quasi mono-static imaging configuration. However, the reflection mode was unable to uniformly illuminate the SUT, since the source and slot array were not collocated like an actual mono-static imaging configuration. Regardless of the limitations of the reflection mode, the camera was a significant accomplishment for real-time microwave imaging.

After achieving real-time microwave imaging with the portable microwave camera at 24 GHz, the next step was the design of an imaging system that operated in a full mono-static imaging configuration. The systems described in [18] and [12] were primarily designed to operate in a bi-static imaging configuration. However, this configuration is disadvantageous when one does not have access to the back side of a SUT. Thus, the next system developed was a 30 GHz linear high-resolution imaging system that operated with a mono-static imaging configuration. The system consisted of a linear array of modulated elliptical slot antennas resonant at 30 GHz. The array was designed such that there were 16 transmitting (TX) and 16 receiving (RX) slot antennas interlaced to create TX/RX antenna pairs. The TX and RX antennas were spaced at $\lambda/2$, which effectively created a mono-static

imaging configuration. All TX antennas were fed equally by a transmitter through Wilkinson power dividers, and all RX antennas equally fed into the receiver through similar Wilkinson power combiners. Two-dimensional raster scanning was accomplished by electronically scanning along the linear array with sequential load impedance modulation and mechanical scanning along the second dimension. There was one primary drawback to this imaging system. The interlaced slot antenna configuration resulted in poor isolation between TX/RX pairs at ~12 dB, which lowered the dynamic range of the imaging system. However, this imaging system demonstrated the ability to rapidly scan in a monostatic imaging configuration while being low-cost and in a size that is portable.

After developing the monostatic imaging configuration for elliptical slot antenna arrays, the next step was to move from single frequency operation to operating with a wide bandwidth of frequencies. Mentioned previously, wideband operation has two key benefits in that the generate images have high SNR, and 3D imaging is possible. The load impedance modulation technique used with the elliptical slot antennas in systems described in [12], [18]-[19] was not suited to wideband operation, since the elliptical slots were highly resonant. The solution was to employ varactor-loaded elliptical slots in the 18-26.5 GHz wideband imaging array described in [20]. This system was composed of a vector network analyzer (VNA), two 4-element slot antenna arrays (one transmit array and one receive array), two RF 1:4 switches, and one RF amplifier. The elliptical slot antenna was similar to the one designed in [16], but the slot was loaded with a varactor diode instead of the PIN diode. With a varactor diode, the slot capacitance, and more importantly resonant frequency, could be electronically tuned with a DC voltage. This allowed the slot to transmit and receive signals in the full K-band (18-26.5 GHz). An additional change to the

slot was that it was fed by a microstrip line instead of the traditional waveguide feed due to the work in [21]. This allowed the slots to be made more compact (i.e., placed closer together) for higher imaging resolution.

Two-dimensional raster scanning was conducted by electronically scanning along the transmit and receive arrays via setting the RF switch state and mechanically scanning along the second dimension. The VNA served as both transmitter and receiver for this system. Separate transmit and receive arrays were employed, so an RF amplifier could be placed between the receive array and the VNA to increase SNR in measurement data. This system could produce high resolution 3D images of multiple targets with varying dielectric properties.

The limitation of the wideband imaging system described in [20] was that it required a VNA to make coherent magnitude/phase measurements for SAR imaging. In order to achieve a portable microwave camera, a new methodology for making coherent measurements for SAR imaging was required. This was accomplished with the novel reflectometer presented in [22]. A reflectometer is a device that has been traditionally used in 2D mechanical raster scanning for microwave imaging and is composed of a transmitter, antenna, and receiver. While many reflectometers employ a quadrature mixer as the receiver for producing phase coherent I/Q data for imaging, this new reflectometer employed an open-ended rectangular waveguide (as the antenna) with a Schottky diode placed close to the waveguide aperture to serve as the receiver. The diode sampled the transmitted and received signals and mixed both. The output was a DC voltage proportional to the standing wave at the diode's sampling point. Consequently, this voltage was also proportional to the real part of the reflection coefficient between the transmitted and

received signals. Since the Schottky diode was positioned at the waveguide aperture, the output voltage was phase calibrated to the measurement grid automatically, and therefore this voltage was sufficient to generate SAR images. Using a Schottky diode as the receiver significantly reduced imaging hardware, since all of the receiver components (e.g., couplers, isolators, mixers, etc.) were removed and replaced with a single Schottky diode. Additionally, Schottky diodes are sensitive to a wide bandwidth of frequencies allowing it to be used for wideband microwave imaging.

There were a few limitations to using a Schottky diode as a receiver. The first is that since the real-part of the reflection coefficient was sampled, an identical image of the SUT was formed below the actual image at the output of the SAR algorithm. This was not a significant issue, since the image bounds are always known, and the identical image can be cropped out. A second limitation is that the output of a Schottky diode has a lower SNR when compared to traditional I/Q detection.

This novel reflectometer was used as the basis for the first wideband, real-time microwave camera [13]. This camera was composed of a 256-element array of tapered slot-line antennas, where each antenna was loaded with two Schottky diodes. This meant the camera contained 512 receivers. The 2D antenna array was composed of 16 linear antenna arrays, where each array contained 16 slot-line antennas arranged at the edge of a PCB. The antenna array was fed by a 20-30 GHz wideband source that was multiplexed to a single antenna at a time through a network of monolithic microwave integrated circuit (MMIC) switches and amplifiers. The Schottky diode output voltages were routed with low-frequency multiplexers and fed into two 16-bit analog-to-digital converters (ADCs). One measurement frame consisted of 512 diode voltage measurements at 101 frequency

points, which is a total of 51,712 measurements or 50.5 kB of memory. The camera was controlled by two real-time system (RTS) microcontrollers and a microprocessor and could obtain measurement frames at 30 frames-per-second (1.515 MB/s). This camera was capable of producing high-resolution 2D images of complex dielectric structures. With the addition of an external graphics processing unit (GPU) it was capable of rendering full 3D volumetric images of dielectric structures at 30 frames-per-second. Finally, this system was contained completely within a 10” x 9” x 7” enclosure, which made it readily portable for real-time 3D imaging for in-field applications. Many imaging results were generated with this system demonstrating its suitability for critical NDT and security applications.

A rapid wideband imaging system was developed based on two of the linear arrays from the wideband camera [23]. These arrays were stacked and staggered by half of the width of a slot-line antenna. Raster scanning was performed by electronically scanning along both arrays and then mechanically scanning along the second dimension. In this configuration, the number of spatial measurement points was approximately four times that of the wideband camera. While this system could not produce images in real-time, it could scan over a 6” x 5” area in less than one minute. Imaging results showed that this system was capable of rapidly producing high-resolution 3D images for NDT and security applications.

### 1.3. ORGANIZATION OF THE DISSERTATION

Mentioned previously, the objective of this dissertation has been to build the necessary foundation of research to achieve a millimeter wave camera specifically designed for human skin inspection. Multiple research investigations have been conducted to determine how current imaging systems and methodologies must evolve to develop a

compact millimeter wave camera for imaging human skin. These investigations and findings are outlined in the following papers.

Paper I explores the effect of frequency uncertainty in signals produced by a microwave camera on SAR-generated images. Microwave sources, such as the HMC733 free-running voltage-controlled oscillator (VCO) in the wideband microwave camera reported in [13], have some level of frequency uncertainty (i.e., difference in expected output frequency compared to the actual signal frequency generated by the source) [24]. The goal of this investigation was to quantify the degradation in SAR-generated images as a function of frequency uncertainty. Frequency uncertainty was assumed to be stochastic and non-systemic and was therefore modeled using a statistical distribution. It was found through simulation and experimental verification that the level of image distortions in SAR-generated images is directly proportional to the product of frequency uncertainty and distance between imaging measurement grid and SUT. Finally, the frequency uncertainty statistical distribution of the HMC733 VCO used in the wideband microwave camera was determined experimentally [24]. The results of these experiments showed that for NDT applications, the level of frequency uncertainty in an HMC733 VCO does not visually degrade image quality.

In Paper II, a SAR-based millimeter wave imaging system was developed as the basic building block for a millimeter wave camera. Operating at 58-64 GHz, the system was designed specifically for human skin inspection, in addition to traditional NDT applications. The system was composed of a transceiver and two antipodal Vivaldi-style antennas (AVAs). The transceiver was designed based on commercially-available system-on-chip (SoC) transmitters and receivers. However, the bulk of the investigation was in the

design of the antenna. The antenna was designed on a PCB and consisted of a substrate integrated waveguide (SIW), corrugated Vivaldi-style radiators, and a dielectric lens. Simulation and measurements showed the antenna was suited for millimeter wave imaging with 6 GHz of -10 dB reflection coefficient bandwidth and ~76° half-power beamwidth. A robust phase-calibration procedure was developed for the millimeter wave imaging system based on single frequency SAR imaging. The result of the investigation was a hardware platform by which to develop a millimeter wave camera for SAR imaging.

Finally, in Paper III, a completely new SAR-based microwave imaging methodology was developed to achieve microwave and millimeter wave cameras at a fraction of the size and hardware complexity compared to previous systems. The new imaging methodology named Chaotic Excitation Synthetic Aperture Radar (CESAR) operated based on all antennas in the camera transmitting and receiving, instead of electronic raster scanning. With this approach, a significant portion of the RF hardware could be removed. However, the reduction in hardware came at the cost of reduced image quality. A prototype camera operating at 23-25 GHz was developed to demonstrate CESAR imaging. This camera, which was a fraction of the size of the wideband camera in [13], was designed with Schottky diode-based interferometry and employed a 64-element array of rectangular slot antennas [22]. The camera consisted of a transmitter, antenna array loaded with Schottky diodes, and a data acquisition system. Simulations and experimental results showed that this camera was capable of generating SAR images, where the basic location and shape information of a dielectric flaw in a complex dielectric structure could

be determined. The result of this investigation was a new SAR imaging methodology that allows for designing microwave and millimeter wave cameras that are highly compact and portable for many critical applications.

# PAPER

## I. EFFECT OF INSTRUMENT FREQUENCY UNCERTAINTY ON WIDEBAND MICROWAVE SYNTHETIC APERTURE RADAR (SAR) IMAGES


## ABSTRACT

In this paper, we investigate the effect of frequency uncertainty in signals generated or measured by a microwave instrument on the resulting synthetic aperture radar (SAR) images, particularly for nondestructive testing (NDT) applications. Wideband SAR imaging systems measure reflections from a target by irradiating it with locally-generated signals that can potentially have some level of frequency uncertainty. Quantifying this frequency uncertainty provides the user with a realistic and expected level of image distortion which may manifest itself as blurring, noise artifacts, etc. In this study, we show that as uncertainty in the actual frequency value increases, the level of image distortions increases predominantly for distant targets. This is an important fact for NDT applications since the imaged object is commonly close to the imaging system. In addition these imaging system usually have a limited "aperture" size, which makes target distance an important consideration. For complex targets, we show how frequency uncertainty-based image distortions can dominate features in an image depending on the reflected signal amplitude from the target. We also show that in real imaging systems, the statistical distribution of frequency uncertainty combined with practical, near target ranges (distances) produce non-discernible image distortions.


**Index Terms:** Instrumentation error, nondestructive testing, frequency uncertainty, image distortion, SAR imaging.

# 1. INTRODUCTION

In recent years, portable, high-resolution and real-time wideband microwave imaging systems have been developed capable of producing 3-D synthetic aperture radar (SAR) images of objects for nondestructive testing (NDT) applications [1]-[3]. For these applications in particular, the target (object to-be-imaged) is usually placed close to the imaging system, where a wideband microwave signal irradiates it, and the resulting reflected signal is collected over a predetermined 1D or 2D spatial grid (i.e., the imaging array). Subsequently, efficient SAR imaging algorithms are used to generate a high-resolution 3D image of the target. A prime benefit of SAR imaging is its utilization of coherence in the reflected electromagnetic signal across a large number of spatial measurements and frequency points (within the operating bandwidth). Utilizing coherence significantly improves image signal-to-noise ratio (SNR) even in the presence of relatively high noise levels. However, with all practical imaging systems, there exists some level of instrumentation error (e.g., frequency uncertainty) that can potentially result in image distortions which may be manifested in several different ways including blurring, noise artifacts, etc. [4]. While the term image distortion refers to the presence of unwanted features in an image, the root-mean-square (RMS) error between images with and without distortions, defined by $l^2$-norm of the normalized image error compared to an ideal image, represents a quantitative measure of the level of distortions [4].

Previous studies have addressed the effect of uniform, non-uniform, and random sampling on generated SAR images [4]-[6]. For aperture-limited microwave imaging systems, image spatial resolution degrades as a function of increasing target distance. This degradation either creates or adds to the error associated with the generated image.

With respect to frequency, efforts have been made to study and correct for the effect of systemic sources of frequency deviations in linear frequency-modulated continuous-wave (L-FMCW) radars [7], [8]. Nonlinearities in the frequency-time relationship of the frequency modulation are corrected using a range of pre- and post-processing tools. Corrections can be made since the frequency deviation is systemic and repeats for all frequency sweeps in the measurement data.

To date, the effect of zero-mean frequency uncertainty in wideband SAR images, caused primarily by the imaging instrumentation, has not been studied. Frequency uncertainty is defined as the difference between the frequency the operator uses to create an image (assuming that is the frequency at which the image data is collected) and the actual frequency at which the reflected signal is measured by the system. The term uncertainty is used because, for this study, the difference between assumed and actual frequency is stochastic and non-systemic. Sources of this type of frequency uncertainty are generated by random noise in the system (e.g., thermal). Examples of frequency uncertainty in instrumentation include phase error in phase-locked loops and main source oscillator phase noise. Additionally, recent microwave imaging trends towards developing real-time imaging systems, have employed free-running voltage-controlled oscillators (VCOs) that are susceptible to frequency uncertainty [3]. Since frequency uncertainty is stochastic and uncorrectable, it is extremely important to study the effects of frequency uncertainty in order to understand its influence on SAR-generated images as well as to determine ways by which to reduce its impact.

This study aims to quantify the effect of instrumentation-caused frequency uncertainty in SAR-generated images of targets primarily for NDT applications and is an

extension of the preliminary work presented in [9]. Many previous studies have attempted to quantify measurement error in airborne and space-borne SAR systems, due to: antenna phase center estimation error, observation point error, antenna directing jitter, and pulse repetition frequency jitter [10]-[13]. However, for NDT applications, where the target of interest is relatively close to the imaging instrument and the operating frequency bandwidth is significantly larger, phase and/or frequency deviations can also cause significant image distortion. This study quantifies image distortions in SAR-generated images for a selection of simple and complex targets and determines a combination of frequency uncertainty and target range that generates visible distortions in the SAR-generated images. Finally, the statistical distribution of frequency uncertainty of a VCO that is used in a real-time microwave camera is determined to show what levels of image distortions are to be realistically expected in an NDT imaging application.

## 2. BACKGROUND

The SAR algorithm implemented in this study is based on the ω-*k* algorithm, described in [4]. The algorithm is particularly suitable for NDT applications, since it generates 3-D images from stepped-frequency reflection coefficient measurements recorded by a wideband imaging system. The ω-*k* algorithm is summarized in Figure 1.

The portion of the algorithm that is of interest in this study is in the Range 1-D Non-Uniform Fast Fourier Transform (NUFFT) operation shown below:

$$D_L(k_x, k_y, k_z) \rightarrow S(k_x, k_y, z). \quad (1)$$

The cross-range measurement data $D_L$ is a function of wavenumber $k_z$, which is related to the actual measured frequency values implemented in the algorithm. The transform converts the spectrum data into the image spectrum ($S$), as a function of range,

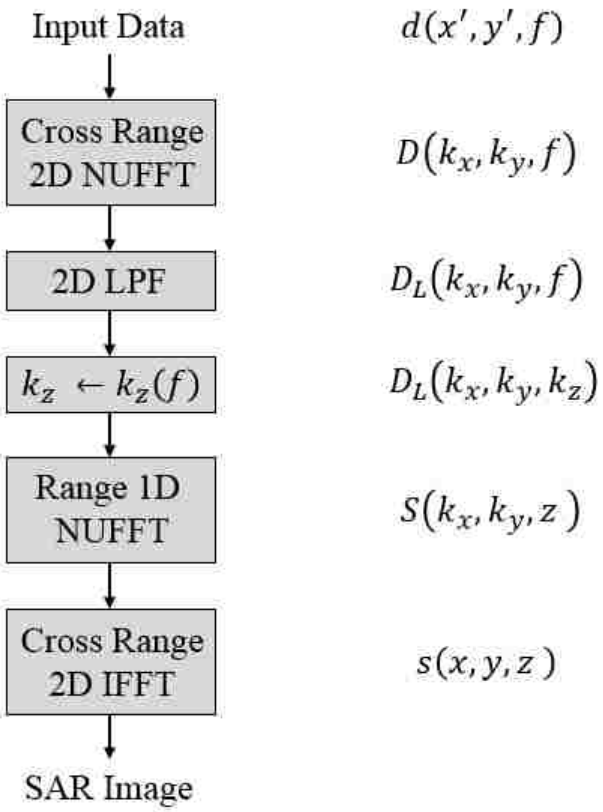


Figure 1. SAR ω-*k* algorithm [4].

$z$. From a practical perspective, the magnitude and phase of the measured data is back-propagated (i.e., focused) to specific ranges (i.e., distances) with multiple specified frequencies.

Thus, the result of the operation is a dataset with complex magnitude and phase for specific ranges. It is this operation that creates image distortions when the data measured at incorrect frequencies is back-propagated in the algorithm.

The following derivation shows how image distortions can be generated with a given frequency uncertainty at a fixed target range. Let $f_0$ be one of the frequencies in the range 1D NUFFT, and let $f_m$ be one of the measurement frequencies, such that:

$$f_m = f_0 + \Delta f \tag{2}$$

where $\Delta f$ is an unknown (random) difference in frequency (i.e., the difference between the frequency used to make the image and the actually-measured frequency), representative of frequency uncertainty. The ω-*k* SAR algorithm assumes round-trip free-space Green's function for the wave propagation model:

$$d(x', y', f_0) = \left(\frac{1}{R^2}\right) e^{-j2kR} \tag{3}$$

where, $f_0$ is the frequency SAR implements in the calculation and $R$ represents the target range. The SAR algorithm back-propagates the measurements to the target location using this model to create the image. The back-propagation uses the phase term $2\pi fR/c$ to "focus" the measurement data. Considering the frequency uncertainty, $\Delta f$, this leads to an uncertainty in the phase term, $\Delta\phi$, as shown below:

$$\Delta\phi = 2\pi f_m R/c - 2\pi f_o R/c \tag{4}$$

$$\Delta\phi = 2\pi\Delta f R/c \tag{5}$$

From equation (5), it is clear that as $\Delta f$ and $R$ increase, $\Delta\phi$ increases. Since SAR requires coherent phase pattern measurements, the existence of $\Delta\phi$ creates image distortions. The SAR algorithm averages the data in each image pixel and hence improves the signal-to-noise ratio (S/N), associated with the image, by a factor of $\sqrt{N}$, where $N$ is defined by:

$$N = N_x N_y N_f. \tag{6}$$

In this equation, the $N_x$ and $N_y$ variables represent the number of spatial data points in *x* and *y* directions (if a two-dimensional scan is performed, and only *x* if the scan is one-dimensional), and $N_f$ represents the number of sampled (measured) frequencies. Since SAR averages the measurement data, it is also important to consider the percentage of data with high $\Delta\phi$. Commonly, image distortions associated with RMS image error greater than

-20 dB are considered to be a reasonable limit with respect to image quality [4]. This averaging feature shows that for frequency uncertainty-based image distortions to significantly degrade image quality, a certain percentage of the measurement data must have $\Delta\phi$ greater than some threshold that is to be determined. It can then be said that if the data has a $\Delta\phi$ less than the threshold, it will produce non-discernable or acceptable image distortions, similar to an unfocused SAR image [14]. As the percentage of data with $\Delta\phi$ greater than the threshold increases, the visible image distortions should increase. In the following section we show how image distortions are quantified based on $\Delta f$ and $R$ and the way by which the $\Delta\phi$ threshold, as a combination of these parameters, is determined.

## 3. SIMULATION RESULTS

The relationship between image distortions, frequency uncertainty, and target range was quantified with a number of simulated scans of a point target. The simulations were conducted in MATLAB®, where simulated measurements were made of a point target on a line vector at specified locations ($x$, $z = 0$). At each location, an isotropic antenna radiates a microwave signal in the Ka-Band frequency range of 26.5 – 40 GHz. Subsequently, the complex reflection coefficients from the target are calculated at 201 frequency points. Figure 2 shows the schematic of the point target and measurement locations, located at $(x_t, z_t)$ and $(x, 0)$, respectively. The complex reflection coefficients were calculated at 101 locations, with $\frac{\lambda}{4}$ spacing, creating a 25λ-long array, where λ represents the wavelength at 40 GHz. This frequency was chosen to satisfy the Nyquist sampling criteria for wideband uniform microwave imaging. The equation used to calculate the reflected signals from the point target is:

$$D(x,f) = \left(\frac{1}{R^2}\right) e^{-j2kR}. \quad (7)$$

In equation (7), $D$ represents the simulated reflection coefficients, $k$ is the wavenumber related to the measurement frequency, and $R$ is the Euclidean distance between the point target and measurement location:

$$R = \sqrt{(x - x_t)^2 + z_t^2}. \quad (8)$$

Frequency uncertainty was introduced by creating random offsets in the frequency vector for each frequency point and measurement location. The offsets were limited to a specified frequency uncertainty bandwidth (BW) and were modeled by the uniform statistical distribution:

$$\Delta f \sim Uniform\left(-\frac{BW}{2}, \frac{BW}{2}\right). \quad (9)$$

The uniform statistical distribution was chosen since it represents an equal likelihood of a frequency offset across the specified bandwidth, which produces the highest measurement error for a given line scan. The generated $\Delta f$ has the same probability of being high (close

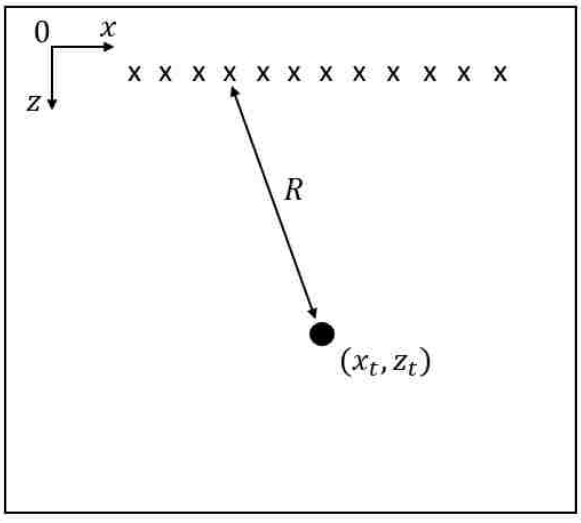


Figure 2. Schematic of measurements from a simulated point target.

to $-\frac{BW}{2}$ or $\frac{BW}{2}$) and low (close to 0). Generating the highest measurement error was desired, since the first goal of this study was to identify the minimum level of frequency uncertainty that is required to produce image distortions that degrade image quality. Other distributions weight high $\Delta f$ with low probability, and thus would generate statistically lower image error. Real instrumentation, such as a VCO, may not have a uniform distribution (i.e., better performance than when the distribution is uniform). In Section 5, a statistical distribution representative of real instrumentation is determined through experimentation.

For the simulations, the frequency uncertainty bandwidth ranged from 0.1 to 1000 MHz, which the latter represents severe frequency uncertainty at the simulated Ka-band frequency range (i.e., relatively large percentage of the operating bandwidth). Most VCOs have much lower frequency uncertainty, as will be shown in Section 5. Additionally, the point target range ($z_t$) spanned 0.1 to 200λ. For each frequency uncertainty bandwidth and target range, two images were produced. The first was an image generated with measurements containing frequency uncertainty ($S_{(x,z)}$), and the second was generated with measurements contained no uncertainty representing the reference image, ($I_{(x,z)}$). Subsequently, $l^2$-norm was calculated similar to [4], as:

$$l^2 - norm = \sqrt{\frac{\sum_{x\in x}\sum_{z\in z}\left(|I_{(x,z)}|-|S_{(x,z)}|\right)^2}{\sum_{x\in x}\sum_{z\in z}\left(|I_{(x,z)}|\right)^2}}. \tag{10}$$

The $l^2$-norm was recorded in dB-scale for each frequency uncertainty bandwidth and target range, and the values were combined into a contour map, as shown in Figure 3. From the contour map, it can be seen that $l^2$-norm increases as a function of increasing frequency uncertainty bandwidth and target range. One of the contours on the plot is defined at -20 dB (as stated earlier), which was used to determine the combination of

frequency uncertainty bandwidth and target range that produces a $\Delta\phi$ threshold that creates image distortions above the -20 dB limit. This threshold was found to be 0.073π radians and was found by reading off $\Delta f$ and $R$ values from Figure 3 and putting them into equation (5). With this threshold, for every combination of frequency uncertainty bandwidth and target range that formed the contour plot in Figure 3, the percentage of measurement data points in the line scan simulation that contained a $\Delta\phi$ exceeding the 0.073π-radian threshold was calculated. Since the frequency uncertainty was generated by the uniform statistical distribution, this percentage can be defined by the cumulative probability:

$$P_{Image} = P_{Uni}(|\Delta\phi| > 0.073\pi)\ x\ 100\% \tag{11}$$

In this equation, $P_{Uni}(|\Delta\phi| > 0.073\pi)$ is the probability that a given measurement point has a $\Delta\phi$ greater than ±0.073π. A plot of frequency uncertainty bandwidth as a function of target range with these percentages is shown in Figure 4. This plot shows that for most values of frequency uncertainty bandwidth and target range, the percentage of

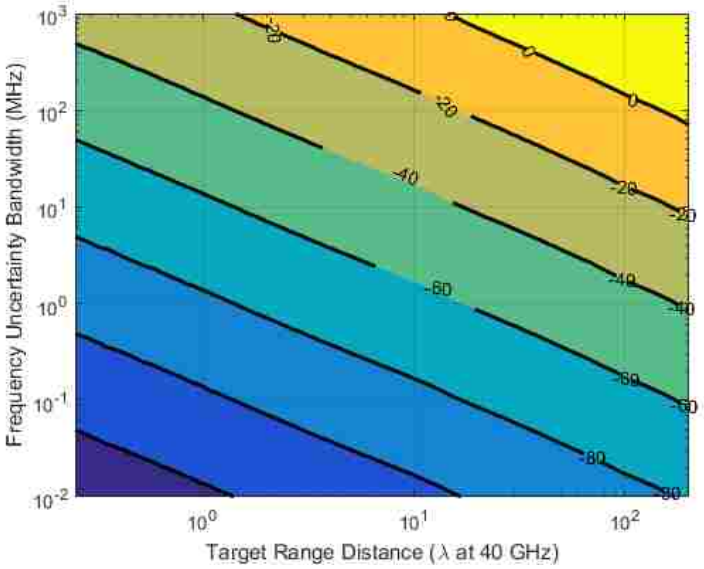


Figure 3. Contour plot of $l^2$-norm as a function of frequency uncertainty bandwidth and target range.

measurement data with $|\Delta\phi| < 0.073\pi$ is less than 20%. This must be true since for most combinations of frequency uncertainty bandwidth and target range in this region, $\Delta\phi$ never increases above the threshold due to the limits set on frequency uncertainty in equation (9). However, in the region where $\Delta\phi$ increases above the threshold, the percentage of measurement data above the threshold increases significantly to above 80% with increasing frequency uncertainty bandwidth and target range.

Comparing Figure 3 and Figure 4 shows that images with $l^2$-norm greater than 0 dB will have measurement data that is at least 80% above the threshold. In practice, these plots show that $l^2$-norm can be minimized by minimizing frequency uncertainty in the instrumentation and imaging targets close to the measurement system. To illustrate the effect of frequency uncertainty on SAR images, Figure 5 shows several images that were produced for several (point) target ranges and frequency uncertainty bandwidths. Images are shown for the same array length of 25λ at target ranges of 10λ, 25λ, and 50λ to

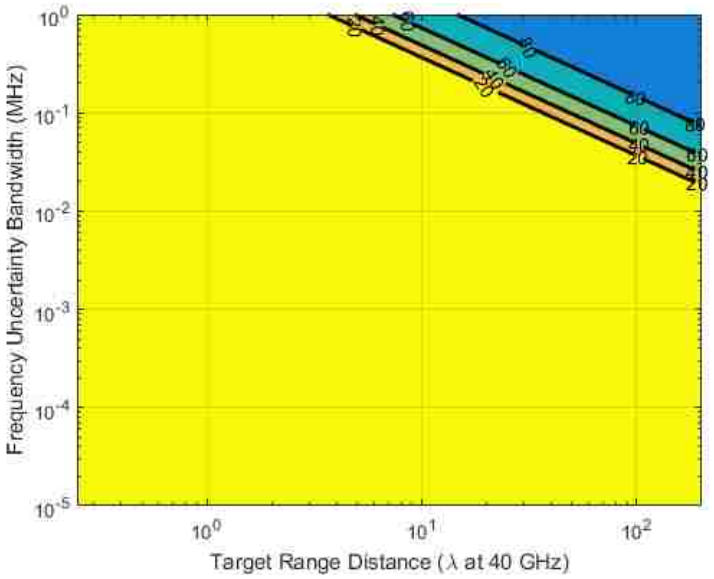


Figure 4. Contour plot of $P_{Image}$ as a function of frequency uncertainty bandwidth and target range.

demonstrate the effect of image degradation as a function of target distance (for this aperture-limited SAR case) [4]. Additionally, the images were produced for a series of frequency uncertainty bandwidths, ranging from 0 to 1000 MHz.

Tables 1 and 2 show the calculated $l^2$-norm and highest possible $\Delta\phi$ relating to the images in Figure 5. The images produced at 50λ show the effect of resolution degradation, since the target appears bulbous with some unwanted image artifacts surrounding the target. However, image distortion as a function of frequency uncertainty is significant for the 1000 MHz case (Figure 5m – Figure 5o) and is substantial primarily for the 50λ distance case (Figure 5o). Table 1 confirms this fact with the last row having values substantially greater than -20 dB. For the 100 MHz, 25λ and 50λ cases in Figure 5k and Figure 5l, the image distortions are less significant, since the $l^2$-norm values are -15.66 dB and -9.08 dB (close to the -20 dB threshold). Table 2 also confirms these findings with maximum $\Delta\phi$ values greater than the $0.073\pi$ threshold. Practically, this means that for NDT applications, where the target is imaged close to the array, high levels of frequency uncertainty (1000 MHz and higher) may be tolerated before image distortions become visible.

## 4. MEASUREMENT APPROACH AND RESULTS

Experimental line scan measurements were performed to verify the effect of frequency uncertainty and its dependence on target range in SAR image processing. For these experiments, the point target was represented by a thin copper wire stretched in the direction orthogonal to the image plane shown in Figure 6, which makes the image of the wire the cross-sectional area resembling a point target. A copper wire produces higher reflections than a small metal ball, where higher reflections are needed to reduce the effect of measurement noise on and improve $l^2$-norm calculation based solely on frequency

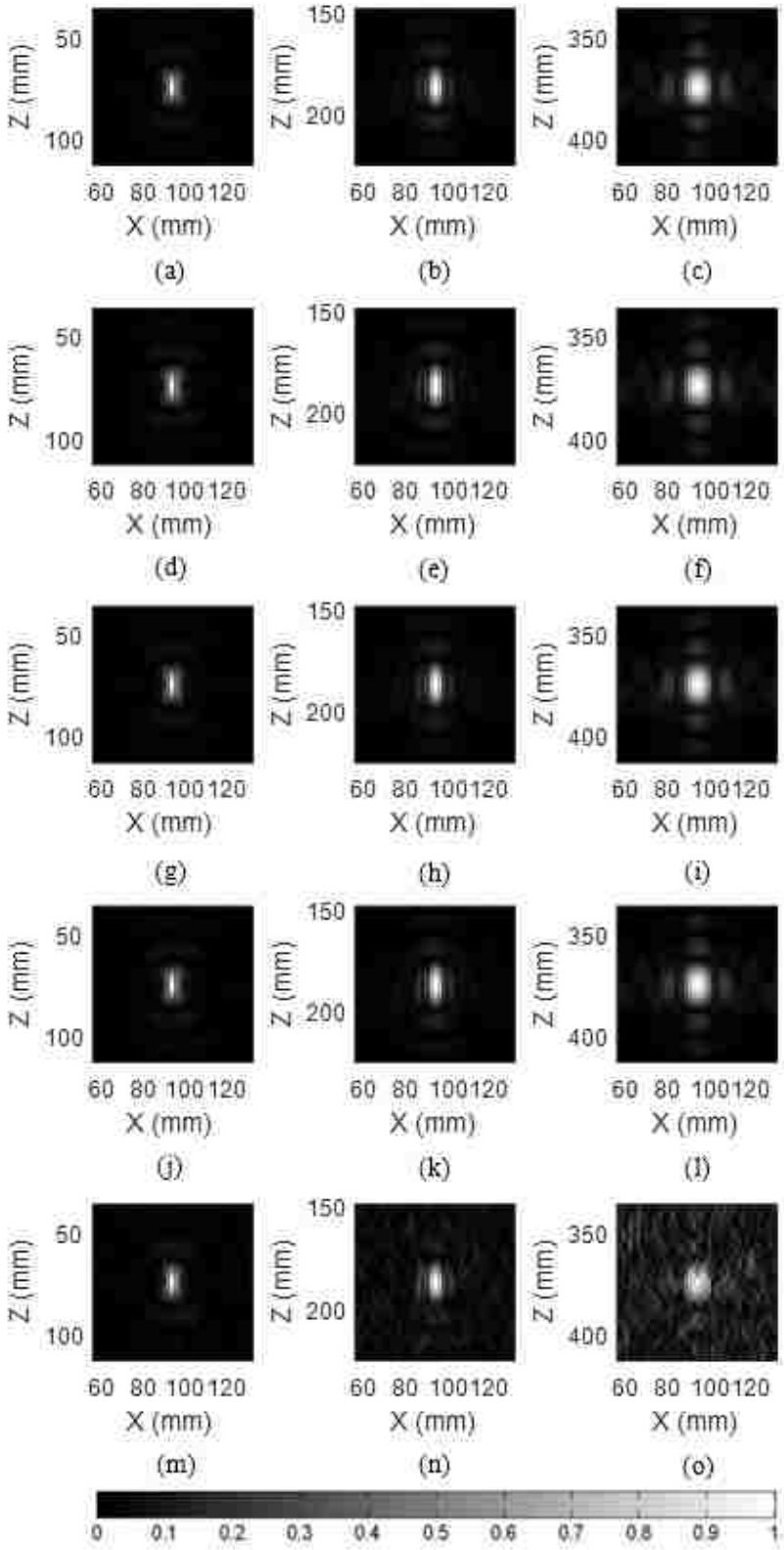


Figure 5. Images produced from a point target with various levels of frequency uncertainty bandwidth and at different target ranges. Columns represent 10λ, 25λ, and 50λ. Rows represent 0 MHz, 1 MHz, 10 MHz, 100 MHz, and 1000 MHz.

Table 1. $l^2$-norm (dB) for Various Frequency Uncertainty Bandwidths and Target Ranges.

| **Frequency Uncertainty Bandwidth (MHz)** | **Target Range** | | |
|---|---|---|---|
| | ***10λ*** | ***25λ*** | ***50λ*** |
| ***0*** | -∞ | -∞ | -∞ |
| ***1*** | -64.46 | -56.56 | -50.82 |
| ***10*** | -44.56 | -36.70 | -30.97 |
| ***100*** | -24.51 | -15.66 | -9.08 |
| ***1000*** | -3.02 | 0.92 | 1.38 |

Table 2. Maximum $\Delta\phi$ (rad.) For Various Frequency Uncertainty Bandwidths and Target Ranges.

| **Frequency Uncertainty Bandwidth (MHz)** | **Target Range** | | |
|---|---|---|---|
| | ***10λ*** | ***25λ*** | ***50λ*** |
| ***0*** | 0 | 0 | 0 |
| ***1*** | $2.5\pi \; x \; 10^{-4}$ | $6.4\pi \; x \; 10^{-4}$ | $1.3\pi \; x \; 10^{-3}$ |
| ***10*** | $2.5\pi \; x \; 10^{-3}$ | $6.4\pi \; x \; 10^{-3}$ | $1.3\pi \; x \; 10^{-2}$ |
| ***100*** | $2.5\pi \; x \; 10^{-2}$ | $6.4\pi \; x \; 10^{-2}$ | $0.13\pi$ |
| ***1000*** | $0.25\pi$ | $0.64\pi$ | $1.3\pi$ |

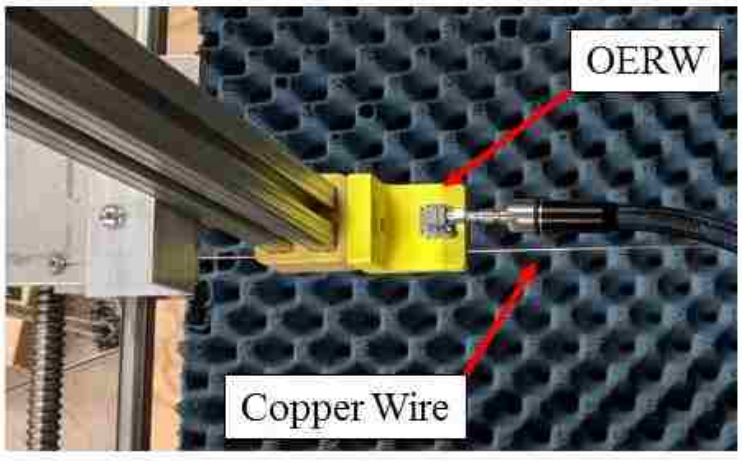


Figure 6. Measurement setup of an OERW scanning over a straight copper wire.

uncertainty. The isotropic antenna (in the simulations) was represented by a Ka-band (26.5-40 GHz) open-ended rectangular waveguide (OERW) antenna, which has a wide beamwidth. The OERW was fed by an Anritsu Vector Star MS4644A Vector Network Analyzer (VNA), where it generated signals in the Ka-band frequency range. The OERW was attached to an automated positioning system for performing the line scans.

Scans were made for the same target ranges of 10λ, 25λ, and 50λ and for the same number of measurement points in frequency and *x* to directly compare to the simulation results. Prior to processing the image data to produce SAR images, frequency uncertainty was added by interpolating the recorded data to a new frequency vector with added frequency uncertainty bandwidth generated by the same uniform statistical distribution, as in simulations. The input to the interpolation was the experimental data, which was measured as a function of the theoretical frequency range that would be implemented in SAR. The output of the interpolation was the same data, but slightly corrupted to match measurements made on a similar frequency range but with a specified frequency uncertainty bandwidth, similar to the previous MATLAB simulations. Figure 7 shows the calculated $l^2$-norm as a function of the three distances between the OERW and the target and different frequency uncertainty bandwidths. For the 50λ distance, a simulation for the same distance is plotted for comparison. Figure 8 shows images in an arrangement similar to Figure 5 for these scans. From Figure 7, $l^2$-norm, plotted in dB scale, increases as a function of frequency uncertainty bandwidth and target range, as expected. However, the magnitude of $l^2$-norm in the 300-1000 MHz range differs from simulation. This is attributed to the interpolation scheme that was used to add frequency uncertainty to

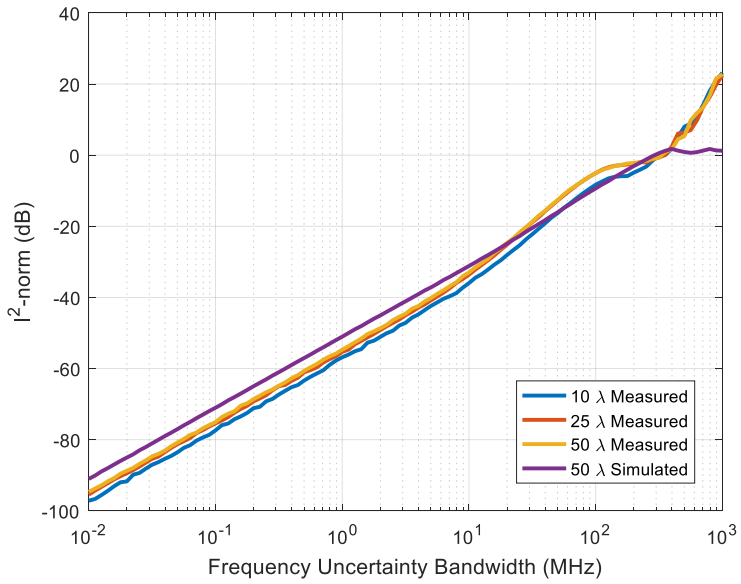


Figure 7. Results of $l^2$-norm for three experimental line scans at different target ranges and varied frequency uncertainty bandwidth and one simulated line scan for comparison.

experimental measurements, which is absent in simulation (this effect is also evident in Figure 8m,n,o).

While a copper wire was scanned at different target ranges for comparison to simulation, a complex target composed of copper tape strips forming a plus sign, three vertical bars, and three horizontal bars was scanned using the same scanning apparatus to show how frequency uncertainty-based image distortions can dominate different features in an image. This complex target was scanned at a target range of 10λ, and different levels of frequency uncertainty bandwidth (0, 250, 500, 750, 1000 MHz) were chosen to show a more gradual transition from no distortion to a completely distorted image. These results are shown in Figure 9, where Figure 9a shows the complex target that was imaged. In Figure 9b, the target is shown with no frequency uncertainty. The blurring in the three vertical bars and the vertical component of the plus sign is a result of the OERW having a

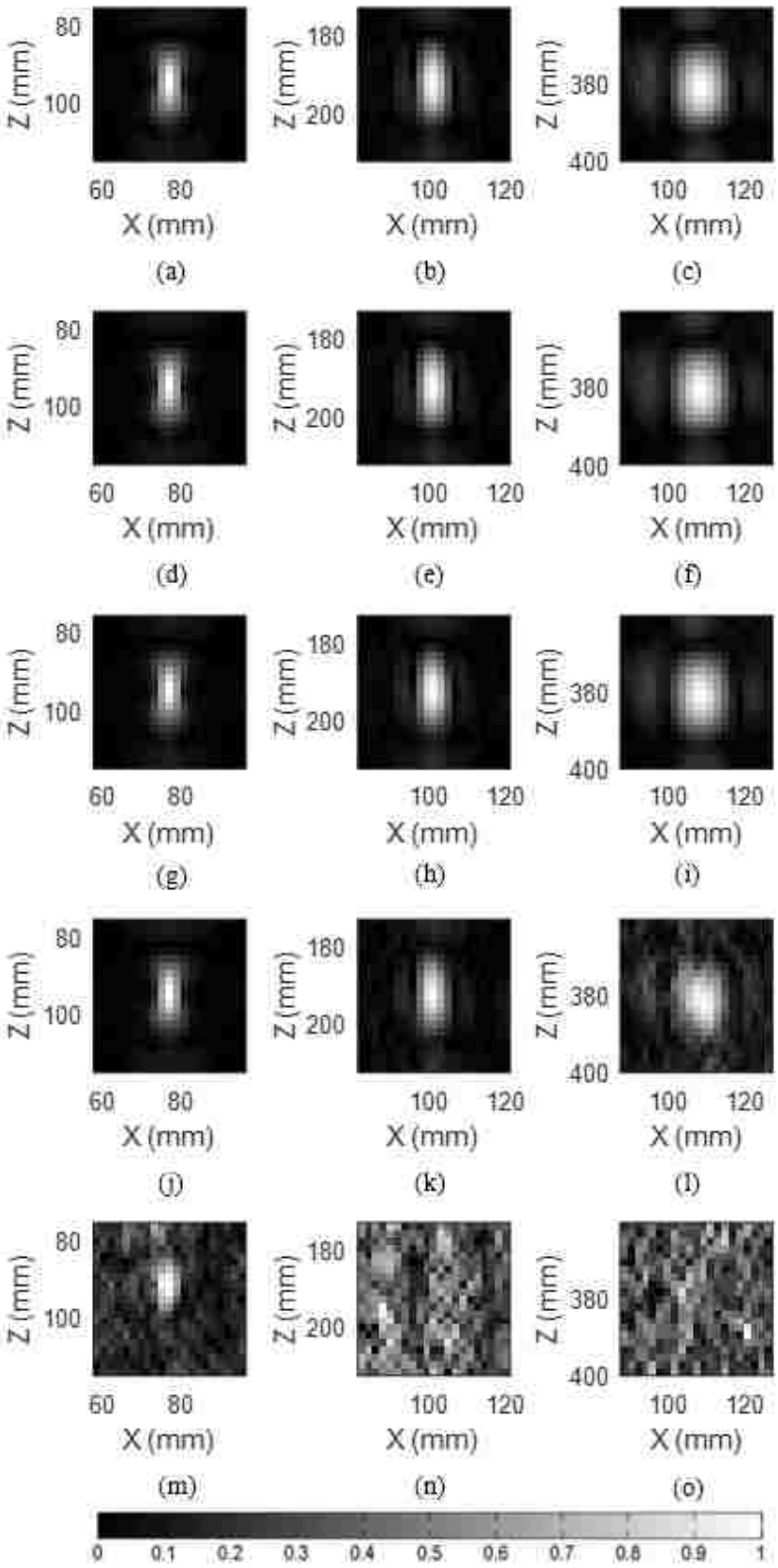


Figure 8. Image results of a copper wire with various levels of frequency uncertainty bandwidth and target range. Columns represent 10λ, 25λ, and 50λ. Rows represent 0 MHz, 1 MHz, 10 MHz, 100 MHz, and 1000 MHz.

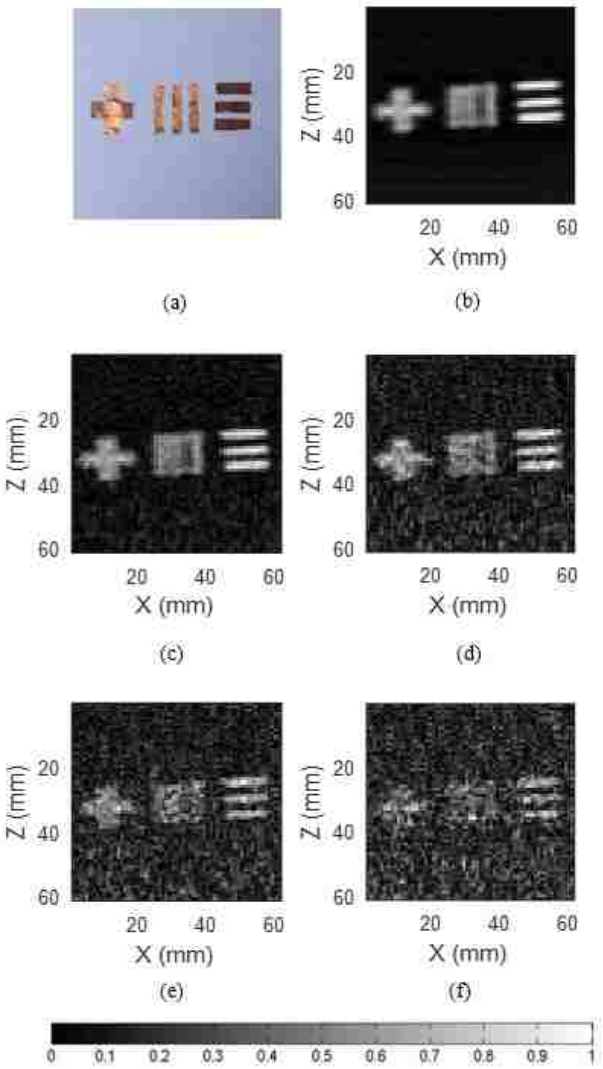


Figure 9. Image results of a complex with various levels of frequency uncertainty bandwidth at a target range of 10λ. (a) Picture of complex target, (b-f) SAR images with frequency uncertainty bandwidths of 0 MHz, 250 MHz, 500 MHz, 750 MHz, and 1000 MHz, respectively.

relatively narrower beamwidth in the vertical direction with respect to the wide beamwidth in the horizontal direction [4]. As the frequency uncertainty bandwidth increases, the three vertical bars become the first target to be completely masked by image distortions, since they have a lower signal amplitude (darker). The plus sign was dominated to a lesser degree by image distortions, and the three horizontal bars remain visible against the distortions for

all cases, since they had a higher signal amplitude (brighter). Therefore, in the presence of a fixed frequency uncertainty level for which there is a weakly scattering target (i.e., the vertical bars) and a strongly scattering target (i.e., the horizontal bars), the former will be masked ahead of the latter as frequency uncertainty increases.

## 5. FREQUENCY STATISTICAL DISTRIBUTION OF HMC733LC4B VOLTAGE CONTROLLED OSCILLATOR

Simulation and experimental results from previous sections in this study show the level of frequency uncertainty bandwidth required to produce distortions that degrade image quality in SAR-generated images. The aim of this section is to determine the statistical distribution frequency uncertainty takes for an actual instrument.

The device under test was the HMC733LC4B VCO, which was used as the frequency generator in the real-time, wideband microwave camera described in [3]. The statistical distribution for its output frequency was determined by tuning the VCO to a theoretical output frequency specified according to its data sheet and recording the actual generated frequency [15]. In this microwave camera [3], the VCO sweeps frequency from 10 GHz to 15 GHz over a short period of time on the order of hundreds of microseconds. The VCO was swept in this manner to ensure that whatever frequency uncertainty occurred under these conditions would match the conditions in the microwave camera. To do so, the VCO output frequency was measured in the time domain with an HMC144LC4 down-mixer and Keysight DSOX2024A oscilloscope. A diagram of the test setup is shown in Figure 10. Capturing the VCO output frequency in the time domain allowed for recording frequency uncertainty over a short period of time (cycle-to-cycle) as well as over a long period of time (frequency sweep-to-sweep). An Anritsu Vector Star MS4644A VNA provided the local oscillator signal for down-mixing to the IF range for the oscilloscope

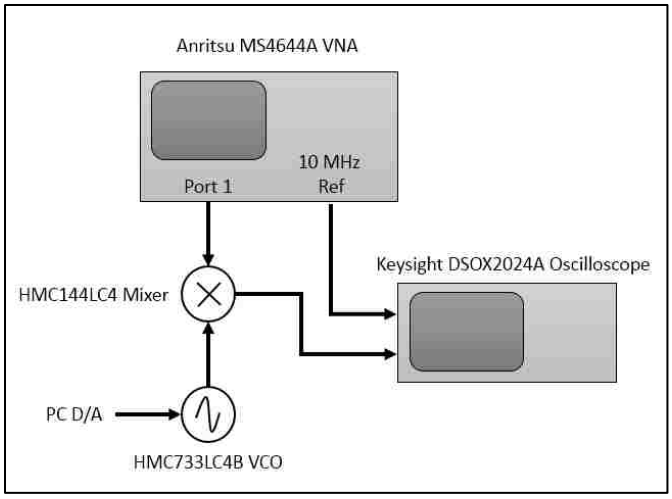


Figure 10. Experimental test setup for measuring frequency output from HMC733LC4B VCO.

measurements. Additionally, a 10-MHz reference signal was used (from the VNA) to trigger the oscilloscope, in order to phase-lock the VNA and the oscilloscope.

The frequency of the VCO was swept 1000 times at 6 frequency points. The high number of sweeps was chosen to emulate how the microwave camera sweeps frequency hundreds of times for a single measurement frame. At each frequency point in the sweep, the time domain signal was recorded by the oscilloscope and then divided into 8 parts. This means that each frequency in the experiment was recorded 8000 times. Since the VCO output frequency was highly susceptible to measurement setup and ambient conditions in the environment, the experiment was conducted three times.

Figure 11 shows histogram plots for each frequency in the range of sweep from the final experiment. The histograms are centered at 0 MHz, which means the VCO output frequency plotted in the histogram was referenced to the theoretical value, where a 0 MHz value meant the actual and theoretical values were the same. These histograms show that the VCO output frequency is normally distributed for all points in the sweep, and the only

differences are in the standard deviation. The standard deviation in output frequency for all frequency points and experiments is tabulated in Table 3. In general, standard deviation first increases with frequency points in the sweep then decreases slightly at the end. This can be attributed to the tuning sensitivity reported in the VCO datasheet, where the sensitivity increases first then decreases over the tuning voltage range that was used to generate the 10 – 15 GHz frequency sweep [15]. As the experiments were repeated, the standard deviation for all frequencies decreased. While there were variations in the standard deviation for all frequencies and experiments, the results show that for this particular VCO, one should expect frequency uncertainty that follows the normal distribution where the standard deviation will be in the hundreds of kilohertz.

Using the statistical distribution derived from these experiments, simulated lines scans were performed similar to the first simulations in Section 3, but the uniform distribution was replaced with a normal distribution shown below:

$$\Delta f \sim Normal(0, 488.5\ KHz). \tag{12}$$

In this equation, the frequency uncertainty is normally distributed with zero-mean and standard deviation of 488.5 KHz. The standard deviation value was chosen because it was the highest reported value from the statistical distribution experiment and would therefore produce the highest possible $l^2$-norm. The result of this simulation is shown in Figure 12. In this figure, frequency uncertainty is held constant, but the target range location is varied for the same values used in Section 3. In this figure, $l^2$-norm never increases above the -20 dB threshold. These experiments show that for SAR imaging for NDT applications, frequency uncertainty from this VCO will not significantly affect image quality.

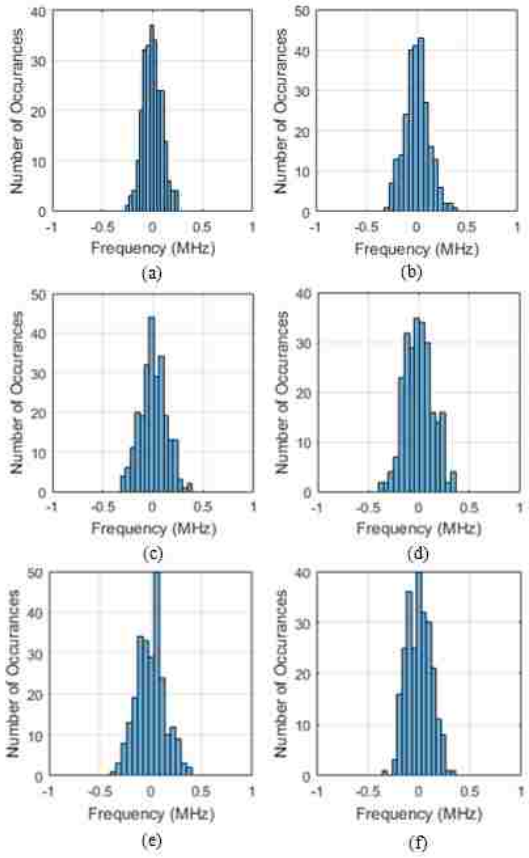


Figure 11. Histogram plots of HMC733LC4B output frequency at localized frequencies: (a) 10 GHz, (b) 11 GHz, (c) 12 GHz, (d) 13 GHz, (e) 14 GHz, and (f) 15 GHz.

Table 3. Standard Deviation (KHz) in HMC733LC4B Output Frequency

| **Trial** | **Frequency (GHz)** | | | | | |
|---|---|---|---|---|---|---|
| | ***10*** | ***11*** | ***12*** | ***13*** | ***14*** | ***15*** |
| ***1*** | 154.1 | 193.4 | 261.1 | 282.0 | 320.8 | 488.5 |
| ***2*** | 104.9 | 135.6 | 175.5 | 222.9 | 240.6 | 202.3 |
| ***3*** | 96.3 | 129.4 | 147.9 | 175.3 | 188.5 | 153.7 |

## 6. CONCLUSION

Image distortions created by instrumentation-based frequency uncertainty were quantified for different levels of frequency uncertainty and target range. A threshold was found based on these two parameters for when image distortions begin to degrade image

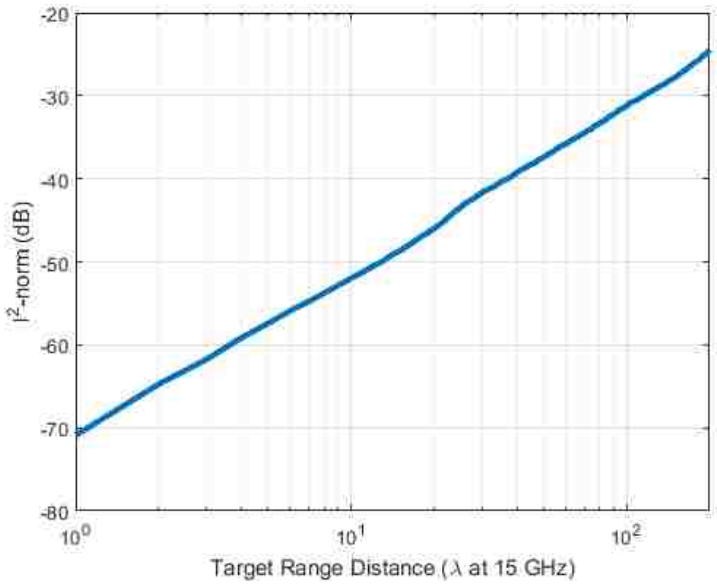


Figure 12. Simulation results of $l^2$-norm of a point target with fixed frequency uncertainty standard deviation of 488.5 KHz and different target ranges.

quality. In simulation, $l^2$-norm increased as a function of both parameters. Measurement results showed a similar trend with higher $l^2$-norm overall. Statistical distribution measurements showed the actual level of frequency uncertainty in the tested VCO will produce $l^2$-norm that is lower than -20 dB in SAR-generated images for NDT applications. This study also provides a roadmap by which to measure frequency uncertainty in an instrument following the procedure and results reported in this study to determine image distortion expectation and suitability for NDT SAR-based imaging.

## ACKNOWLEDGMENT

The authors would like to thank Dr. Akim Adekpedjou from the Department of Mathematics and Statistics at Missouri University of Science and Technology (S&T) for his valuable comments and discussions during the preparation of this paper.

## REFERENCES

[1] M. T. Ghasr, M. A. Abou-Khousa, S. Kharkovsky, R. Zoughi, and D. Pommerenke, "Portable Real-Time Microwave Camera at 24 GHz," IEEE Transactions on Antennas and Propagation, vol. 60, pp. 1114-1125, 2012.

[2] M. T. Ghasr, S. Kharkovsky, R. Bohnert, B. Hirst, and R. Zoughi, "30 GHz Linear High-Resolution and Rapid Millimeter Wave Imaging System for NDE," IEEE Transactions on Antennas and Propagation, vol. 61, pp. 4733-4740, 2013.

[3] M. T. Ghasr, M. J. Horst, M. R. Dvorsky, and R. Zoughi, "Wideband Microwave Camera for Real-Time 3-D Imaging," IEEE Transactions on Antennas and Propagation, vol. 65, pp. 258-268, 2017

[4] J. T. Case, M. T. Ghasr, and R. Zoughi, "Optimum Two-Dimensional Uniform Spatial Sampling for Microwave SAR-Based NDE Imaging Systems," IEEE Transactions on Instrumentation and Measurement, vol. 60, pp. 3806-3815, 2011.

[5] J. T. Case, M. T. Ghasr, and R. Zoughi, "Optimum 2-D Nonuniform Spatial Sampling for Microwave SAR-Based NDE Imaging Systems," IEEE Transactions on Instrumentation and Measurement, vol. 61, pp. 3072-3083, 2012.

[6] J. T. Case, M. T. Ghasr and R. Zoughi, "Nonuniform Manual Scanning for Rapid Microwave Nondestructive Evaluation Imaging," IEEE Transactions on Instrumentation and Measurement, vol. 62, pp. 1250-1258, 2013.

[7] M. Pichler, A. Stelzer, P. Gulden, C. Seisenberger, and M. Vossiek, "Phase-Error Measurement and Compensation in PLL Frequency Synthesizers for FMCW Sensors I: Context and Application," IEEE Transactions on Circuits and Systems I: Regular Papers, vol. 54, pp. 1006-1017, 2007.

[8] T. Grosch, "Correcting nonlinear modulation error in linear FMCW radar systems," in 2017 IEEE Radar Conference (RadarConf.), 2017, pp. 1577-1581.

[9] M. Horst, M. T. Ghasr, and R. Zoughi, "Effect of instrument frequency uncertainty on wideband microwave synthetic aperture radar (SAR) images," in 2017 IEEE International Instrumentation and Measurement Technology Conference (I2MTC), 2017, pp. 1-5.

[10] Y. Q. Liu, Y. D. Luo, and Y. Z. Xie, "An high-efficiency positioning method for ground testing SAR system," in IET International Radar Conference 2015, 2015, pp. 1-5.

[11] N. Marechal, "A terrain elevation error model for stereometric SAR systems engineering," in 2008 42nd Asilomar Conference on Signals, Systems and Computers, 2008, pp. 497-504.

[12] J. Ding and S. Zhang, "Impact of antenna directing jitter in bistatic SAR," in Microwave and Millimeter Wave Circuits and System Technology (MMWCST), 2012 International Workshop on, 2012, pp. 1-4.

[13] J. Wu, J. Xiong, Y. Huang, and J. Yang, "Analysis of PRF Jitter in Bistatic SAR," in 2006 CIE International Conference on Radar, 2006, pp. 1-4.

[14] F. T. Ulaby, Richard K. Moore and A.K. Fung, Microwave Remote Sensing: Active and Passive vol. II: Artech House, 1986.

[15] Analog Devices. (2018, January 9). HMC733LC4B [Online]. Available: http://www.analog.com/media/en/technical-documentation/data-sheets/hmc733.pdf

# II. DESIGN OF A COMPACT V-BAND TRANSCEIVER AND ANTENNA FOR MILLIMETER WAVE IMAGING SYSTEMS


## ABSTRACT

In this paper, we introduce a synthetic aperture radar (SAR) based millimeter wave imaging system for high-resolution imaging of human skin, in addition to traditional nondestructive testing (NDT) applications. The imaging system, which operates in the 58-64 GHz frequency range, forms the basic building block of a future millimeter wave camera suitable for imaging burned skin and skin cancers. The system is composed of a coherent transceiver and two antennas, principally enabling a quasi mono-static measurement configuration. The designed antenna is an antipodal Vivaldi antenna (AVA) with 5.0-8.0 dB gain and half-power beamwidths of ~79.0° and ~76.0° in its E and H planes, respectively. The transceiver is designed using a complete System-on-Chip (SoC) transmitter and receiver capable of I/Q detection. The fully-designed imaging system has 47 dB of dynamic range and is phase-calibrated using a robust wideband calibration procedure based on single frequency SAR imaging approach. Examples of images produced with this system include burned porcine skin and a small balsa wood panel with four small embedded rubber pieces.


## 1. INTRODUCTION

Microwave and millimeter wave nondestructive imaging based on synthetic aperture radar (SAR) reconstruction techniques can produce high resolution, 3D images of complex dielectric structures for many critical nondestructive testing (NDT), security, and biomedical applications [1]-[4]. Recent technological advances have enabled designing and developing portable, real-time and 3D image-producing systems (i.e., cameras) [5]-

[6]. Recently, microwave and millimeter wave SAR imaging has shown great promise as a valuable tool for human skin diagnosis, as well [3]. Diagnosis of skin injuries, such as burns, can benefit from SAR imaging, since currently the most prominent diagnosis method is visual inspection by a physician, which is subjective and not very accurate [7]. Previous investigations have shown that imaging in the V-band (50-75 GHz) of the millimeter wave frequency range has shown promise for human skin diagnosis [3], [8]-[10]. Operating in the V-band has three primary benefits for this application, namely: *i)* high image resolution for accurate characterization of skin injury, *ii)* electrically sensitive to individual layers of skin, and *iii)* low penetration depth [3].

Many of the previous studies involving millimeter waves have relied on commercial hardware such as bulky vector network analyzers (VNAs) and stationary imaging systems for collecting the imaging data. The full-body millimeter wave imaging system reported in [4] was designed for security applications, and it employed multiple transmitter and receiver circuits operating in parallel for electric field sampling. With this hardware architecture, the system transmits amplitude modulated signals from the transmitters and receive phase coherent data via quadratic receivers. However, the overall hardware architecture and size of this system is not conducive for developing a portable medical diagnostic tool. To date, cameras similar to those reported in [5]-[6] that operate at millimeter wave frequencies and provide portability and real-time diagnosis of skin have yet to be developed.

If portable, high-resolution millimeter wave imaging is to eventually become the diagnostics method of choice for skin disease assessment, a self-contained millimeter wave camera must be developed similar to current portable medical diagnostics devices.

Consequently, the objective of this investigation has been to develop the basic building block for a portable and high-resolution millimeter wave imaging camera suitable for human skin diagnosis. The system is composed of two primary parts, namely: *i*) a coherent transceiver, and *ii*) a specially-designed antenna suitable for fulfilling the stringent design requirements for this application. The transceiver controls the millimeter wave signal transmission and reception for recording the imaging data, while the antenna serves as the irradiating element facilitating transmission and reception of signals. Together, these components form a complete quasi mono-static imaging system with a small form-factor that can be mounted on an automated scanning platform for mechanical raster scanning. The system can ultimately be converted into a millimeter wave camera in the future by transforming the designed antenna into a switched 2D array for real-time image production without the need for mechanical scanning [5]-[6].

System design parameters as well as the design, fabrication, and testing methods of the antenna and transceiver are provided in the following section. Next, the calibration procedure for the system is described. This constitutes a major portion of this overall endeavor, since as will be explained, calibrating the designed antenna and transceiver is not a straightforward (or standard) process. Finally, representative imaging results, using the complete imaging system, are provided illustrating the system's suitability for millimeter wave imaging of human skin, in addition to imaging for traditional NDT applications.

## 2. SYSTEM DESIGN

To arrive at a proper design of a millimeter wave imaging system for human skin diagnosis, several design parameters (requirements) must firstly be defined, namely: *i)*

operating frequency range, *ii)* electric field spatial sampling, *iii)* antenna radiation pattern, *iv)* multiplexing scheme, and *v)* reflection measurement methodology. The first three parameters influence the design of the antenna, and the last two parameters influence both the design of the antenna and transceiver.

Operating frequency range is primarily determined by the application requirements. The primary factor that influences the choice of frequency range is the application of human skin imaging, which was previously mentioned in the Introduction. However, the operating frequency range also influences the quality of images generated by an imaging system. Center frequency determines image cross-range resolution, while the bandwidth of frequencies determines the range resolution while improving the signal-to-noise ratio (SNR) in SAR generated images. Finally, antenna design, particularly its overall size which is critical in this case, is primarily determined by the frequency range.

Electric field spatial sampling also heavily influences the antenna design [11]. This parameter is particularly important for designing the antenna for future integration into a 2D imaging array system [11], [6]. The optimal spatial sampling requirement for SAR imaging is one-quarter ($\frac{\lambda}{4}$) of the operating wavelength (measured at mid-band) [11]. This means that when the antenna is placed in a 2D array, its overall dimensions should be small enough so that the spacing among the array elements is as close to one-quarter wavelength as possible. However, it is often not possible to design an antenna with such dimensional constraints, while having acceptable wideband matching properties (i.e., efficiency) and radiation pattern (i.e., beamwidth and gain). In practice, it has been shown that operating with a sample spacing of one-half wavelength ($\frac{\lambda}{2}$) is sufficient to generate high-resolution images without significant aliasing-caused image distortions [12], [13]. Thus, for this

imaging system, the antenna is designed with overall dimensions as close to one-half wavelength as possible.

Antenna radiation pattern is an important parameter with respect to SAR image formation. The designed antenna must have a sufficiently directive (i.e. not omnidirectional) radiation pattern, so the radiated electric fields are directed towards the sample under test and not the undesired surrounding areas (e.g., imaging system hardware, operator, etc.). Additionally, the directive radiation pattern must have a sufficiently wide main lobe with low sidelobe levels to effectively benefit from the spatial focusing of SAR [14].

Multiplexing scheme is another important consideration for designing an imaging system which can ultimately be converted into a camera using a 2D array. This influences how the signals received by the antennas, configured in a 2D array, are routed and recorded. One approach is to use a multiplexer network of microwave monolithic integrated circuit (MMIC)-based switches to route signals between *one* transceiver and a 2D array of antennas [6]. Another approach is to have a transceiver for each antenna in the 2D array. Finally, a third approach is to use a combination of the first two approaches [4].

For the final design parameter, reflection measurement methodology, there are two primary approaches, namely: quadratic demodulation and interferometry. Quadratic demodulation produces phase coherent imaging data via a quadrature receiver (I/Q detection) [4]. For this approach, isolation between transmitter and receiver, when routing signals to and from the antenna, is critically important for obtaining SAR images with high SNR. One method to achieve good isolation between transmitter and receiver is when two like antennas are used, where one antenna connects to the output of the transmitter, and the

other antenna connects to the input of the receiver. In this configuration, and when the two antennas are near one another, the system operates in quasi mono-static mode [12], [13]. However, depending on the antenna geometry, antennas placed close together can be susceptible to a high level of mutual coupling and thus low isolation. Unlike the quadratic demodulation approach, interferometry employs Schottky diode-based detectors (i.e., mixers) to produce phase coherent imaging data [6]. With this approach, the concern about the isolation between the transmitted and received signals is no longer an issue, since the diode requires both signals to function properly [1]. The choice between these two approaches is primarily dictated by the state-of-the-art in solid-state diode design technologies in the desired operating frequency range.

Recently, complete system-on-chip (SoC) transmitters and receivers, operating within the V-band frequency range, have been developed for communication applications [15]-[16]. These developments are fueled by the latest designation of the unlicensed V-band for short-range, large bandwidth communication, satellite (i.e., backhaul, etc.) [17]-[18]. SoC transmitters and receivers are capable of transmitting and receiving signals in the same manner as the system reported in [4], but in a smaller overall package.

Based on the above parameters and the introduction of SoC transmitters and receivers produced primarily for V-band communication applications, a transceiver and an antenna were designed, for this SAR imaging application, in the 58–64 GHz frequency range. The frequency range was chosen based on specific SoC transmitters and receivers that are commercially available and are discussed in detail in the Transceiver Design section. The transceiver is built based on a quadratic demodulation scheme with one discrete transmitter and one receiver, where two antennas are implemented in a quasi

mono-static configuration. The system is designed with the multiplexer methodology of one transceiver and a multiplexer network of MMIC switches connected to a 2D antenna array, which allows for future conversion into a camera. An antipodal Vivaldi antenna was designed based on its ability to meet the antenna-specific design parameters listed above. Together, the transceiver and antenna form a complete building block of an imaging system suitable for imaging human skin.

### 1.1. ANTIPODAL VIVALDI ANTENNA DESIGN

After investigating many different antenna types to meet the many design requirements described above and equipped with significant experience in designing high-frequency printed circuit board (PCB)-based Vivaldi-style antennas for wideband SAR imaging, the antipodal Vivaldi antenna (AVA) was selected [19]-[24]. This is an inherently wideband antenna, sufficiently directive (i.e., sufficient efficiency and gain), and can be arranged into a compact linear array placed on the edge of a PCB, where multiple arrays can then be stacked on top of each other to form a switched 2D array [6], [24]. In this context, the width of the antenna is defined as the dimension of the antenna along the edge of the PCB when placed in the configuration mentioned previously. Antenna length is the second dimension in the plane of the PCB. Consequently, antenna width determines electric field spatial sampling. This configuration is beneficial with respect to spatial sampling, since it allows for antenna width to be as large as one wavelength. When multiple linear arrays of this antenna are stacked to form a 2D array, each array alternates between transmitting and receiving for quasi mono-static imaging. For example, the lowest array contains all of the transmitting antennas, and the array directly above it contains all of the receiving antennas, followed by another array of transmitting antennas. If all antennas are

designed one wavelength wide and the receiving antenna arrays are shifted by one-half wavelength, the sample spacing is effectively one-half wavelength, similar to [12]. Therefore, scattered electric fields can be sampled at one-half wavelength even though the antenna is one wavelength wide. This configuration also ensures the relatively directional radiation pattern of the antenna does not interfere with the RF circuitries placed on the same PCB (behind the antenna). Additionally, the AVA provides great design flexibility as a function of the desired operating frequency range.

Although an AVA is a good antenna candidate for this purpose, to fulfill all specific design requirements for this imaging system, some critical modifications had to be made to a "standard" AVA, as described here, and as shown in Figure 1. The antenna was designed on Rogers RO5880 substrate with a dielectric constant of 2.2 and thickness of 0.254 mm. A substrate with relatively low dielectric constant (compared to Rogers RO4350B with dielectric constant of 3.48) allows for lower reflections at the aperture of the antenna for propagating electric fields. The antenna is composed of a grounded coplanar waveguide (GCPW) input, substrate integrated waveguide (SIW) section, balanced radiator composed of two radiating fins, and a dielectric lens. In Figure 1, the top layer of the antenna contains the top ground plane, microstrip line, and the top radiating fin. The bottom layer contains the bottom ground plane and the bottom radiating fin. A GCPW feed was chosen for this antenna, since the antenna was intended to be integrated with millimeter wave switches when placed in a 2D array, in which case relatively easy access to the feed line is required. The vias used in the GCPW and SIW were chosen to be 0.254 mm in diameter with 0.127 mm annular ring, which is the distance from the via hole to the edge of the top ground plane. These dimensions were at the limit of the current

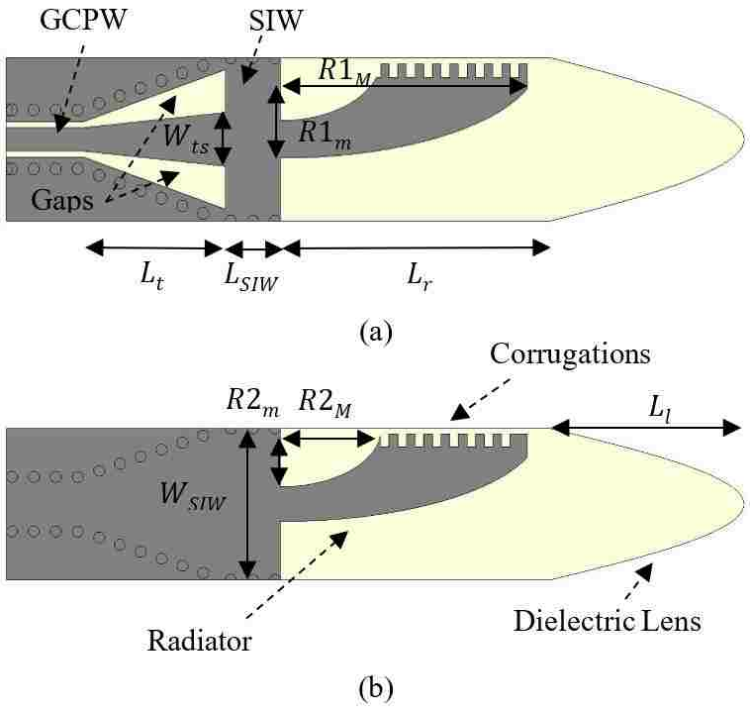


Figure 1. Geometry of antenna (a) top layer ($L_t$ = 3.30 mm, $L_{SIW}$ = 1.28 mm, $L_r$ = 6.25 mm, $W_{ts}$ = 1.15 mm, $W_{SIW}$ = 3.50 mm, $R1_M$ = 5.72 mm, $R1_m$ = 2.81 mm) and (b) bottom layer ($L_l$ = 5.00 mm, $R2_M$ = 2.40 mm, $R2_m$ = 0.92 mm).

capabilities of the commercial fabrication company used to manufacture the antenna. The microstrip line width and the gaps between the microstrip and the top ground plane were chosen to be 0.50 mm and 0.127 mm, respectively, to achieve a line impedance of 53.28 Ω. This was the closest impedance to 50 Ω while maintaining a microstrip line width that is narrow enough to connect to millimeter wave switch terminals.

An SIW was chosen to feed the radiator for several key reasons. It has inherently lower loss than microstrip feeds and can operate in a wider range of frequencies similar to traditional waveguide structures [19]. Furthermore, an SIW is inherently a balanced transmission line (TRL), which is required for properly feeding a balanced AVA. The GCPW input was transitioned to SIW by slightly widening the microstrip line.

Additionally, the gaps between the top ground plane and the microstrip line were widened, so that the final combined transitioned width of the microstrip line and the gaps on either side of it was approximately the same width as that of the SIW. This type of transition concentrates the electric field between the microstrip line and bottom ground plane, minimizing the reflection at the input of the SIW. The length of the transition, final width of the microstrip line, and final width of the gaps were optimized, using CST Microwave Studio®, to minimize the overall reflection coefficient (i.e., matching characteristics) within the desired 58-64 GHz operating frequency range.

The edges of the radiating fins were designed using two elliptical shapes. The larger ellipse defines the leading edge of the fin with its major and minor radii ($R1_M$ and $R1_m$) along the length and width of the antenna, respectively. Similarly, the smaller ellipse defines the trailing edge of the fin with radii ($R2_M$ and $R2_m$) defined in a similar manner. While some AVAs are designed with no trailing edge (i.e. $R2_M = R2_m = 0$), one was implemented in this design to improve impedance matching bandwidth (i.e., efficiency) and to reduce sidelobe levels. When simulating the design of the radiating fins, it was noticed that the surface currents tended to travel back to the feed on the outer edges of the fins. This resulted in poor reflection coefficient and increased sidelobe levels. To mitigate these undesired effects, corrugations (0.20 mm long by 0.30 mm deep) were incorporated into the outer edges of the radiating fins.

Finally, a dielectric lens, placed at the end of the radiator, was incorporated into the design to concentrate electric fields in the lens, which in effect results in smaller spatial sampling distance between adjacent antennas. The electric field radiated from an AVA is polarized along the width of the antenna. When the electric field travels from the radiator

to the dielectric/free-space boundary, defined by the shape of the lens, the electric field sees an effectively larger aperture. While the addition of the lens increases the overall antenna gain, it also lowers its operating frequency range. This is advantageous since for a specific frequency, the antenna width can be reduced to have a smaller electric field spatial sampling, as required for SAR imaging. The resulting length of the lens was 5 mm, and the width of the lens is the full width of the antenna. The lens shape was defined by a cosine function. With a dielectric lens, the antenna was designed to be 3.5 mm wide ($\sim\frac{3}{4}\lambda$ at 61 GHz), while maintaining good matching characteristics and radiation pattern. This width is greater than $\frac{\lambda}{2}$ at 61 GHz (2.50 mm), but when the antenna is placed in a 2D array with shifted rows mentioned previously, the effective electric field spatial sampling becomes half of the antenna's width (1.75 mm), which is less than $\frac{\lambda}{2}$.

Figure 2 shows the simulation model of the designed antenna and the reflection coefficient with and without the dielectric lens and with and without corrugations. The antenna was simulated in CST Microwave Studio® as a 5-element array, where there were two like antennas on each side of the radiating antenna. These side antennas were included, to account for the influences of neighboring antennas on the radiation pattern of the radiating antenna, in consideration of the fact that eventually this antenna will be configured in an array. While the radiating antenna was matched at its input feed with a simulation wave port, the side antennas had no wave ports attached to their input feeds (i.e. open-circuit termination). This would reflect any signal that is coupled from the radiating antenna. The reason for terminating the side antennas in this way is that most millimeter wave switches also reflect signals traveling through the side antennas. Since this antenna was designed to be implemented in a switched antenna array, it was critical that all antenna

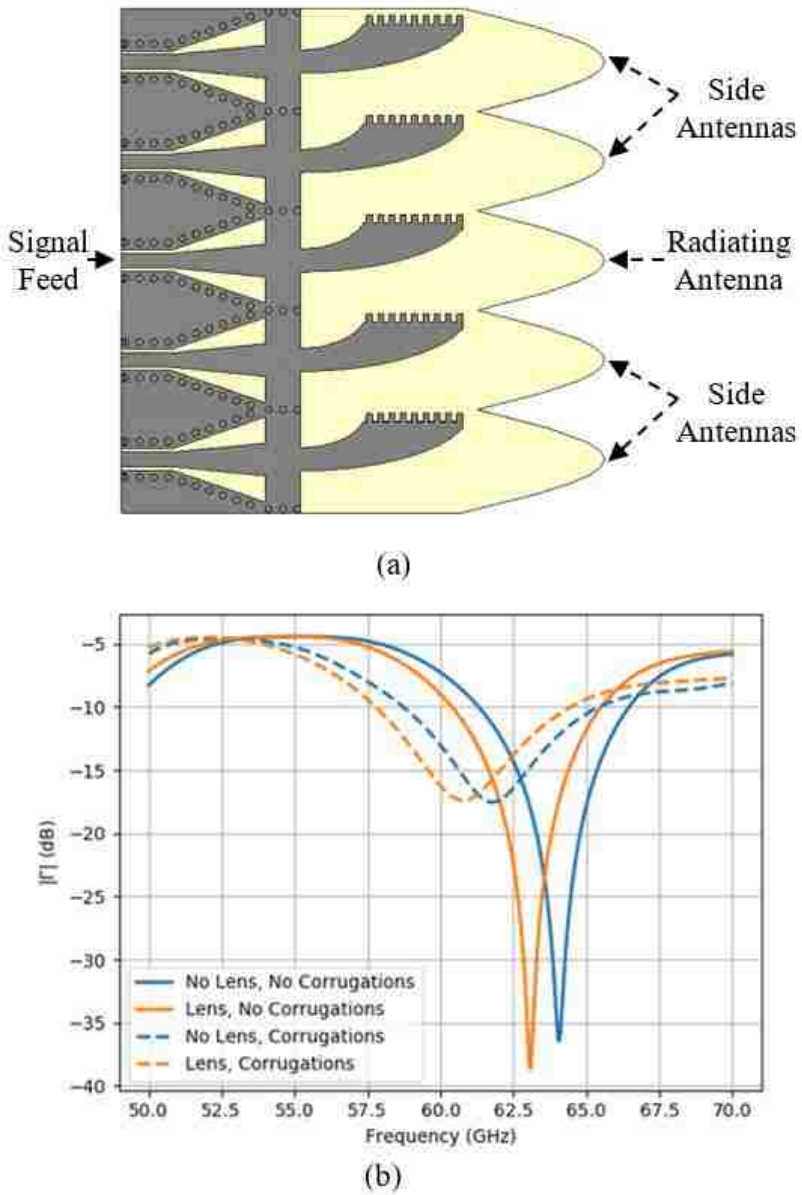


Figure 2. (a) Simulation model of designed antenna with dielectric lens and corrugations (top view), (b) Reflection coefficient for designed antenna with and without the dielectric lens and with and without corrugations.

input feed terminations be simulated to match the terminations in a switched array. As shown in Figure 2, without the corrugations and lens, the antenna has a resonant response at 64 GHz with an approximately 3 GHz of (i.e., -10 dB) bandwidth. The addition of a dielectric lens alone shifts the reflection coefficient response lower in frequency by

approximately 1 GHz, and the bandwidth remains the same. When corrugations are added without a dielectric lens, the resonance becomes less shallow. However, the response shifts lower in frequency, and the -10 dB bandwidth increases to 6 GHz. Finally, the addition of both dielectric lens and corrugations results in an operating range of 58-64 GHz (i.e., $|\Gamma| <$ -10 dB).

Antenna far-field pattern was simulated to determine the overall radiation pattern for all four configurations, as shown in Figure 3. The results clearly show that without the corrugations, there is substantial sidelobe radiation in the H-plane and wider beamwidth in the E-plane, which is most evident at 58 GHz. Without the dielectric lens, higher sidelobe radiation in the H-plane is seen, which is most evident at 64 GHz. In general, for both frequencies shown, corrugations have a higher influence than the dielectric lens on sidelobe reduction in the H-plane. Overall, the addition of both the dielectric lens and corrugations reduces sidelobe radiation and increases the directivity of the antenna. The E- and H-plane radiation patterns are directional with sidelobe levels of approximately -8 to -10 dB (compared to the main lobe). The half-power E- and H-plane beamwidths are on average 79.0° and 76.0°, respectively.

The influence of the dielectric lens and corrugations is also shown in plotted gain across frequency in Figure 4. The results show that the addition of corrugations significantly increases antenna gain at lower frequencies, since the corrugations reduce H-plane sidelobe radiation significantly at lower frequencies. Furthermore, the addition of a dielectric lens increases antenna gain at higher frequencies, which can be attributed to the much larger electrical aperture created by the lens, particularly at higher frequencies. With both dielectric lens and corrugations, the gain ranges from approximately 5 dB to 8 dB and

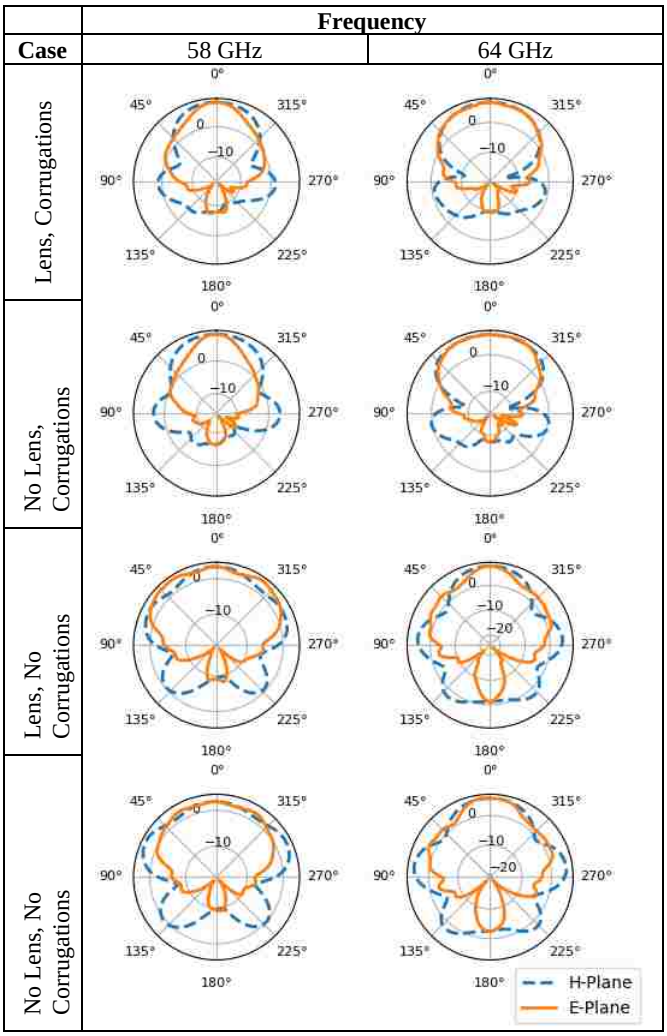


Figure 3. Simulated far-field E-plane (orange) and the H-plane (blue) patterns.

decreases slightly with frequency. The decrease in gain across frequency is due the corrugations influencing antenna gain more than the dielectric lens.

Finally, isolation between two like antennas having both the dielectric lens and the corrugations was simulated for quasi- monostatic imaging, as shown in Figure 5. For this simulation, the 5-element array, with one radiating middle antenna, was duplicated and arranged for quasi mono-static imaging with 3.5 mm ($\sim\frac{3}{4}\lambda$ at 61 GHz) of spacing between the two boards. This distance was as small as possible while maintaining enough space for

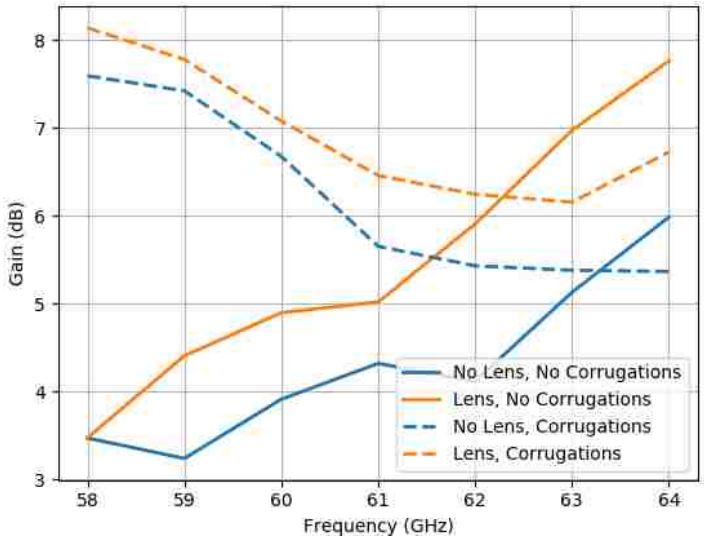


Figure 4. Antenna gain with and without the dielectric lens and with and without corrugations.

when connectors are attached to the antennas. Figure 5b shows the simulated isolation between the two radiating middle antennas of both arrays. The isolation ranges from -25dB to -35 dB across the operating frequency range. This level of isolation is sufficient for good SNR when collecting imaging data with this antenna.

After the AVA was simulated and optimized, it was fabricated as a 5-element array, as shown in Figure 6, where the top side of the antenna is shown. The middle antenna is fed by a 1.85 mm end-launch PCB connector. Additionally, the four side antennas are left open-circuit at their inputs to match the model used in the simulation. The reflection coefficient of the antenna was measured using an Agilent N5227A (10 MHz-67 GHz) Performance Network Analyzer (PNA). To measure reflection coefficient, a single port of the PNA was calibrated, and the measurement was conducted with the antenna radiating into free-space, as shown in Figure 7. When comparing these results to simulation, where the simulated antenna has both dielectric lens and corrugations, the measurements follow

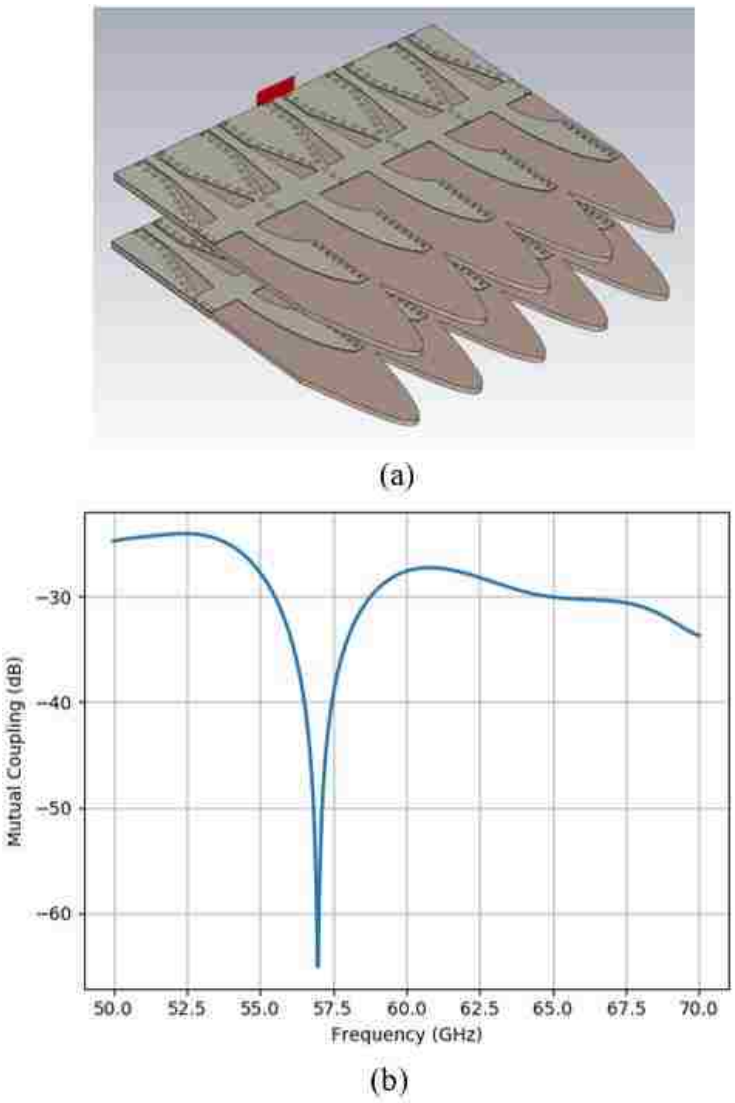


Figure 5. Simulated isolation between like antennas: (a) simulation model with 3.5 mm (3/4 λ at 64 GHz) of space between the two boards, and (b) results.

the same wideband response, but do not exactly match simulation results. The -10 dB bandwidth of the antenna is shifted lower in frequency (57-63.75 GHz). Additionally, the reflection coefficient within the operating band is lower in comparison to simulation. This difference can be attributed to losses in the PCB.

Since access to a millimeter wave antenna range was not available for this investigation, the antenna radiation properties were determined by conducting an imaging


Figure 6. Fabricated antenna with the middle element being fed while the other four are left open.

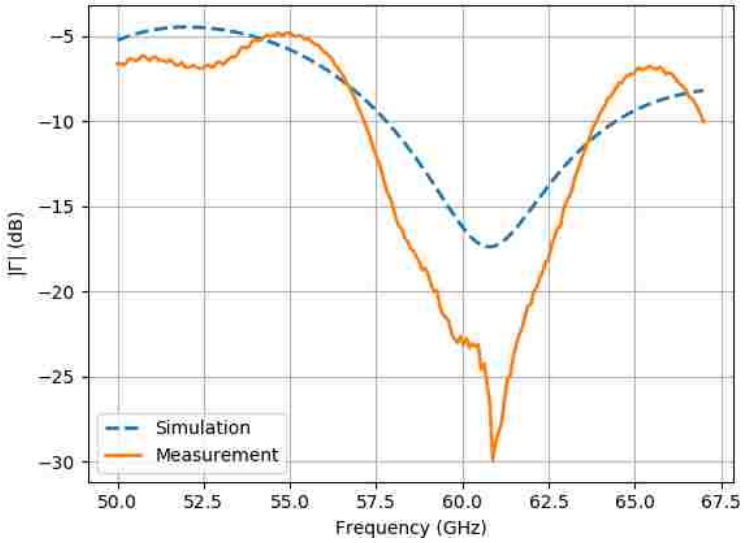


Figure 7. Simulated and measured reflection coefficient for the antenna.

test on a “known” target. By imaging a “known” target and processing the SAR image, the quality of the target in the image gives an indication of the quality of the antenna radiation pattern. For example, a highly-focused image of a target indicates directive radiation with wide beamwidth [14]. For these reasons, a single antenna was used in a monostatic imaging configuration to test its radiation pattern [25]. For this test, the antenna was used to scan over a small metal sphere of 0.5 mm diameter ($\sim\frac{\lambda}{10}$ at 61 GHz), which is commonly used

to characterize SAR imaging systems [11]. The scan was made on a 40 mm x 40 mm area in 1 mm increments in each direction, where the metal sphere was place 20 mm below the antenna. The antenna was connected to the Agilent PNA for collecting data in the 58-64 GHz frequency range. Next, an image of the metal sphere was produced using the well-known ω-*k* SAR algorithm [2], [11].

The SAR-generated image of the metal sphere is shown in Figure 8. The halo around the metal sphere is attributed to the construction foam that the sphere was embedded into during the imaging process. The 3 dB spot width of the metal sphere was calculated according to the procedure outlined in [11], and the result was a spot width of 1.75mm, which is 0.355$\lambda$ at 61 GHz. Considering the scan size, sample spacing, and distance from measurement grid to the metal sphere, this spot width matches theoretical expectation [11]. These results show that the antenna is suitable for millimeter wave SAR imaging, as described herein.

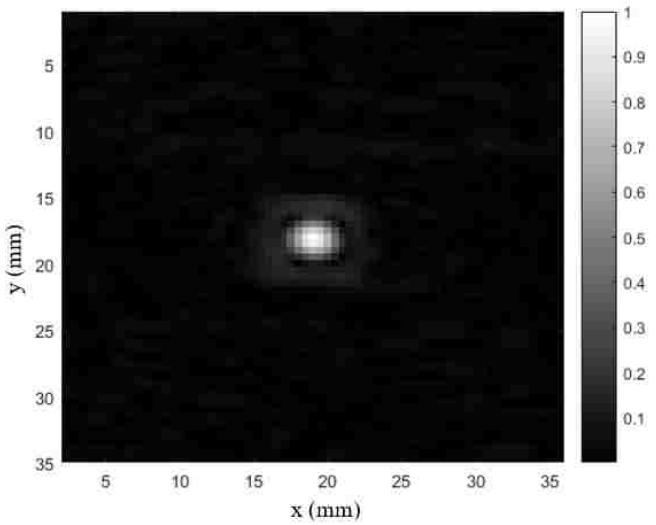


Figure 8. SAR image of a small metallic sphere made with the fabricated antenna.

## 1.2. TRANSCEIVER DESIGN

The transceiver was designed based on quadratic demodulation with an SoC HMC6300 transmitter chip and SoC HMC6301 receiver chip [15], [16]. The HMC6300 chip has a typical output power of 15 dBm, and the HMC6301 chip has a receiver gain of 0 dB to 69 dB depending on gain control settings [15], [16]. These chips can operate in the 57-64 GHz frequency range, but the frequency range was slightly lowered to 58-64 GHz to accommodate the operational frequency range of the antenna. A block diagram of the major components of the transceiver is shown in Figure 9. It consists of these two chips, a local oscillator (LO), hybrid coupler, and 100 MHz intermediate frequency (IF) source. The transmitter and receiver chips function as an up-mixer and down-mixer, respectively. Although these chips have built-in oscillators for LO, using a single external LO ensures exact phase and frequency match between chips. The LO is a voltage-controlled oscillator (VCO) with a phase-locked loop (PLL) referenced to a crystal oscillator (XO) at 100 MHz, where the PLL was implemented to ensure the LO would not drift in frequency during a scan. A Keysight DSOX2024A oscilloscope was used as a three-channel analog-to-digital converter (ADC), which can be replaced by a few MMIC-based ADCs and integrated into the transceiver for future camera design considerations.

The imaging measurement begins with an IF signal, which is a 100 MHz continuous wave signal from the crystal oscillator, fed into the hybrid coupler. Then, the I and Q outputs of the coupler are fed into the transmitter. The LO is tuned to a single frequency within the 16.3-18.3 GHz operating band and also fed into the transmitter. Inside the transmitter, the LO is split into two signals, where one signal is frequency multiplied by three (3xLO) and the second signal is frequency divided by two (LO/2). The I and Q

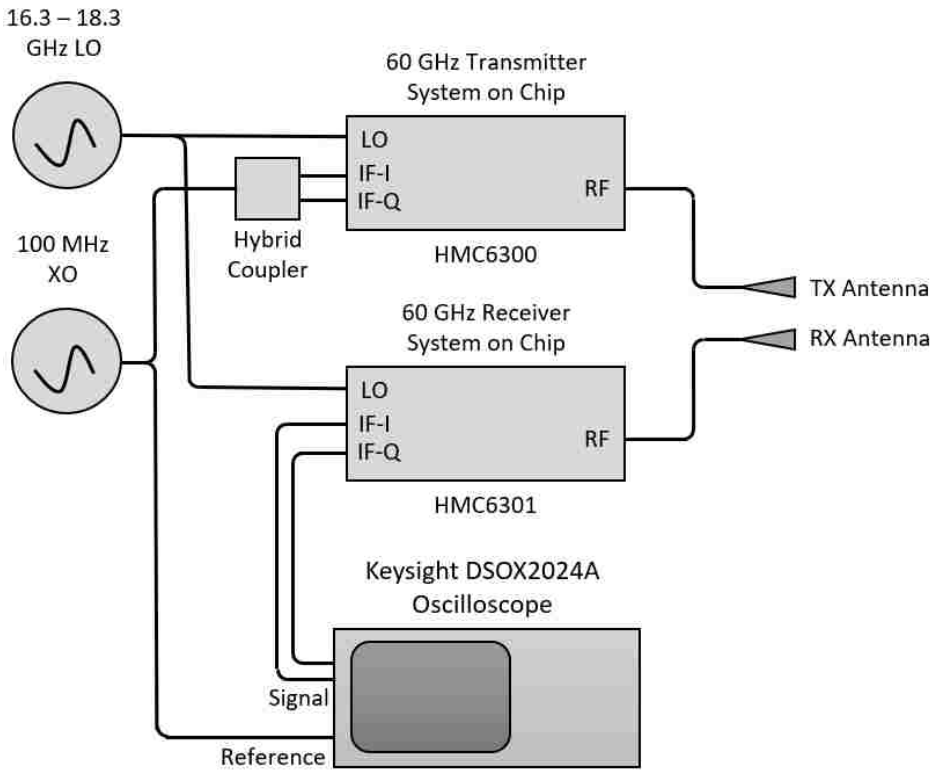


Figure 9. Block diagram of transceiver.

signals are fed into an image-reject mixer and mixed with the LO/2 signal. The output is then fed into a standard mixer and mixed with the 3xLO signal. After filtering and amplification, the result is an upper-sideband amplitude-modulated signal in the 58-64 GHz frequency range. This signal is transmitted from the TX antenna, and the RX antenna receives the reflected signal from a target. The received signal is then down-mixed to IF in the receiver using the same process performed in the transmitter but in reverse. The output of the image-reject mixer within the receiver produces I and Q signals, which are fed into two channels of the oscilloscope. Additionally, a portion of the 100 MHz source is fed into the third channel of the oscilloscope as a reference signal. The received I and Q signals are phase-referenced to the reference signal, so there is phase coherence across all measurements when imaging with the system. These signals are then recorded by the

oscilloscope and sent to a PC. In the PC, the I and Q signals are filtered through a 100 MHz band-pass filter and then match filtered with the reference to obtain the vector (real and imaginary) effective reflection coefficient. This value is then used for SAR imaging. This procedure is repeated in a stepped-frequency continuous-wave modulation scheme, where the individual frequency points are chosen by tuning the LO.

The fabricated transceiver is shown in Figure 10. The transceiver is composed of several PCBs and has an overall size of approximately 90 mm x 90 mm x 170 mm. The local oscillator and control hardware for the transmitter and receiver chips reside on

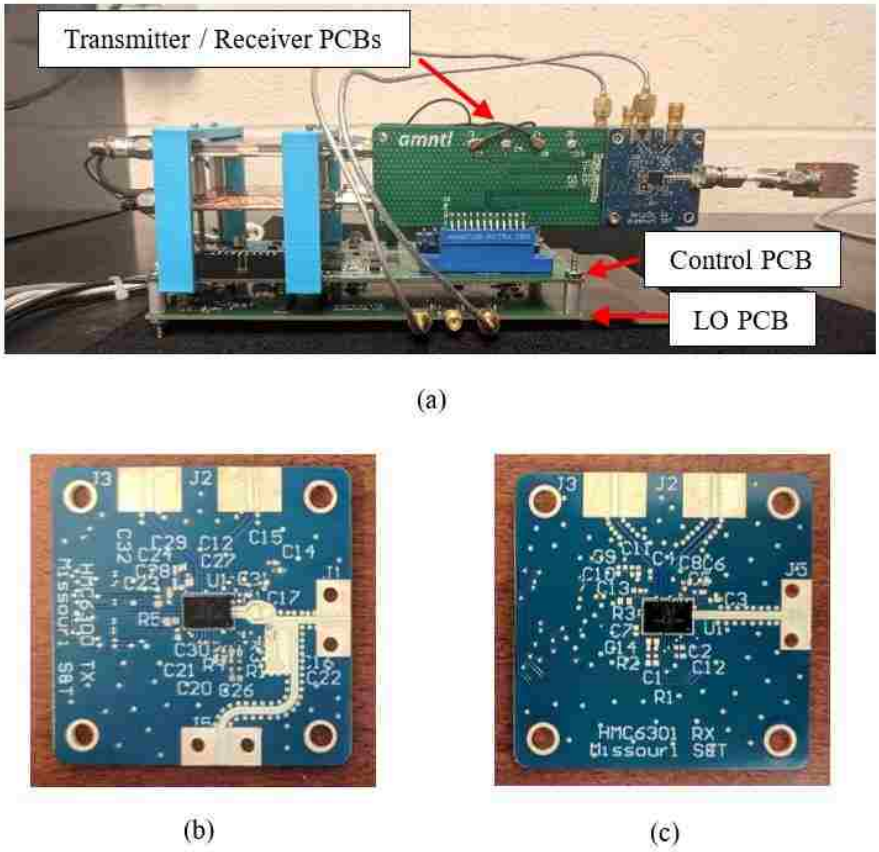


Figure 10. Fabricated transceiver: (a) fully assembled with antennas attached, (b) transmitter PCB before component population and (c) receiver PCB before component population.

separate low frequency PCBs using FR-4 substrate. The transmitter and receiver chips are attached to a PCB with a custom high frequency stack-up and are shown in Figure 10(b) and Figure 10(c), respectively. The stack-up has four signal layers with a 6.6 mil Rogers 4350B substrate between the top two layers and FR-4 between the remaining lower layers. The transmitter and receiver PCBs attach to the control PCB vertically with daughter boards. Finally, a PC interfaces with this system through two FTDI FT2232D USB interface chips located on the control and LO boards [26].

Once the full system was assembled, its overall dynamic range was measured. When the settings of the transmitter and receiver chips were first configured, the receiver was saturated by the transmitter. This is due to the initial maximum gain set in the receiver and electromagnetic interference (EMI) between the transmitter and receiver chips, 1.85 mm connectors, and TX and RX antennas. Therefore, the receiver gain was lowered before the dynamic range was calculated. The dynamic range was then calculated for the 58-64 GHz frequency range at seven linearly spaced frequency points. This number of points was chosen since the system uses seven frequency points when producing SAR images, as will be explained later. The system dynamic range was calculated by subtracting (in dB-scale) the minimum detectable signal (MDS) from the strongest received signal, where the MDS was found by measuring the system noise and adding 3 dB to it. System noise was first measured by positioning a high frequency absorber approximately 80 mm in front of the system, so little to no signal would be detected by the receiver. The received signal was then measured multiple times. The variance of the received signal across multiple recordings was calculated to determine the noise power, and the MDS was calculated afterwards. Next, the strongest received signal was measured by transmitting and receiving

against a large metal plate located 10 mm away from the TX and RX antennas. Subsequently, the system dynamic range was calculated for the seven measured frequencies, as shown in Figure 11. The results show that the dynamic range varies between 44 dB and 50 dB, being approximately 47 dB on average. This dynamic range is lower than what is achievable in the HMC6301 chip when used for communications applications. In these applications, receivers use automatic gain control to adjust internal amplifier settings to maximize gain. Thus, the HMC6301 can achieve a dynamic range up to 69 dB [16]. However, for imaging applications, internal amplifier gain cannot be set high due to the EMI issues described previously. However, 47 dB of dynamic range is more than sufficient for SAR imaging, especially in human skin imaging applications at ~60 GHz, where the skin is positioned close to the imaging system. Further improvements to dynamic range can be made by reducing the coupling between transmitter and receiver allowing for increased receiver gain.

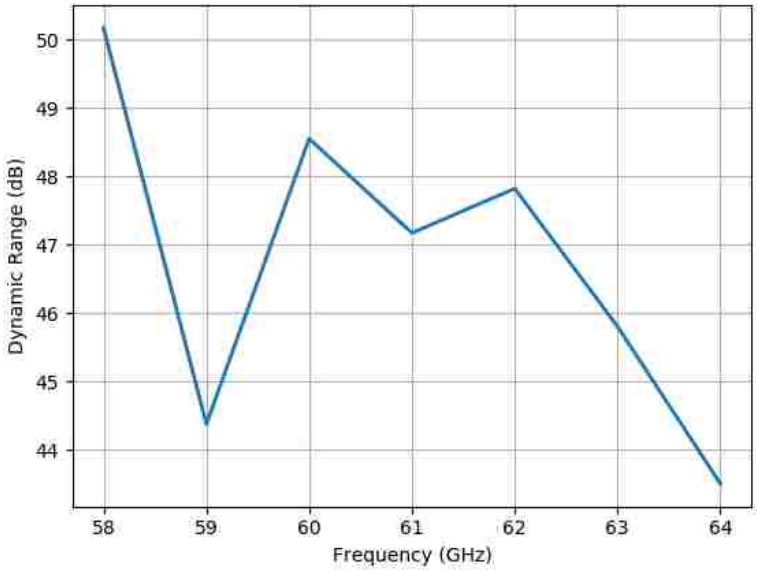


Figure 11. Dynamic range of the system.

# 3. SYSTEM CALIBRATION

Subsequent to calculating the system dynamic range, the imaging system needed to be phase-calibrated across the 58-64 GHz operating frequency range prior to conducting imaging tests. Phase calibration is the procedure of determining the overall phase response of the imaging system as a function of frequency and removing this phase response before applying the SAR imaging algorithm. Depending on the antenna type used and other system specifications, phase calibration (or correction) is not a trivial task, and extensive amount of work has been performed for phase calibrating SAR imaging and radar systems. One effective phase calibration technique involves scanning a "known" target, such as a metal plate, a metal pole, a metal sphere, or a corner reflector. The expected phase is then calculated based on the knowledge of target reflectivity (in particular, scattering phase) and the physical configuration of the measurement setup (i.e., distance to target, etc.) [13], [27]-[29]. This approach requires precise knowledge of the distance between the imaging system and the "known" target and often requires multiple measurements to eliminate the influence of multiple reflections.

Another calibration technique is to perform transmission-through measurements for bi-static imaging systems [5], [30]. In this procedure, phase calibration can be performed by removing the phase due to signal travel distance in air between transmitter and receiver, where the remaining phase can be calibrated out.

While these calibration techniques are viable for many radar applications, they cannot be applied to the imaging system developed for this investigation. Transmission through calibration cannot be applied, since the two antennas are arranged in a quasi mono-static configuration. Furthermore, the calibration procedures outlined in [13], [27]-[29] are time consuming and thus cannot be used for the following reasons.

In this imaging system, there are multiple signal phases that contribute to the overall phase response of the system. While many traditional antenna topologies, such as a waveguide probe, can be accurately phase-calibrated across a wide frequency band using well-known methods, the AVA design for this investigation has a phase center that moves along and across the antenna as a function of frequency. Furthermore, the transmission-through phase response in the transmitter and receiver chips are highly dependent on the digital gain settings of the amplifiers and attenuators internal to the chips. Finally, a phase exists between the TX and RX antennas, that are positioned in a quasi mono-static configuration, where it can vary if the distance between the antennas changes slightly. Since there are many sources contributing to the overall phase response of the imaging system and the phase response can change with the slightest change in measurement setup, a fast calibration procedure must be developed that can be employed before or after every imaging event.

The concept of using SAR imaging for calibration has been employed previously for amplitude-based radar cross-section (RCS) calibration of known targets for air-borne imaging systems [31]. Additionally, Auto Focus SAR employs SAR imaging for phase calibration, but this technique is typically used in scenarios when there are unknown phases at each measurement location and not within the imaging system itself [32]. Finally, SAR imaging has been used to calibrate target location (RCS angular dependency) for Multistatic SAR imaging systems using relatively large targets [33]. In these investigations, the imaging systems were either narrow band, or the phase response of the imaging system was not considered to be frequency dependent. Applying phase calibration for the wideband imaging system described in this investigation becomes much more

cumbersome due to fact that scattering from any "known" target will have a frequency dependent phase response.

For these reasons, a robust wideband calibration procedure was developed to phase-calibrate the imaging system across the operating frequency range, which can be applied quickly before or after an imaging event. This procedure utilizes single frequency SAR imaging of a "known" target to determine the phase response required to phase-calibrate the system for each frequency point across the operating frequency range.

The calibration procedure starts with a single frequency line scan of an electrically small target, such as a metal sphere, where the schematic of such a scan is shown in Figure 12. Measurements are performed along the $x$-axis, and the target is placed in the $xz$-plane, where measurement points and the metal sphere are located at ($x$,0) and ($x_t$,$z_t$), respectively. The spatial sampling distance between the measurement points, $\Delta_x$, is $\frac{\lambda}{4}$. The reflected signal at the measurement points follows the round-trip free-space Green's function:

$$D(x) = \left(\frac{1}{R^2}\right) e^{-j(2kR+\phi)}. \tag{1}$$

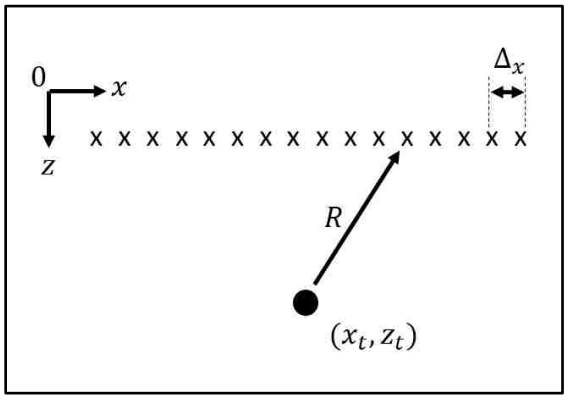


Figure 12. Line scan setup for calibration.

$$R = \sqrt{(x - x_t)^2 + z_t^2}. \quad (2)$$

For an imaging system that is not phase-calibrated, there exists an unknown phase, $\phi$ , as shown in equation (1). For practical imaging systems, the phase is different for each frequency point in the operating range. When the single frequency SAR image of the known target is formed, the indication of the target is (must be) located at ($x_t$,$z_t$). At this location in the image, the corresponding complex image value represents the reflectivity of the target and is shown in the following equation, where $\rho$ and $\theta$ represent physical reflectivity magnitude and phase of the target:

$$\Gamma = \rho e^{j(\theta+\phi)}. \quad (3)$$

One property of single frequency SAR imaging is that the unknown phase, $\phi$, is added to the phase response of the target in the SAR image. This term can be found by subtracting the expected phase ($\theta$) from the phase calculated in the image ($\theta + \phi$) to find $\phi$. This procedure can then be repeated for all frequency points in the operating frequency range to form a vector representing the phase values (i.e., $\phi$, as a function of frequency). Finally, the measured imaging data is divided by the vector of phases ($\phi$) with respect to frequency to remove the phase response of the imaging system.

For this imaging system, seven frequency points, linearly spaced across 58-64 GHz, were chosen. Having a high number of frequency points allows for high unambiguous target range and high SNR in SAR images. However, due to the phase-locked-loop in the LO, tuning the system to a particular frequency takes considerable time. Therefore, seven frequency points were chosen to optimize SNR and the overall measurement time. The proposed calibration setup is shown in Figure 13. A metal wire with a diameter of 0.78 mm was chosen to be the “known” target instead of a small metal sphere. Metal spheres are

often impractical to use as a "known" target for two reasons, namely: *i)* low return signal amplitude, and *ii)* difficulty of positioning without introducing additional scattering sources (e.g., construction foam). However, when the AVA scans over the metal wire with electric field polarization oriented perpendicular to the length of the wire, the phase response of the wire is quite close to the response of a metal sphere with same diameter. This is illustrated in Figure 14, where the phase responses of the metal wire and metallic sphere were simulated in CST Microwave Studio® and compared.

Single frequency scans were conducted for each frequency point using a synthetic aperture width of 160 mm at 1 mm spatial sampling distance. The wire was positioned 40 mm away from the antennas. Next, the mean of the raw imaging data was subtracted from the scan data for each frequency to remove the direct coupling signal caused by the EMI (coupling) between the transmitter and receiver. Finally, single frequency SAR images were formed, and the uncalibrated phase of the wire was found for each frequency. This

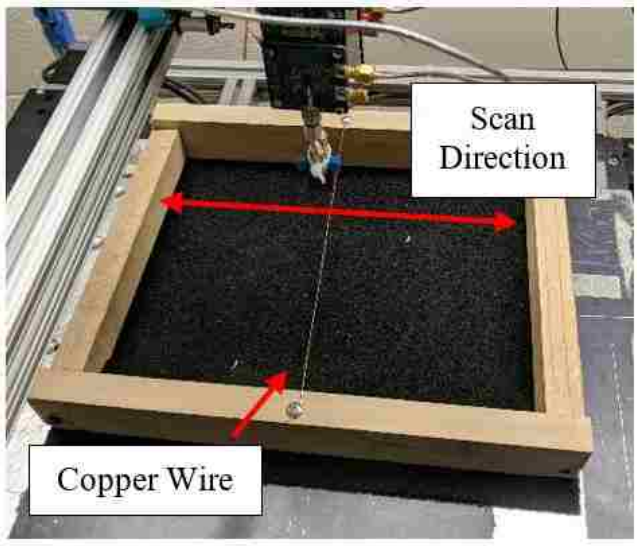


Figure 13. Calibration setup for phase referencing.

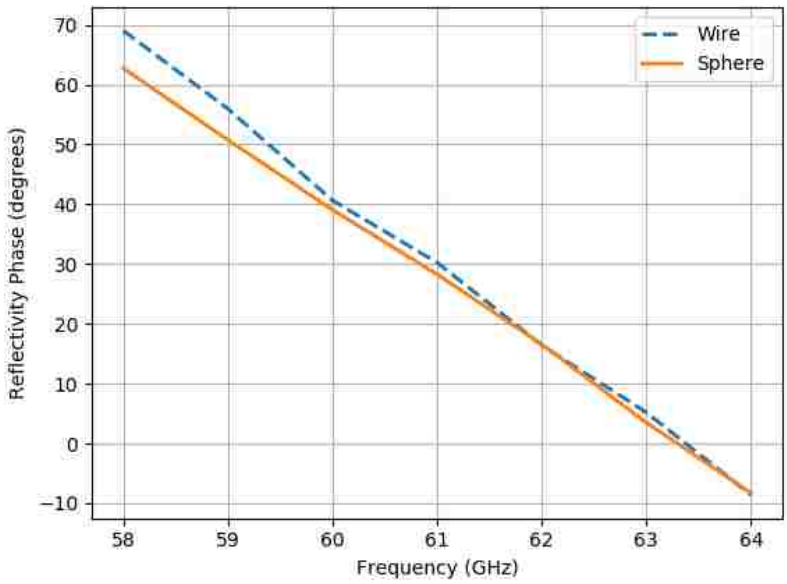


Figure 14. Phase response for a thin wire and a small metal sphere.

procedure was conducted for three trials to achieve a mean phase response. Figure 15 shows the phases obtained from the SAR images, which do not follow the linear trend (as expected) in Figure 14, and must therefore be calibrated. In Figure 15, the standard deviation in the phase response (indicated by the error bars) is at most 5°, which shows that the phase response of the system is relatively stable over the course of an imaging event. Both sets of information were used to phase-calibrate the system, and the results of this calibration procedure are shown in Figure 16. In this figure, the horizontal and vertical axes represent the *x* and *z* directions, respectively. The image in Figure 16(a) shows the wideband SAR image of the wire with no phase correction (i.e., calibration) applied. In contrast, Figure 16(b) shows the same wideband SAR image after the proposed phase correction was applied. Compared to the image in Figure 16(a), the indication of the wire is quite clear with an SNR of 20 dB, which is higher than the first image (15 dB).

Finally, to demonstrate the utility of this calibration procedure with respect to image quality, a 2D scan was performed on four rubber circles glued between two pieces of balsa

wood. The balsa wood dimensions are 105 mm x 76 mm x 12 mm, and the four rubber circles are 5 mm in diameter. This test was conducted to determine the qualitative improvement the calibration procedure has on imaging data after the imaging system has been calibrated. The balsa wood was positioned 20 mm below the imaging system, and the system scanned over a 100 mm x 120 mm array at 1 mm increments. After the scan was

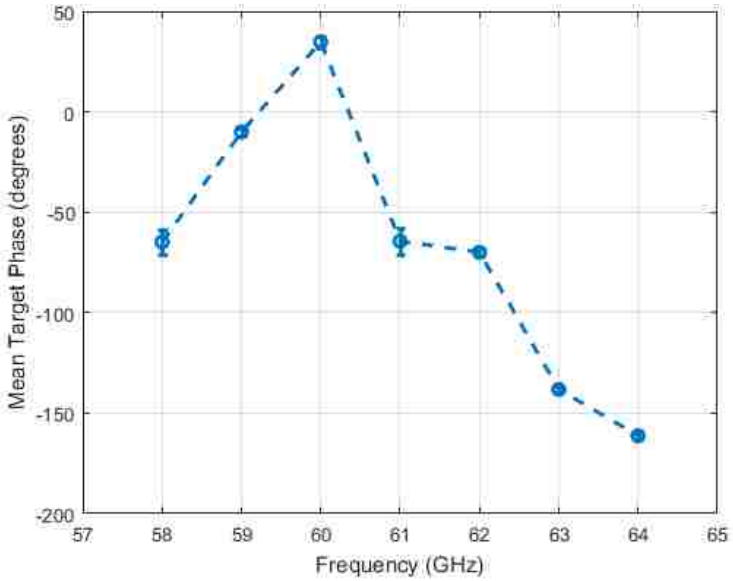


Figure 15. Uncalibrated phase of wire reflectivity obtained from single frequency SAR images.

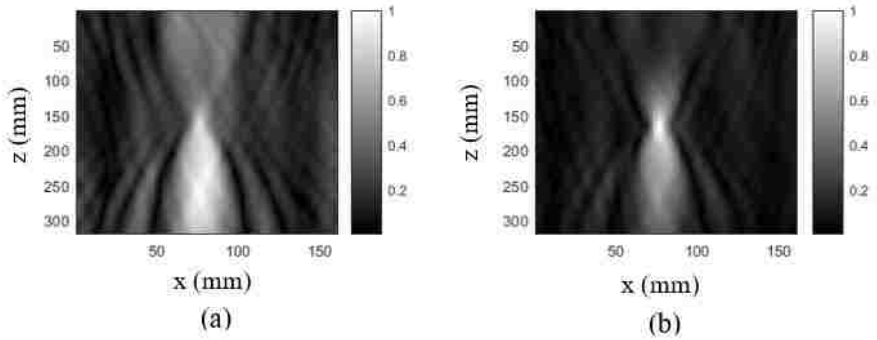


Figure 16. Calibration results: (a) wideband image before calibration (SNR = 15 dB), (b) wideband image after calibration (SNR = 20 dB).

completed, the mean of the raw imaging data was subtracted to remove the direct coupling signal caused by EMI between the transmitter and receiver, and any other constant scattering from the environment, from the imaging data. This was performed for all imaging tests. Finally, the calibration was applied to the imaging data before SAR processing. The image domain used the coordinates *x*, *y*, and *z* to match the coordinates used previously. After SAR processing, images were generated of the balsa wood with and without calibration.

Figure 17 shows the results of this imaging experiment. Figure 17(a) shows a picture of the balsa wood. Figure 17(b) and Figure 17(c) show the indications of the four rubber circles without calibration and with calibration, respectively. In the uncalibrated image, the four rubber circles are shown, but with a relative high noise level, as seen in the image. However, the calibrated image shows the four rubber circles clearly with much lower image noise. These results clearly show the utility of this procedure for this system and wideband radar systems in general. These results also show how this system can be used for imaging for NDT applications.

## 4. IMAGING RESULT

Once phase calibration was completed, the imaging system was used to perform a 2D scan on a piece of pigskin that was burned similar to the pigskin imaged in [3]. The sample of pigskin used was 140 mm x 140 mm, and a 15 mm diameter circular burn was made in the center of the sample. The burn was made to approximate a second degree burn similar to [3]. The sample of pigskin was placed 20 mm below the imaging system and scanned. Figure 18(a) shows the setup of the burned pigskin, and Figure 18(b) shows the image of the burn. The indication of the burn is clear, where the shape and size are

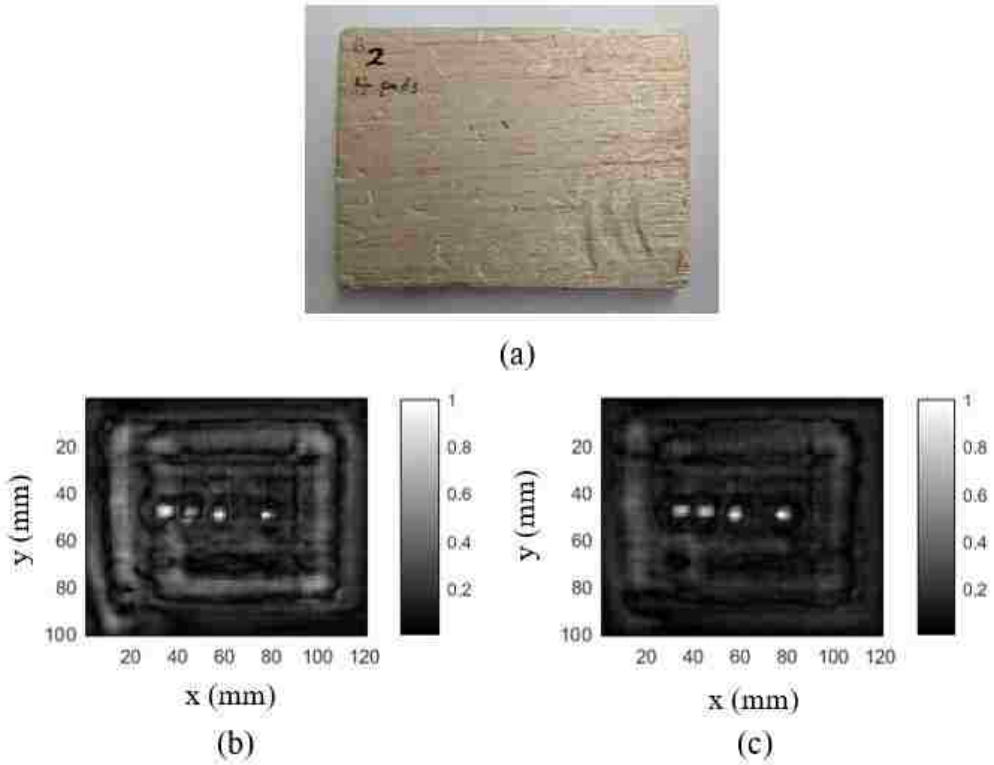


Figure 17. Image of balsa wood containing four rubber circles. (a) Picture of balsa wood, (b) uncalibrated image, (c) calibrated image.

representative of the actual burn. There are also some intensity variations in the burn image indicative of uneven burn within that region. The distortions at the edges of the image are caused by the wrinkles in the pigskin. The results clearly indicate the viability of this system as a building block of a 2D millimeter wave camera which can be designed (in the future) for skin health assessment and diagnosis.

## 5. CONCLUSION

A quasi mono-static millimeter wave SAR-based imaging system consisting of a transceiver and two antipodal Vivaldi antennas was designed and fabricated for human skin diagnosis and high-resolution NDT applications. The system is designed as the basic building block of a millimeter wave camera and can be converted into a camera by

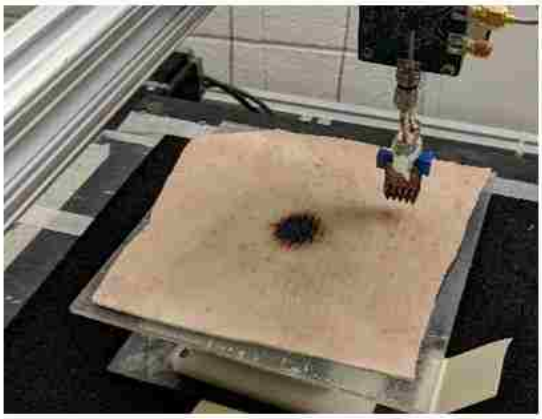

(a)

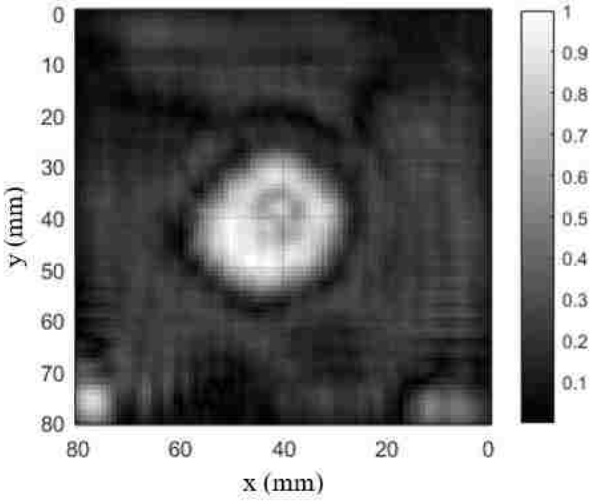


(b)

Figure 18. (a) Scan setup with burned pigskin. (b) Image of burn in pigskin.

replacing the two antennas with a switched 2D antenna array. Simulation and experimental results of the designed antipodal Vivaldi antenna demonstrated its suitability for millimeter wave SAR imaging. A robust wideband calibration procedure was developed for the imaging system, due to the system's complex phase response. From the calibration procedure, it was shown that the system is suitable for the intended imaging applications, as indicated by images of a burn in pigskin and hidden objects in a balsa wood panel.

Further investigations will involve improvements to the dynamic range of the transceiver and integration with a switched 2D array forming a millimeter wave camera.

## REFERENCES


[1] M. T. Ghasr, J. T. Case, and R. Zoughi, "Novel Reflectometer for Millimeter-Wave 3-D Holographic Imaging," *IEEE Transactions on Instrumentation and Measurement,* vol. 63, pp. 1328-1336, 2014.

[2] D. M. Sheen, D. L. McMakin, and T. E. Hall, "Three-dimensional millimeter-wave imaging for concealed weapon detection," *IEEE Transactions on Microwave Theory and Techniques,* vol. 49, pp. 1581-1592, 2001.

[3] Y. Gao and R. Zoughi, "Millimeter Wave Reflectometry and Imaging for Noninvasive Diagnosis of Skin Burn Injuries," *IEEE Transactions on Instrumentation and Measurement,* vol. 66, pp. 77- 84, 2017.

[4] S. S. Ahmed, A. Schiessl and L. P. Schmidt, "A Novel Fully Electronic Active Real-Time Imager Based on a Planar Multistatic Sparse Array," *IEEE Transactions on Microwave Theory and Techniques*, vol. 59, no. 12, pp. 3567-3576, Dec. 2011.

[5] M. T. Ghasr, M. A. Abou-Khousa, S. Kharkovsky, R. Zoughi, and D. Pommerenke, "Portable Real-Time Microwave Camera at 24 GHz," *IEEE Transactions on Antennas and Propagation,* vol. 60, pp. 1114-1125, 2012.

[6] M. T. Ghasr, M. J. Horst, M. R. Dvorsky, and R. Zoughi, "Wideband Microwave Camera for Real-Time 3-D Imaging," *IEEE Transactions on Antennas and Propagation,* vol. 65, pp. 258-268, 2017.

[7] A. D. Jaskille, J. C. R. Roman, J. W. Shupp, M. H. Jordan, and J. C. Jeng, “Critical review of burn depth assessment techniques: Part I. Historical review,” J. Burn Care Res., vol. 30, no. 6, pp. 937–947, Nov. 2009.

[8] A. Mirbeik-Sabzevari, S. Li, E. Garay, H. T. Nguyen, H. Wang and N. Tavassolian, "Synthetic Ultra-High-Resolution Millimeter-Wave Imaging for Skin Cancer Detection," *IEEE Transactions on Biomedical Engineering*.

[9] D. Oppelt, J. Adametz, J. Groh, O. Goertz and M. Vossiek, "MIMO-SAR based millimeter-wave imaging for contactless assessment of burned skin," *2017 IEEE MTT-S International Microwave Symposium (IMS),* Honololu, HI, 2017, pp. 1383-1386.

[10] F. Topfer and J. Oberhammer, "Millimeter-Wave Tissue Diagnosis: The Most Promising Fields for Medical Applications," *IEEE Microwave Magazine*, vol. 16, no. 4, pp. 97-113, May 2015.

[11] J. T. Case, M. T. Ghasr, and R. Zoughi, "Optimum Two-Dimensional Uniform Spatial Sampling for Microwave SAR-Based NDE Imaging Systems," *IEEE Transactions on Instrumentation and Measurement*, vol. 60, pp. 3806-3815, 2011.

[12] M. T. Ghasr, S. Kharkovsky, R. Bohnert, B. Hirst, and R. Zoughi, "30 GHz Linear High-Resolution and Rapid Millimeter Wave Imaging System for NDE," *IEEE Transactions on Antennas and Propagation*, vol. 61, pp. 4733-4740, 2013.

[13] M. A. Baumgartner, M. T. Ghasr, and R. Zoughi, "Wideband Imaging Array Using Orthogonally Fed Dual Varactor-Loaded Elliptical Slots," *IEEE Transactions on Instrumentation and Measurement*, vol. 64, pp. 740-749, 2015.

[14] D. M. Sheen, et al, "Wide-bandwidth, wide-beam width, high resolution, millimeter wave imaging for concealed weapon detection", Proc. SPIE in Passive and Active Millimeter-Wave Imaging XVI, vol. 8715, pp. 871509, May. 2013.

[15] Analog Devices. (2018, June 11). *HMC6300* [Online]. Available: http://www.analog.com/media/en/technical-documentation/data-sheets/HMC6300.pdf

[16] Analog Devices. (2018, June 11). *HMC6301* [Online]. Available: http://www.analog.com/media/en/technical-documentation/data-sheets/HMC6301.pdf

[17] C. H. Park and T. S. Rappaport, "Short-range wireless communications for next-generation networks: UWB, 60 GHz millimeter wave PAN, and Zigbee," *IEEE Wireless Communications Magazine*, vol. 14, no. 4, pp. 70–78, Aug. 2007.

[18] R. C. Daniels and R. W. Heath, Jr., "60 GHz Wireless Communications: Emerging Requirements and Design Recommendations," *IEEE Vehicle Technology Magazine*, vol. 2, no. 3, pp. 41-50, Sept. 2007.

[19] M. H. Bah, J. S. Hong, and D. A. Jamro, "UWB antenna design and implementation for microwave medical imaging applications," *2015 IEEE International Conference on Communication Software and Networks (ICCSN)*, , 2015, pp. 151-155.

[20] A. Mirbeik and N. Tavassolian, "Synthetic ultra-wideband antenna for high-resolution millimeter-wave imaging," *2015 IEEE International Symposium on Antennas and Propagation & USNC/URSI National Radio Science Meeting*, 2015, pp. 2093-2094.

[21] R. Kazemi, A. E. Fathy and R. A. Sadeghzadeh, "Dielectric Rod Antenna Array With Substrate Integrated Waveguide Planar Feed Network for Wideband Applications," *IEEE Transactions on Antennas and Propagation*, vol. 60, no. 3, pp. 1312-1319, March 2012.

[22] F. Taringou, D. Dousset, J. Bornemann and K. Wu, "Broadband CPW Feed for Millimeter-Wave SIW-Based Antipodal Linearly Tapered Slot Antennas," *IEEE Transactions on Antennas and Propagation*, vol. 61, no. 4, pp. 1756-1762, April 2013.

[23] M. Moosazadeh, S. Kharkovsky, J. T. Case and B. Samali, "Improved Radiation Characteristics of Small Antipodal Vivaldi Antenna for Microwave and Millimeter-Wave Imaging Applications," *IEEE Antennas and Wireless Propagation Letters*, vol. 16, pp. 1961-1964, 2017.

[24] M. Horst, M. T. Ghasr and R. Zoughi, "Design of a tapered slot-line antenna for wideband SAR imaging," *2016 IEEE International Symposium on Antennas and Propagation (APSURSI)*, Fajardo, 2016, pp. 1835-1836.

[25] A. Foudazi, T. E. Roth, M. T. Ghasr and R. Zoughi, "Aperture-coupled microstrip patch antenna fed by orthogonal SIW line for millimetre-wave imaging applications," *IET Microwaves, Antennas & Propagation*, vol. 11, no. 6, pp. 811-817, 5 12 2017.

[26] Future Technology Devices International Ltd. (2018, June 11). *FT2232D*. [Online]. Available: http://www.ftdichip.com/Support/Documents/DataSheets/ICs/DS_FT2232D.pdf

[27] G. L. Charvat, L. C. Kempel, E. J. Rothwell, C. Coleman, E. J. Mokole, "An ultrawideband (UWB) switched- antenna-array radar imaging system", *IEEE International Symposium on Phased Array Systems & Technology*, Waltham, MA, October 2010.

[28] Tan, Weixian, et al. "Array error calibration methods in downward-looking linear-array three-dimensional synthetic aperture radar." *Journal of Applied Remote Sensing* 10.2 (2016): 025010.

[29] J. T. Case, M. T. Ghasr and R. Zoughi, "Correcting Mutual Coupling and Poor Isolation for Real-Time 2-D Microwave Imaging Systems," *IEEE Transactions on Instrumentation and Measurement*, vol. 63, no. 5, pp. 1310-1319, May 2014.

[30] Yurduseven, Okan, et al. "Software calibration of a frequency-diverse, multistatic, computational imaging system." IEEE Access (2016): 2488-2497.

[31] F. T. Ulaby, Richard K. Moore and A.K. Fung, *Microwave Remote Sensing: Active and Passive* vol. II: Artech House, 1986.

[32] S. I. Kelly, M. Yaghoobi and M. E. Davies, "Auto-focus for under-sampled synthetic aperture radar," *Sensor Signal Processing for Defence (SSPD 2012)*, London, 2012, pp. 1-5.

[33] A. M. Chan, M. D. Casciato and P. K. Rennich, "Coherent calibration techniques for multistatic SAR image formation," *2008 European Radar Conference*, Amsterdam, 2008, pp. 324-327.

# III. A COMPACT MICROWAVE CAMERA BASED ON CHAOTIC EXCITATION SYNTHETIC APERTURE RADAR (CESAR)

## ABSTRACT

In this paper, we introduce a compact microwave camera based on a new synthetic aperture radar (SAR) imaging methodology with potential applications encompassing nondestructive testing (NDT) and security. The imaging methodology defined as Chaotic Excitation Synthetic Aperture Radar (CESAR), was developed specifically for microwave cameras, where all antennas irradiate a target *simultaneously* instead of traditional sequential irradiation. The benefit of CESAR is a significant reduction in required RF hardware, that is otherwise critical to previous system designs. However, the trade-off is a degradation of image quality that can be tolerated in some applications. The microwave camera developed for this study operates in the 23-25 GHz frequency range and is composed of 64 rectangular slot antennas fed with a two-stage power divider network. The divider network is composed of a corporate feed waveguide network and cavity dividers. The camera generates a *pseudo* plane-wave with ~7 dB and 35° of variation in magnitude and phase (compared to a plane-wave), respectively. The well-known $\boldsymbol{\omega}$-$\boldsymbol{k}$ SAR algorithm was consequently modified to properly focus images with the new imaging methodology. Experimental imaging results were produced for flaws in polylactic acid (PLA) and metallic object feature detection, highlighting the camera's suitability for NDT and security applications.

**Index Terms:** Synthetic aperture radar (SAR), microwave imaging, Nondestructive Testing, Simultaneous irradiation.

# 1. INTRODUCTION

Microwave and millimeter wave imaging methods, utlizing synthetic aperture radar (SAR), are capable of generating high-resolution, 3D images of complex dielectric structures for many critical nondestructive testing (NDT), biomedical, and security applications [1]-[3]. Basic microwave and millimeter wave SAR imaging, for NDT applications, employs a single reflectometer, composed of an RF transmitter, receiver, and antenna, attached to an automated scanning platform for mechanical raster scanning over a target [1]. Recent developments in microwave imaging technology have led towards the development of real-time microwave and millimeter wave imaging systems using imaging arrays in which each individual antenna transmits and receives sequentially using fast switching circuits [4]-[6]. These systems speed up imaging data acquisiton, while being readily portable for on-demand applications.

The SAR imaging methdology employed in these real-time imaging systems is based on sequentially transmitting electric fields and coherently measuring the reflections over a 2D plane [7]. Next, a microwave imaging algorithm (e.g., $\omega$-$k$ SAR) is employed to generate an image of a target [3], [7]-[8]. In general, the imaging system should produce data specifically for the chosen imaging algorithm. For example, if mono-static $\omega$-$k$ SAR is employed, the imaging system should be designed such that it provides reflection data at each spatial location on a 2D measurement grid, where each measurement is independent of all others. For imaging systems that employ antenna arrays, this typically requires high isolation between individual antenna elements, which can be accomplished through the use of microwave monolithic integrated circuit (MMIC) switches [4], independent transmitters/receivers, modulation schemes [5], [6], etc.

An example of an imaging system that is capable of generating high-resolution 2D and 3D images is the wideband microwave camera presented in [4]. This camera consisted of a switched antenna array of 256 tapered slot-line antennas, with a 20-30 GHz wideband voltage controlled oscillator (VCO). Microwave signals scattered by a target are then received via interferometers at the array elements [1]. Schottky detector/mixer diodes (herein refered to as Schottky diodes) were placed in pairs at the apertures of the tapered slot-line antennas, where they down-mixed the transmitted and received signals to baseband as input to the SAR imaging algorithm [1]. This effectively created 512 receivers whose baseband outputs were multiplexed at frequencies much lower than the microwave operating frequency band. Using Schottky diodes significantly reduced RF hardware complexity, since it eliminated RF multiplexers for the receiver channel and the additional down-mixing and detection stages that were otherwise required in [5]. Nevertheless, the system described in [4] used a wideband switching network composed of many single-pull-four-throw (SP4T) switches for routing the signal sequentially from the transmitter to each antenna in the imaging aray. While this switching network contributed to high isolation between antenna elements, it constituted a significant majority of the hardware cost, size, and complexities.

There are imaging applications where a high-fidelity microwave camera, such as the one reported in [4], may not be needed. Some examples include flaw detection along a Fiberglass or high-density polyethylene (HDPE) pipe, concealed contraband detection, and imaging human skin for burn and cancer detection [2]. In some cases, the location, basic dimensions, and dielectric contrast are sufficient to characterize the target of interest. Consequently, a microwave camera with much less complexity compared to previous

systems can be designed to achieve this desired information. Furthermore, a corresponding microwave imaging methodology, requiring much less hardware complexity and cost, can be developed specifically tailored to generating images for such applications. Developing a microwave camera with significantly less hardware complexity is also beneficial for reducing camera size and for operation at relatively high frequencies, where the commerical availability of switches and other components is significantly limited. Therefore, the goal of this investigation has been to develop a new microwave camera and imaging methodology capable of overcoming these complexities while producing reasonably high-resolution images for many different applications.

For this investigation a new microwave imaging methodology was developed and is named Chaotic Excitation Synethetic Aperture Radar (CESAR) for reasons that are discussed in Section 2. This new imaging methodology is founded on the principle of irradiating a target with a plane-wave and measuring the reflected signal with a 2D antenna array. It will be shown later that using a plane-wave to illuminate targets is crucial to reducing the complexity of the microwave camera as well as minimizing the necessary modifications to the existing SAR algorithms. With this new imaging methodology, a prototype microwave camera was designed and fabricated much smaller and less complex compared to previously-developed systems [4] based on the compact planar antenna array in [9].

There are a few major advantages to developing a microwave camera based on CESAR, namely: *i)* ability to generate SAR images with minimal modifications to the existing SAR algorithms, *ii)* significant reduction in microwave hardware, *iii)* ability to operate at higher (millimeter wave) frequencies, and *iv)* decreased measurement time.

However, as will be shown, these advantages come at the cost of: *i)* reduced image resolution, *ii)* low-level image distortions, *iii)* reduced imaging volume, and *iv)* reduced signal-to-noise ratio (SNR) in the resulting images. However, as stated earlier, given the desirous features of this new approach, for many practical applications these limitations may be acceptable.

## 2. CHAOTIC EXCITATION SYNTHETIC APERTURE RADAR

### 1.1. IMAGING MEASUREMENTS

In this section, the basic CESAR imaging methodology and accompanying image formulation are detailed with comparisons to traditional mono-static $\omega$-$k$ SAR. CESAR was derived from mono-static $\omega$-$k$ SAR, so it is important to first review the traditional imaging approach. Figure 1(a) shows an imaging diagram of mono-static $\omega$-$k$ SAR. In this figure, electric fields are sequentially transmitted and received (by reflections from the target) at each point on the measurement grid in a raster scan. For the purpose of deriving the image formation equations, the measurement grid is planar (i.e., two-dimensional) and lies in the X-Y plane. The measurement points are optimally spaced at $\frac{\lambda}{4}$, where $\lambda$ is measured at the center frequency in the operating frequency range [7]. Waves transmitted by antennas at the measurement points and scattered back by the target propagate as spherical waves with wavenumbers $k_1$ and $k_2$ as defined by the following equation:

$$k_1 = k_2 = k \tag{1}$$

where $k$ is the wave number for any wave propagating in any general direction. SAR images are then generated using the $\omega$-$k$ SAR algorithm as described in [7]. In this algorithm, the measured reflected signal $s_{(x,y,f)}$ is a function of the spatial dimention *x* and

*y* and the operating frequency *f* and is converted to a series of plane-waves propagating in the *z*-direction. This is acomplished using a Fourier transform to convert the signal from the spatial domain to the spectal domain. The waves are then backpropagated to the image location and then converted back to the spatial domain using inverse Fourier transforms to obtain the image $I_{(x,y,z)}$ as shown in (2):

$$I_{(x,y,z)} = IFFT_{k_x,k_y,k_z}\left(FFT_{x,y}\left(s_{(x,y,f)}\right)e^{j\sqrt{(2k)^2-k_x^2-k_y^2}\,z}\right) \tag{2}$$

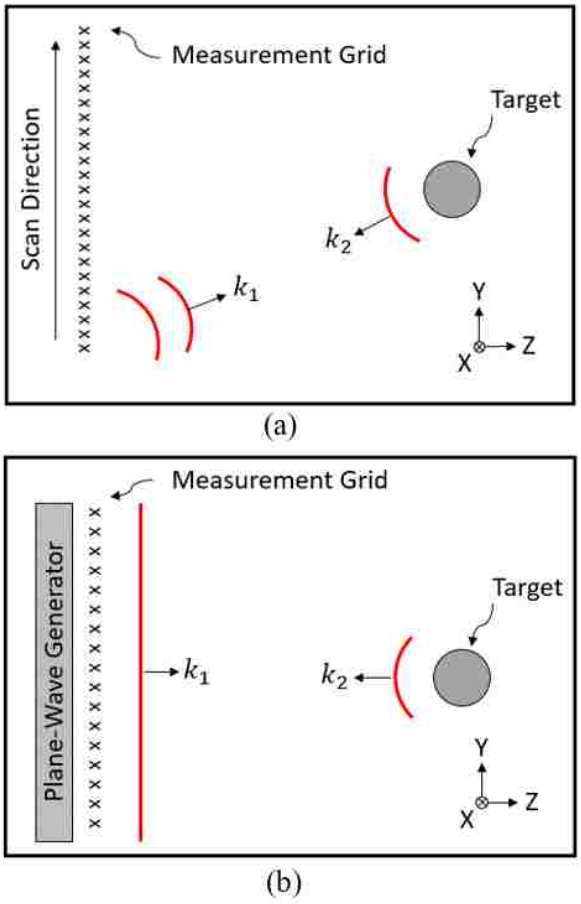


Figure 1. Imaging diagram for: (a) traditional mono-static *ω*-*k* SAR approach and (b) CESAR approach.

where $k_x$, $k_y$, and $k_z = \sqrt{(2k)^2 - k_x^2 - k_y^2}$ are wave numbers for plane-waves propagating in the *x*, *y*, and *z* directions respectivly.

The CESAR imaging methodology is shown in Figure 1(b). In this diagram, a plane-wave is propagated towards a target by a plane-wave generator. The reflected electric field travels back and is sampled at the measurement grid (preferably) collocated with the plane-wave generator. It is important to note that the received electric field can be measured *simultaneously* at each point on the measurement grid, which contrasts the sequential (switched transmitter-receiver) measurements of the previous approach. The measurement grid is then optimally spaced at $\frac{\lambda}{2}$, and the difference in spacing interval with the previous approach will be discussed later. Since the radiated electric field is a plane-wave propagating in the *z*-direction, it is also a single plane-wave in the spectral domain. Similar to the previous approach, the wave-number for the (spherical) reflected electric field correspond to a series of plane waves in the spectral domain through the Fourier transform relationship. The image reconstruction algorithm must therefore be modified accordingly as it is different than that shown in equation (4) and is given by:

$$I_{(x,y,z)} = IFFT_{k_x,k_y,k_z}\left(FFT_{x,y}\left(s_{(x,y,f)}\right)e^{j\left(k+\sqrt{k^2-k_x^2-k_y^2}\right)z}\right) \tag{3}$$

where $k_z = k + \sqrt{k^2 - k_x^2 - k_y^2}$. Equation (3), named the CESAR algorithm, is similar to the mono-static $\omega$-$k$ SAR, except the wave-number representing the radiated electric field is changed to represent a plane-wave. This is one of the benefits of using a plane-wave for target illumination such that it allows for implementing the mono-static $\omega$-$k$ SAR algorithm with minimal modifications.

## 1.2. IMAGE QUALITY COMPARISONS BETWEEN METHODOLOGIES

After the CESAR imaging methodology was developed, simulations were performed (in Python) to compare it to the mono-static $\omega$-$k$ SAR. Single frequency 2-D images of a point target were produced to compare how well each methodology performs in focusing on the point target. The first simulation involved traditional mono-static $\omega$-$k$ SAR [7], and the second simulation used CESAR. For both simulations, the measurement grid was $10\lambda$ x $10\lambda$ in size, and the point target was centered in front of the grid with a stand-off of $5\lambda$.

The results from these different imaging methodologies were compared using image spot width and spatial frequency bandwidth. Image spot width is the 3-dB spatial width of a point target in a SAR image [7]. Having a small spot width is beneficial for imaging targets that are close together and thus determines image spatial resolution. Similarly, spatial frequency bandwidth is the bandwidth of the raw imaging data. The spatial frequency bandwidth and spot width are inversely proportional to each other. Spot width and spatial frequency bandwidth were then calculated for each imaging methodology and are shown in Figure 2.

Comparing the results of the mono-static $\omega$-$k$ SAR to CESAR [Figure 2(a)] shows that the spatial frequency bandwidth of the former is twice that of the latter. This is expected, since the propagated electric field spreads twice the distance for the mono-static $\omega$-$k$ SAR case (measurement grid to target and target to measurement grid). The electric field spreads only from the target to the array in CESAR, since the radiated electric field is a plane-wave that does not spread as it travels to the target (i.e., a plane-wave has zero spatial frequency bandwidth). This is the reason why the electric field spatial sampling

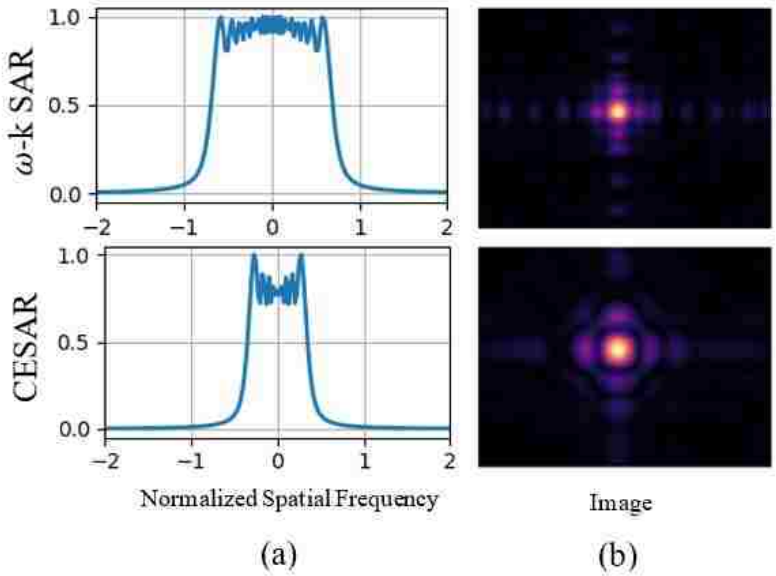


Figure 2. Comparison between mono-static ω-*k* SAR and CESAR: (a) measurement spatial frequency bandwidth, and (b) generated images focused on the point target.

interval is twice the size in the mono-static *ω-k* SAR. This allows for making the measurement grid more sparse (i.e., less number of antennas in a 2D imaging array), since the spatial frequency bandwidth is half that of mono-static *ω-k* SAR.

Due to the difference in the spatial frequency bandwidth, the spot width in the mono-static *ω-k* SAR case is half the width in the CESAR case, as also indicated in their SAR images in Figure 2(b). These comparisons show that when imaging with CESAR, one can expect to clearly detect the target in the SAR generated image, but with an image resolution that is coarser by a factor of two.

### 1.3. IMPLEMENTATION

In this section, the method for physically generating a plane-wave and measuring the reflected electric field from a target are discussed in the context of accomplishing both tasks in a compact and a less complex (in design) microwave camera. The first task,

generating a plane-wave in the near-field of the imaging system, is not trivial. One example of an ideal plane-wave generator would be a large aperture antenna (e.g., TEM horn) whose structure produces a TEM wave with uniform magnitude and phase. This kind of plane-wave generator is counter-intuitive to the goal of this investigation, which is to produce a compact microwave camera. In addition to the size of a large aperture antenna, it is also not possible to create a measurement grid at the aperture, and any hardware implemented some distance in front of the antenna would interfere with the plane-waves generated. Therefore, there must be a compromise between having an ideal plane-wave generator and having a compact microwave camera. This compromise can be achieved by using a planar antenna array whose elements have uniform magnitude and phase excitation, serving as the plane-wave generator. Planar antenna arrays with uniform magnitude and phase can be made compact using a network of passive power dividers [9]. Compared to previous imaging systems [4], there are no RF switches for feeding the array with this approach. Therefore, there is a significant reduction in RF hardware need and complexity for CESAR, which is its most important benefit.

A planar antenna array with uniform magnitude and phase excitation focuses the radiated electric field into a beam in the far-field. Additionally, in the near-field, the interference between array elements results in the production of a *pseudo* plane-wave, where *pseudo* refers to the fact that there are variations in the magnitude and phase of this wave relative to a proper plane-wave. For this type of SAR, imaging is conducted in the near-field of the imaging array. Therefore, a planar antenna array operating in its near-field meets the requirement for CESAR.

However, the gain in being compact and having no RF switches comes at the cost of a few limitations. First, the variations in its magnitude and phase distributions create low level distortions in the SAR generated image. For example, if a small target was placed in a region of space where the *pseudo* plane-wave's magnitude was high, the target would appear bright in the image. Similarly, moving the same target to a region where the magnitude was lower would result in the target appearing dimmer in the SAR image. For CESAR, there is a limit for how much of variations are acceptable, and they have been found through simulated imaging to be 8 dB and 40° for magnitude and phase, respectively. These limits were set for imaging point targets, and they can be changed depending on application requirements. Second, the beam-forming nature of the planar array has the effect such that the region where a *pseudo* plane-wave exists in front of the antenna array becomes smaller (with respect to the size of the antenna array) as the distance from the array increases. The region where a *pseudo* plane-wave exists is characterized by low level variations in magnitude and phase, typically no greater than the 8 dB and 40°, previously stated. The boundary of the *pseudo* plane-wave region is characterized by the phase changing significantly up to 180°, making it difficult to form images of targets outside of this boundary. Therefore, the usable imaging volume is reduced due to this beam-forming property.

To demonstrate these two limitations, the radiated electric field from a planar array of isotropic antennas was simulated (in Python). Figure 3 shows the simulation setup for the antenna array. The array consists of 64 isotropic elements in an 8 x 8 square configuration. The vertical and horizontal spacing between two adjacent antennas in the array is $\frac{\lambda}{2}$, where $\lambda$ represents the operating frequency, which is 24 GHz for these

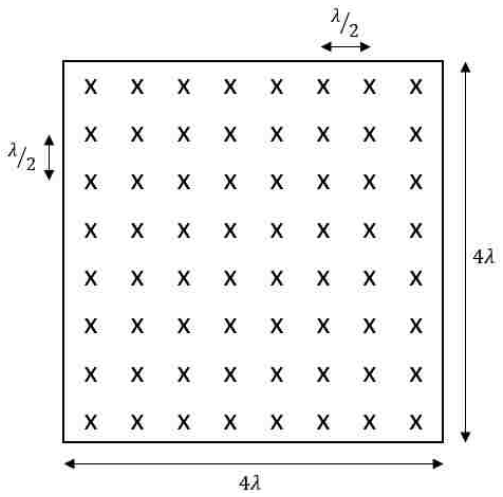


Figure 3. Diagram of 64-element planar array of isotropic antennas.

simulations. As a result, the size of the array was $4\lambda$ in each direction. A simulated electric field was radiated from all antennas to a measurement plane that was $2\lambda$ (half the width of the aperture) away from the array. This distance was chosen, since it is the optimal distance for focusing targets in aperture-limited SAR-generated images [7]. The simulated electric field was propagated using the free-space Green's function:

$$S_{(x,y)} = \sum_{m,n} \frac{1}{R_{(x,y,m,n)}} e^{-jkR_{(x,y,m,n)}} \tag{4}$$

where $m$ and $n$ are the row and column indices of the individual antennas, and $x$ and $y$ are the spatial coordinates on the measurement plane. The magnitude and phase distribution of the resulting composite electric field are shown in Figure 4(a-b), where Figure 4(a) shows the magnitude plotted in dB-scale, and Figure 4b shows the unwrapped electric field phase, respectively. The dashed lines show the physical extent of the antenna array. Within this region, a *pseudo* plane-wave exists with ~7-8 dB variation in magnitude and ~40° variation in phase. Beyond this region, the magnitude rolls off quickly down to -30 dB to -40 dB in some regions, and the phase changes by up to 180° compared to the *pseudo* plane-wave

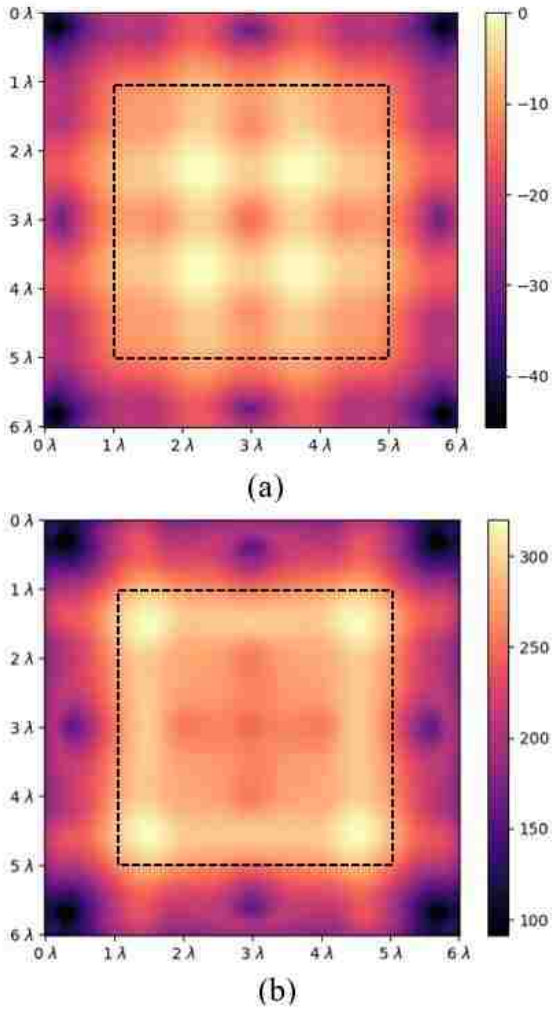


Figure 4. Simulated electric field radiated from a 64-element array of isotropic antennas. The dashed black line indicates the extents of the array: (a) log magnitude in dB-scale, and (b) unwrapped phase.

region. As mentioned earlier, these limitations create low-level image distortions and reduce image quality. However, while not implemented for this investigation, correction algorithms can be implemented to corrected for the low-level image distortions if increased computational time is tolerated.

The second task of physically implementing CESAR, which is how the reflected electric field is measured on a grid, was accomplished by placing Schottky diodes at the

antenna element apertures [1]. Using Schottky diodes is a hardware-efficient and compact method for creating the measurement grid. With this configuration, the Schottky diodes are automatically phase-referenced to the measurement grid created by the antenna array. For a given Schottky diode, it mixes the transmitted electric field from its antenna and a received signal due to all reflections from the environment, which is similar to [1] and [4]. However, since all antennas are radiating *simultaneously*, mutually coupled signals from other neighboring antennas are mixed in this Schottky diode as well. This interference lowers the SNR of the SAR generated image, which is another limitation of CESAR. The *chaotic* nature of the radiated electric field and interference between antennas is the motivation for naming this new imaging methodology Chaotic Excitation SAR.

There is a significant benefit of using Schottky diodes for measuring the reflected electric field. Since Schottky diodes output low-frequency baseband signals, they can be recorded by relatively low-cost and low-complexity analog-to-digital converters (ADCs). Furthermore, since all Schottky diodes on the antenna array measure the reflected electric field simultaneously, their baseband output signals can be measured by a bank of low-cost ADCs operating in parallel. In this configuration, the measurement speed can be increased by an order of magnitude, which is another major benefit of CESAR.

## 3. MICROWAVE CAMERA DESIGN

After the CESAR imaging methodology and image reconstruction algorithm was developed, a new microwave camera was designed and fabricated based on the implementation outlined in the previous section. For a microwave camera that uses a uniformly excited planar antenna array loaded with Schottky diodes for measurements, there are a few important design parameters that must be considered, namely: *i)* operating

frequency range, *ii)* antenna element spacing, *iii)* antenna radiation pattern, and *iv)* transmitter power.

First, the operating frequency range is determined by application requirements and the commercial availability of the state-of-the-art components and hardware. The center frequency of operation was chosen based on two reasons, namely: to comply with application requirements, and to demonstrate the fundamentals of the imaging approach. For NDT applications for example, 24 GHz has proven to be a suitable operating frequency [5], [10]. Additionally, there are many commercially-available Schottky diodes that work well at this frequency, which makes 24 GHz a suitable frequency for demonstration [11]. The operating frequency bandwidth determines range resolution and influences the resulting image SNR (i.e., higher the bandwidth, less noisy the resulting image) [7]. While a very fine range resolution was not crucial for this design, a bandwidth of 2 GHz was chosen to improve the low SNR inherent to CESAR imaging. Thus, the operating frequency range was chosen to be 23-25 GHz.

Next, antenna element spacing, which is another critical parameter, must be determined for three reasons. First, the antenna element spacing sets the electric field spatial sampling, since Schottky diodes are placed on the antenna elements [1]. A spacing of one- half wavelength ($\frac{\lambda}{2}$) is sufficient to generate SAR images without aliasing-caused distortions [7]. Increasing the element spacing to one wavelength ($\lambda$) can create significant aliasing in the resulting SAR images. Therefore, designing the element spacing to be as small as possible is ideal.

The second reason why element spacing is critical is that *pseudo* plane-wave purity (i.e., how close a *pseudo* plane-wave is to an ideal plane-wave) is dependent on element

spacing. Large element spacing produces deep nulls in the magnitude of the radiated electric field distribution in the near-field of the antenna array. Consequently, as the element spacing decreases, the antenna array becomes similar to a continuous source (i.e., TEM horn antenna) with a near-field radiated electric field closely resembling a plane-wave. The influence of element spacing on *pseudo* plane-wave purity is similar to the influence element spacing has on the far-field pattern. An element spacing of $\frac{\lambda}{2}$ or smaller produces minimal side lobes. A spacing between $\frac{\lambda}{2}$ and $\lambda$ produces significant side lobes. Finally, a spacing of $\lambda$ or greater produces grating lobes [12]. In summary, as element spacing decreases, the *pseudo* plane-wave becomes closer to an ideal plane-wave resulting in a reduction of the low-level image distortions inherent to CESAR. The final reason why element spacing is critical is that it limits the physical antenna size. In a compact array, the antenna width sets the minimum element spacing. Therefore, the antenna must be designed to be small enough to achieve the desired element spacing for SAR imaging requirements.

The array antenna element radiation pattern is also critical for two reasons. First, the antenna element must have a relatively directional radiation pattern while also having a sufficiently wide main lobe to utilize the focusing benefits of SAR [7], [13]. Second, such a radiation pattern also benefits *pseudo* plane-wave purity. As mentioned in Section 2, a simultaneously radiating antenna array with uniform magnitude and phase has inter-element interference in the near-field of the array resulting in variations in the magnitude and phase of the plane-wave. Having a directive antenna can potentially reduce the inter-element interactions and contribute to a more uniform electric field distribution directly in front of the array. Therefore, to reach a compromise between the SAR requirement and

*pseudo* plane-wave purity, a relatively directive antenna should be chosen with a moderately wide beamwidth.

Finally, transmitter power is a parameter unique to microwave camera designs that employ Schottky diodes as their receivers [4]. Stated previously, Schottky diodes mix the transmitted electric field and the reflected signal from the target. The combined power of both signals determines the output baseband voltage [11]. Additionally, Schottky diodes have a noise floor, where under a certain level, RF signals cannot be measured. Thus, each antenna has a minimum input power required for transmission, so the corresponding Schottky diode is properly biased and produces an output baseband voltage that is sufficiently higher than its noise floor. Additionally, increasing input power increases output baseband voltage SNR, but the input power should be limited to not saturate the Schottky diode.

Based on these design parameters, the new camera was designed, with its basic schematic shown in Figure 5. The major components of the camera are the microwave source (transmitter), the data acquisition hardware, the passive power divider network, and the planar array of 64 aperture antennas loaded with Schottky diodes. The camera operates by tuning the microwave source to a single frequency, where the generated signal is then radiated from all antennas. The radiated electric field and reflected field from a target are mixed together at the Schottky diodes (at the antenna apertures), and the baseband outputs of the Schottky diodes are multiplexed to an ADC for recording. The Schottky diode voltages were multiplexed instead of measured in parallel to reduce camera hardware. These steps are repeated for 21 frequency points in the 23-25 GHz operating range, and the raw imaging data is then processed on a PC to generate a 2-D image of a target. Having a

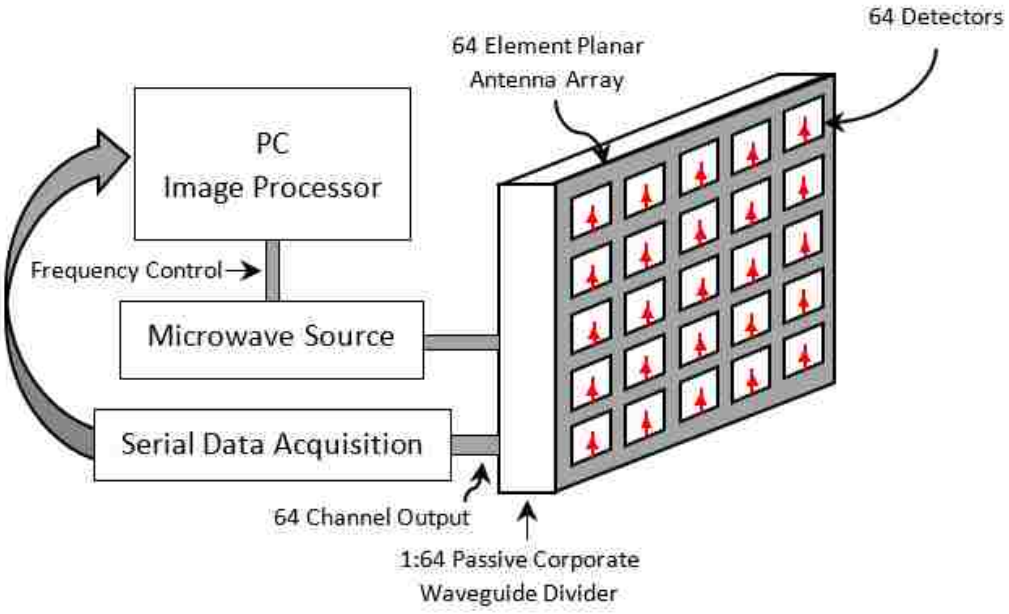


Figure 5. Basic diagram of the designed microwave camera.

high number of frequency points increases the SNR in SAR generated images. However, a high number of frequency points increases measurement time. Therefore, 21 points were chosen as a compromise between SNR and measurement time.

While a portion of the hardware including the microwave source and data acquisition hardware was designed and fabricated with commercially-available components, most of the camera design work had to do with the antenna array and passive power divider network designs. After investigating several potential suitable antenna and antenna array designs, a corporate waveguide-fed slot array was chosen [9]. This structure, which was originally designed for millimeter wave communications applications, has several features that are attractive for this camera design. First, a corporate feed waveguide network is a low-loss power divider network that is compact and can be designed to feed the antenna elements with a relatively uniform magnitude and phase. Second, the implementation of a unit cell of four slot antennas allows for reduced complexity in the

waveguide divider network and provides for reduced antenna element spacing. For example, if each terminating point of the waveguide network fed into a single antenna, the network would be divided into 64 outputs. By implementing a *unit cell* of four slot antennas, the division ratio becomes 1:16 for the waveguide network and 1:4 for the unit cell, thus enabling a compact 1:64 power divider network. Finally, rectangular slot antennas are moderately directive (compared to an isotropic antenna), and slot antennas are not only suitable for SAR imaging purposes, they provide for relatively easy loading of the Schottky diodes at their apertures [5], [10].

The design of the antenna array and power divider network is similar to the structure described in [9]. However, there were two major changes to the design, namely: array optimization for 24 GHz operation, and addition of Schottky diode-loaded monopoles, at their apertures, for electric field sampling (i.e., Schottky diode placement). The design began with the unit cell, which is shown in Figure 6. The unit cell is composed of a coupling aperture, a cavity, and a 2x2 rectangular slot array, are all shown in the stack-up in Figure 6(a). The three components of the unit cell were simulated together, since the reflection coefficient and radiation response of the rectangular slots are dependent on the cavity and the coupling aperture. Electric field propagation begins with injecting a $TE_{10}$ mode into the coupling aperture. The $TE_{10}$ mode sets up a circulating magnetic field that flows around the cavity. Due to the placement of the slots, the circulating magnetic field produces quasi $TE_{10}$ modes on the rectangular slots, where electric fields are then radiated. The unit cell effectively splits the input signal into four channels and then radiates the divided signals with the same magnitude and phase.

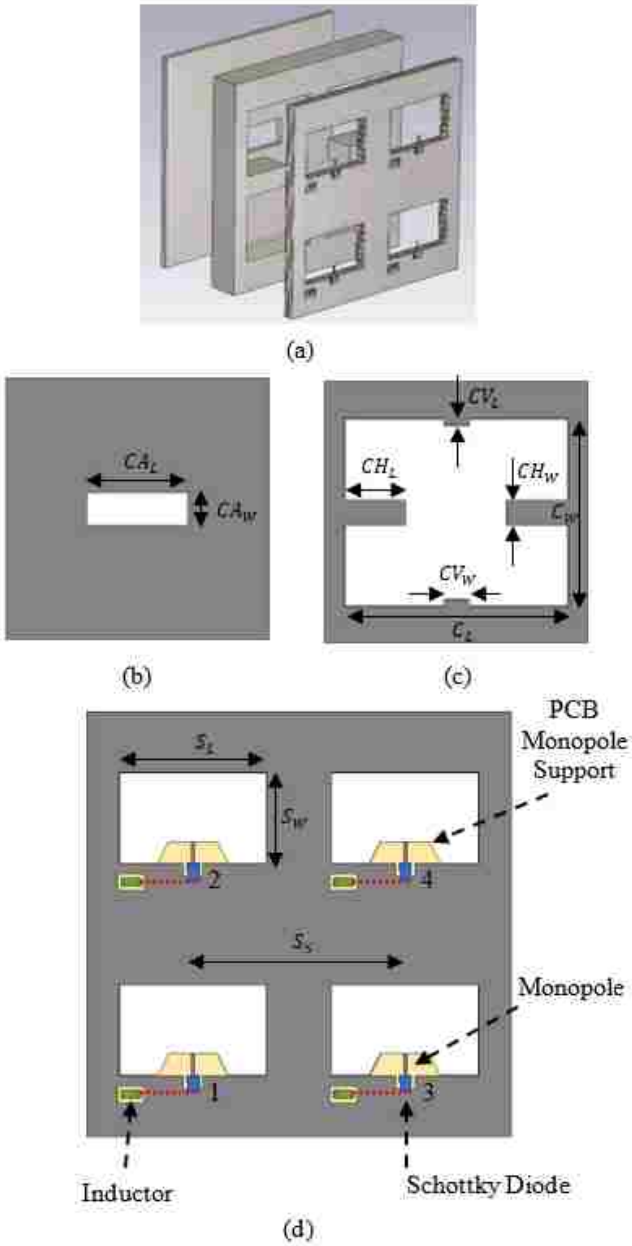


Figure 6. (a) Unit cell stack-up, (b) Coupling aperture ($CA_L$= 7.50 mm, $CA_W$ = 2.40 $mm$), (c) Cavity ($CV_L$ = 0.50 mm, $CV_W$ = 1.90 mm, $CH_L$ = 4.55 mm, $CH_W$ = 1.90 mm, $C_L$ = 16.6 mm, $C_W$ = 14.0 mm), and (d) 4-layer PCB with slots ($S_L$ = 6.80 mm, $S_W$ = 4.20 mm, $S_S$ = 9.80 mm). Red dashed lines indicate internal PCB routing.

To achieve an operating frequency range of 23-25 GHz, the coupling slot dimensions and the cavity perimeter were optimized and are shown in Figure 6(b) and Figure 6(c), respectively. Figure 6(d) shows the rectangular slots. The slots for the new

camera were designed on a 4-layer printed circuit board (PCB), so the Schottky diodes could be placed at the lower edges of the slots to be simultaneously exposed to the transmitted and received electric fields. Rectangular slots were first cut out of the PCB, and their dimensions were optimized for radiating in the 23-25 GHz frequency range. Vias were placed around the slots, so the electric fields would not leak into the internal layers of the PCB. Next, a monopole supported by a small trapezoidal-shaped extension of the PCB substrate was simulated within the slot as shown in Figure 6(d). For each portion of the exposed substrate, a monopole antenna (1.00 mm x 0.127 mm) was placed in the center of the exposed substrate, where the terminal of the monopole was loaded with an SMS7621-060 Schottky diode [11]. The anode port of the detector was grounded to the PCB, and the cathode port was routed away from the slot using a blind via and routing on the internal layers of the PCB. For each Schottky diode, the signal line was routed to a 270 nH inductor to function as an RF choke. Finally, the signal was routed away from the inductor and into the data acquisition hardware. The final center-to-center antenna spacing for the rectangular slots was 9.80 mm, which is approximately $0.78\lambda$ at 24 GHz. While this is larger than the optimal electric field spatial sampling of $\frac{\lambda}{2}$, it is still less than $\lambda$. Thus, images made with this camera are expected to have some aliasing-caused distortions, but the distortions are not expected to be so significant to completely mask targets.

Figure 7 shows the reflection coefficient response of the unit cell. The -10 dB bandwidth ranges from 22.4 GHz to 24.6 GHz. It is shown later that this response shifts a bit higher in frequency when fed by the corporate feed waveguide network. The resonant response of the unit cell is due to the combined resonance features of the cavity and rectangular slots. Next, the RF voltage at each Schottky diode was simulated. Figure 8

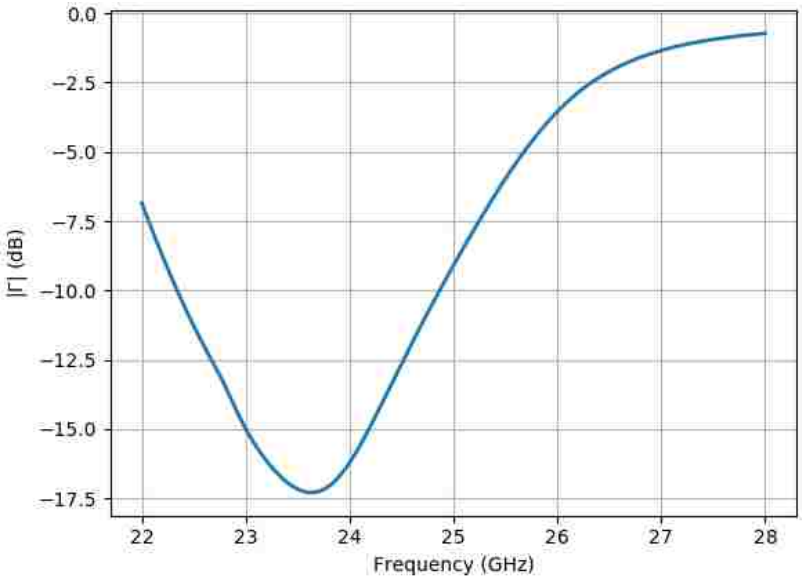


Figure 7. Unit cell simulated reflection coefficient.

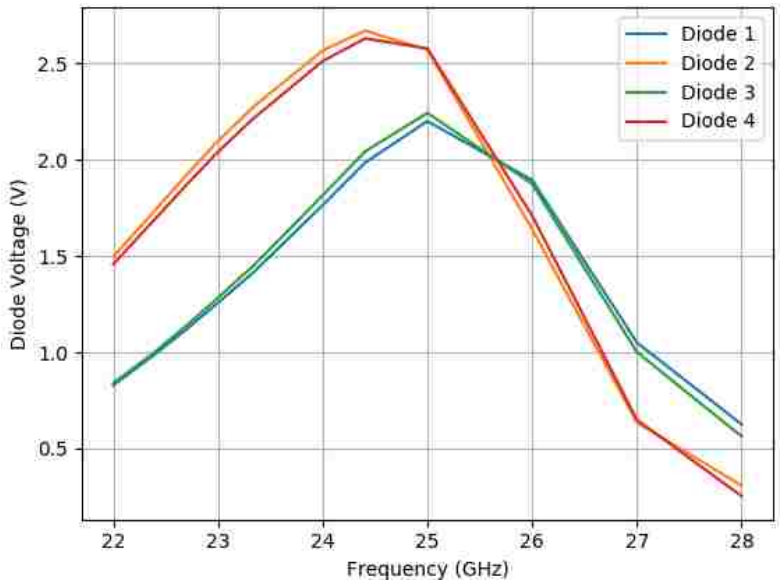


Figure 8. Simulated voltage response of each Schottky diode in unit cell.

shows all voltages at the terminals of the Schottky diodes resulting from electric fields radiating from the slots. For the 23-25 GHz frequency range, the Schottky diode voltages vary from 1.3 V to 2.6 V. These voltages are referenced to 27 dBm input power at the coupling aperture, which is the default parameter value in CST. In practice, these voltages will be lower depending on the output power level of the transmitter. The difference in

voltage between Schottky diodes 1, 3 and 2, 4 is due to two of the Schottky diodes being located over the center of the cavity, where the field strength is higher. These differing voltages will be equalized (calibrated) before imaging tests are conducted. Regardless of the difference in values, these responses show that the Schottky diodes are sufficiently sensitive to electric fields at the rectangular slots for microwave imaging measurements.

With the unit cell optimized and simulated for operating in the ~23-25 GHz frequency range, it was arranged into a 64 x 64 slot array with a 1:16 corporate feed waveguide network feeding the coupling apertures of the unit cells. Diagrams of the waveguide network and full array are shown in Figure 9. In Figure 9(a), the waveguide network is fed by an SMA feed (not shown), which was designed similar to traditional right-angle coaxial-to-waveguide adapters. The input signal is divided equally in minimize unwanted reflections and tune the H-plane tees for the ~23-25 GHz operating frequency band. For all portions of the network, the waveguide dimensions are 7.51 mm and 2.90 mm in their broad and narrow dimensions, respectively. The unit cells are aligned over the waveguide network as indicated by the red dashed lines [representing the coupling apertures in Figure 9(b)]. Slots are then cut in the waveguide terminations to create the coupling apertures for generating the $TE_{10}$ modes required for the unit cells. One important detail to mention is that going from top to bottom in Figure 9(a), the broad and narrow dimensions of the waveguides, where coupling apertures are made, are alternated. This is illustrated in the red dashed lines. Depending on which side the coupling aperture is cut, the $TE_{10}$ mode will have either a 0° or 180° phase. The placement scheme ensures that all unit cells are fed with the same phase.

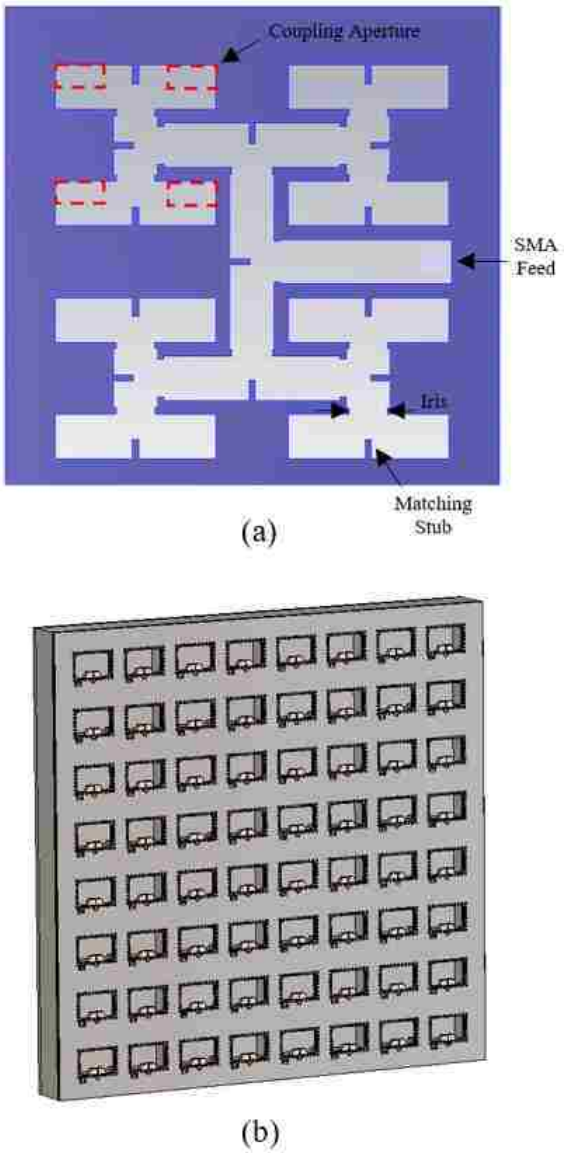


Figure 9. (a) Corporate feed waveguide network, and (b) the full imaging array.

Figure 9(b) shows the full array of 64 rectangular slot antennas. The full array was simulated for its composite reflection coefficient and radiated electric field to determine its suitability for microwave imaging in the 23-25 GHz frequency range, using the CESAR approach. Figure 10 shows the reflection coefficient response for the full array with and without the input SMA-to-waveguide transition/adapter. For the response without the transition, the -10 dB bandwidth is ~23-25 GHz, where the response follows the same trend

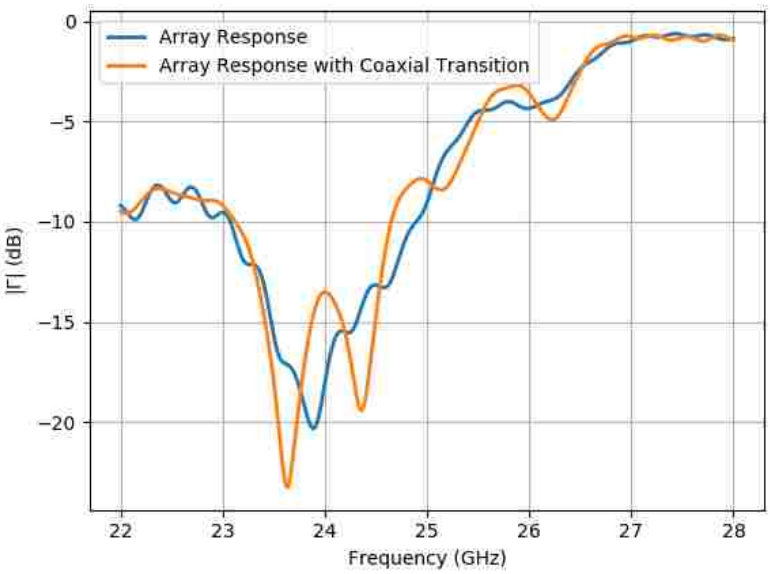


Figure 10. Reflection coefficient response for simulated full array.

as that of the unit cell. However, for the response with the coaxial transition, the -10 dB bandwidth reduces by ~300 MHz. While this is slightly lower than the intended bandwidth, the reflection coefficient is below -8 dB for the frequency range of 23-25 GHz. For this camera, the power radiated from each slot is critical. This is due to the fact that Schottky diodes require a minimum level of RF power (for proper biasing) to generate baseband signals with appreciable SNR. Therefore, since most of the power is radiated from the antenna array, a reflection coefficient slightly higher than -10 dB can be tolerated. It is shown in a later section that this slight degradation does not negatively affect image quality when imaging with the full 23-25 GHz band.

Figure 11 shows the simulated spatial distribution of the radiated electric field (magnitude and phase) from the full array, calculated at a distance of 40 mm from the array, corresponding to half of the entire array width [7]. For both plots, the electric field within the extents of the array, indicated by the dashed lines, resembles a *pseudo* plane-wave, as

expected. The electric field intensity is more uniform than that shown in Figure 4(a), since the antenna element is a rectangular slot [as opposed to a point source in Figure 4(a)] and is more directive. However, at the edges of the array, the magnitude falls -10 to -20 dB. This is due to the radiated electric field beginning to focus into a beam. Additionally, the phase distribution is more uniform in comparison to Figure 4(b), where the phase varies by

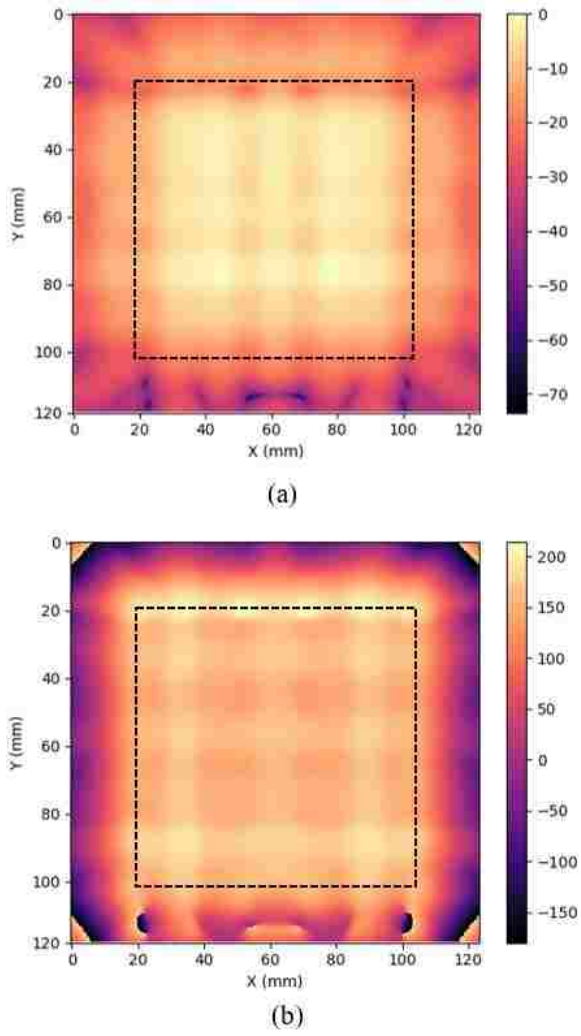


Figure 11. Simulated electric field radiated from the 64-element array rectangular slot array. The dotted black line indicates the extents of the array: (a) log magnitude in dB-scale, and (b) unwrapped phase.

30° for most of the region over the array. These results indicate that this antenna array can sufficiently generate *pseudo* plane-waves for CESAR imaging.

## 4. MICROWAVE CAMERA FABRICATION

The new microwave camera was fabricated in a few steps. The first step was the assembly of the antenna array. A diagram of the assembly is shown in Figure 12. The

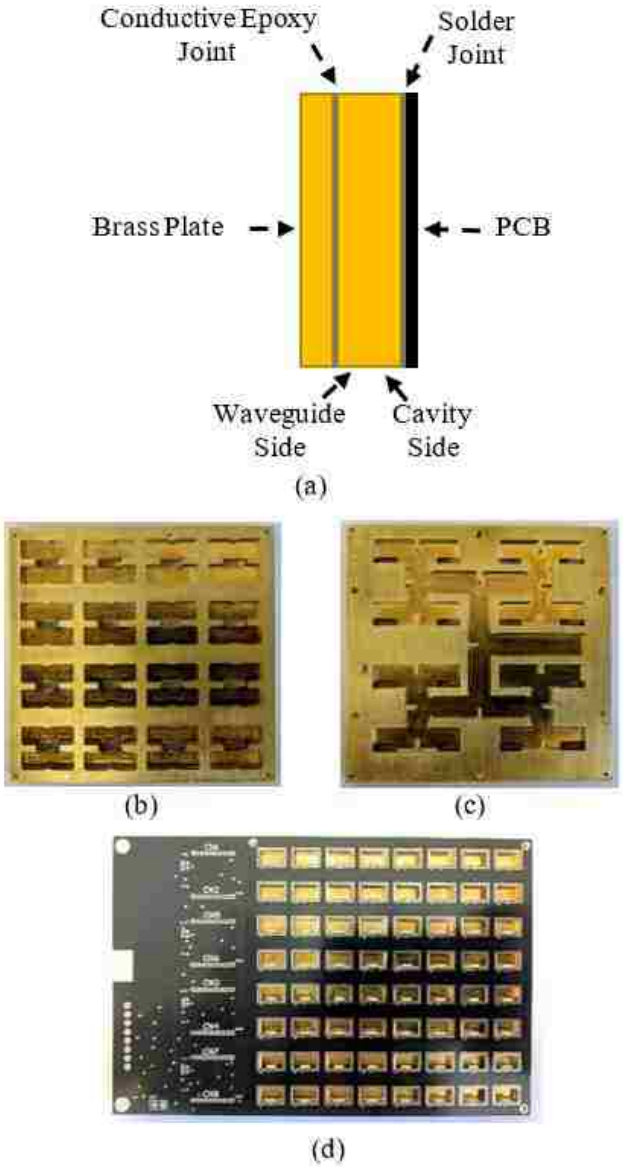


Figure 12. Antenna array fabrication: (a) assembly diagram, (b) cavity side of brass block, (c) waveguide side of brass plate, and (d) assembled array.

antenna array and corporate feed waveguide network were assembled in three parts. The first part is the 4-layer PCB with rectangular slots cut out. The second part is a brass block with one side having the cavities, and the other side having the waveguide network machined in. Both sides are connected by the coupling apertures. Finally, there is a brass plate with a mounting point for the SMA feed. Figure 12(a) shows how the parts assemble together. The PCB was first soldered to the cavity side of the brass block [shown in Figure 12(b)] with a reflow oven. Next, the waveguide side of the brass block [shown in Figure 12(c)] was capped with the brass plate and conductive epoxy. The assembled antenna array is shown in Figure 12(d). The portion of the PCB that extends over the left side of the array houses the multiplexing circuitry for routing the Schottky diode voltages to a single output. This circuitry is composed of five ADG1607 8-channel dual-multiplexers and is located on the back-side of the PCB (not shown) [14]. The assembled array is approximately 120 mm x 80 mm x 9.52 mm in size.

After assembly, the reflection coefficient at the SMA input of the array was measured with an Anritsu Vector Star MS4644A Vector Network Analyzer (VNA) with the array radiating into free-space. Figure 13 shows the measured reflection coefficient. For the 23-25 GHz frequency range of interest, the reflection coefficient is below -10 dB. There is additional loss that can be attributed to the fact that the conductive epoxy and the solder holding the array together do not completely prevent signals from leaking between the PCB, brass block, and brass plate.

Next, the spatial distribution of the radiated electric field from the antenna array was measured. This was accomplished by scanning the radiated electric field with a K-band (18-26.5 GHz) waveguide 100 mm above the array. The distance was chosen so that

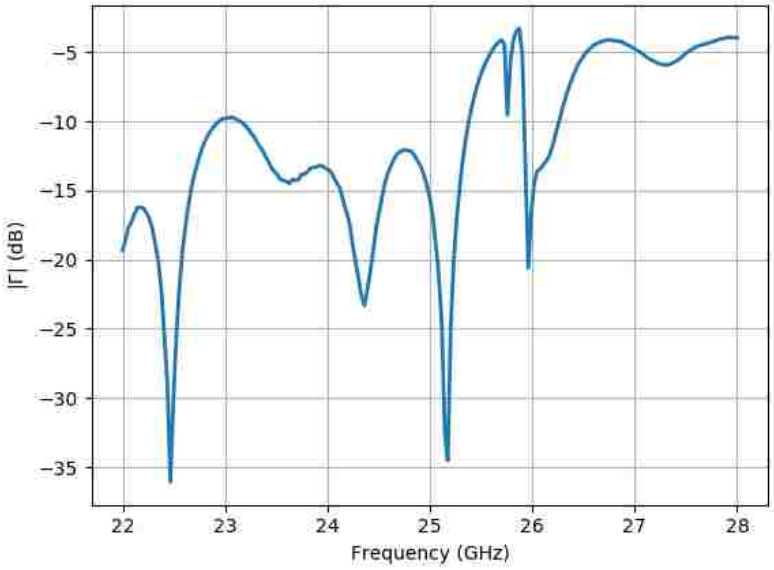


Figure 13. Measured reflection coefficient of the fabricated antenna array while radiating into free-space.

the influence of multiple reflections between the probing waveguide and the array would be minimized. Port 1 of the Anritsu VNA was connected to the antenna array, and port 2 was connected to the K-band waveguide suspended above the array. Next, an area of 120 mm x 120 mm above the array was scanned. Finally, the *ω-k* SAR algorithm was applied to the scan data to back-propagate the measurements to a location 40 mm above the antenna array [7]. The algorithm applied a one-way back-propagation, which effectively produced a radiated electric field image 40 mm away from the array. These results are shown in Figure 14. The electric field intensity plot shows a smooth *pseudo* plane-wave over the spatial extent of the array, where there are some variations in the field intensity in the middle and at the edges. The phase distribution results show a similar trend with some variations in the middle. Within the dashed lines, magnitude and phase vary by ~7 dB and ~35°, respectively.

The transmitter was fabricated next, as shown in Figure 15(a). It was composed of an HMC739 VCO and an HMC863 power amplifier [15]-[16]. A free-running VCO was chosen to supply the microwave signal without a phase-locked-loop, since a prior study has shown that the slight frequency drift in these VCOs does not contribute to visible distortions in SAR generated images [17]. The VCO output frequency is tuned by an analog voltage, where an input voltage range of 0.8-2.8 V produces and output frequency range of

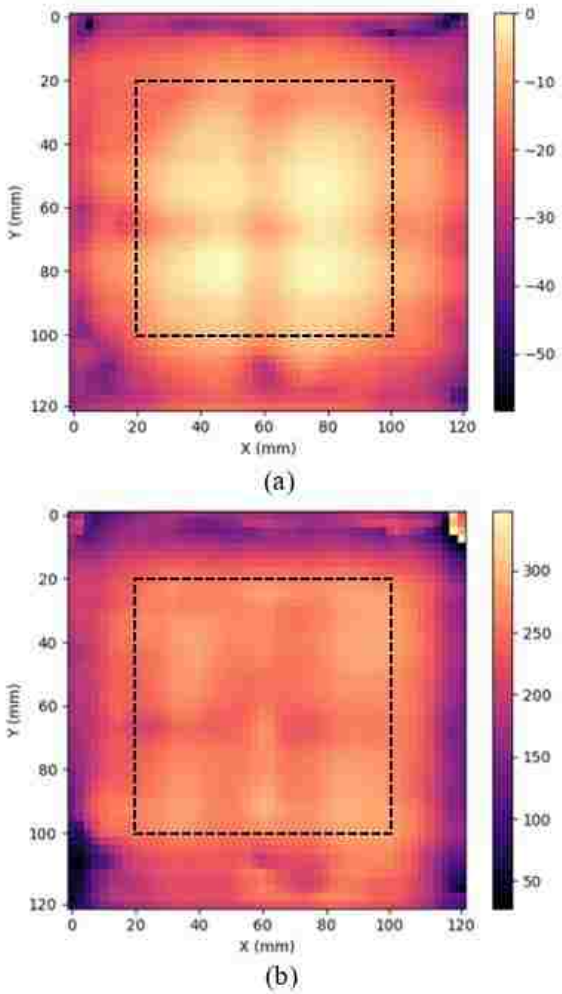


Figure 14. Measured electric field radiated from the fabricated antenna array. The dotted black line indicates the spatial extents of the array: (a) log magnitude in dB-scale, and (b) unwrapped phase.

23-25 GHz. The power amplifier produces 24 dBm to be fed into the array. This level was required to produce Schottky diode output voltages on the order of 10s of millivolts, for proper biasing [11].

With the transmitter fabricated, all components were placed in a 3D printed enclosure, where the complete camera is shown in Figure 15(b). The camera antenna array dimension is 78 mm x 75 mm, and the depth of the enclosure is 55 mm (the overall package as shown in Figure 15b is ~140 mm x 89 mm x 55 mm). The transmitter, antenna array, Schottky diode voltage multiplexer circuitry, and a power regulator board are housed within the enclosure. A small fan was installed in the side of the camera enclosure to

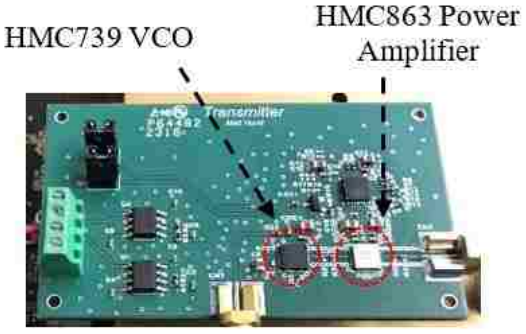


(a)

(b)

Figure 15. (a) Transmitter PCB, and (b) the assembled camera.

remove heat from the transmitter board. On the left side of the camera, there are two connectors. The multiplexed Schottky diode output voltage is terminated in an SMA connector which is then connected to an ADC. The analog tuning voltage for the VCO, digital lines for controlling the Schottky diode voltage multiplexers, and power lines are terminated in a rectangular terminal block. This camera is controlled by National Instruments Data Acquisition (NI-DAQ®) hardware, and the connectors are used for interfacing with the NI-DAQ hardware for tuning the frequency, controlling the multiplexers and measuring the voltages from the Schottky diodes. Future versions of this camera can be made with an on-board microprocessor, which would eliminate having the camera tethered to NI-DAQ hardware.

Before the camera could be used to make microwave images, voltage equalization (i.e., calibration) was applied to all Schottky diode outputs. As mentioned in Section 3, the output voltages from the Schottky diodes can vary depending on location within a unit cell and the individual solid-state characteristics of the Schottky diode. Additionally, soldering the Schottky diodes to the PCB can slightly affect their output voltages. For these reasons, the voltages from all Schottky diodes had to be equalized (calibrated out variations in Schottky diode voltage) before imaging.

One procedure that has been used previously for equalizing Schottky diode voltages has been to position a metal plate close to the array and measure voltages from the Schottky diodes when the array is radiating towards the plate. The distance between the array and plate is then varied, and the magnitude of the sinusoidal voltage response for each Schottky diode (when only one antenna transmits and receives) with respect to distance is measured and used for equalization [18]. This magnitude of the sinusoidal responses (due to varying

distance along a standing wave) is then an indication of Schottky diode sensitivity when mixing the transmitted and the received signals. For this camera, the same approach cannot be used since, unlike the previous mono-static system where each antenna transmits and receives independently, all antenna elements are *simultaneously* radiating. There are complex interactions (e.g., multiple reflections, element-to-element interference, etc.) that not only create differences in voltages between Schottky diodes in the array, but also distort the Schottky diode voltage response with respect to distance between array and metal plate. This behavior is due to the metal plate being in the near-field of the array resulting in bi-static interference between each two array elements. Ideally, the reflected electric field from the metal plate should be a plane-wave, so all Schottky diodes receive the same magnitude and phase, independent of distance to the reflector, for equalization. This was accomplished by performing a similar calibration experiment, except the metal plate was positioned in the far-field of the array where bi-static measurement is approximated with a quasi-monostatic model.

A picture of the Schottky diode voltage equalization (calibration) setup is shown in Figure 16. Absorbing foam was placed around the setup and on the floor to minimize unwanted reflections in the measurement environment. The traditional far-field distance of $\frac{2D^2}{\lambda}$ is ~983 mm for this array, which was too great of a distance for this experiment. Therefore, for this setup, the camera was held 520 mm away from the metal plate (which was 300 mm x 300 mm in size). This distance was calculated based on a rule-of-thumb that if the angle ($\theta_t$) between farthest transmitting antennas (worst quasi-monostatic approximation) with respect to a metal plate is equal to or less than 10° (actual angle was calculated to be 8.2°). This ensures that the distance of the array to the metallic plate is

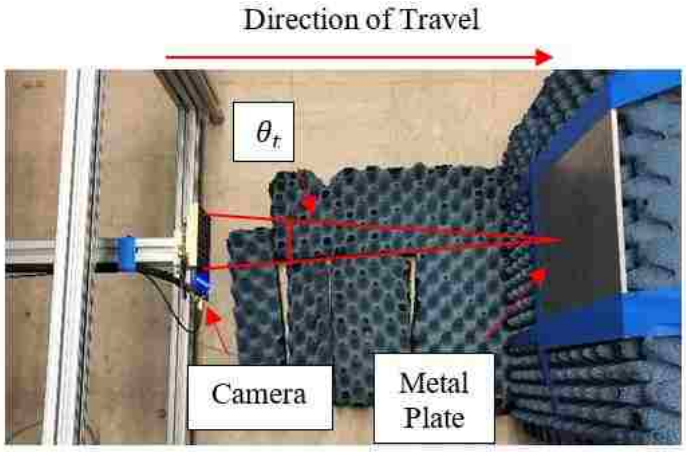


Figure 16. Measurement setup for Schottky diode voltage equalization (calibration) experiment.

more than 99% of the bi-static roundtrip path. Next, the camera transmitted an electric field towards the metal plate, and the transmitted and reflected electric fields were mixed at all Schottky diode locations and recorded. This process was completed for 21 frequency points in the 23-25 GHz frequency range. After all frequencies were transmitted, the camera was moved 1 mm closer to the metal plate. This procedure was repeated until the camera was 480 mm from the metal plate. This travel distance approximately corresponds to 3 wavelengths, which provides a good estimate of diode response. Figure 17 shows the voltage from one Schottky diode at 24 GHz. In this figure, the voltage is sinusoidal with respect to distance, as expected. The magnitude is also constant across the measurement distance, which is due to the experiment being conducted in the far-field of the array, unlike the experiment in [18]. Thus, a Schottky diode voltage equalization matrix was formed from the magnitudes of these sinusoids (after DC level subtraction) across all Schottky diodes and frequencies. Here, the DC level corresponds to the bias level of the Schottky diode and also includes the constant aperture reflection at the slots. Raw imaging data was then divided element-wise by the equalization matrix before images were produced.

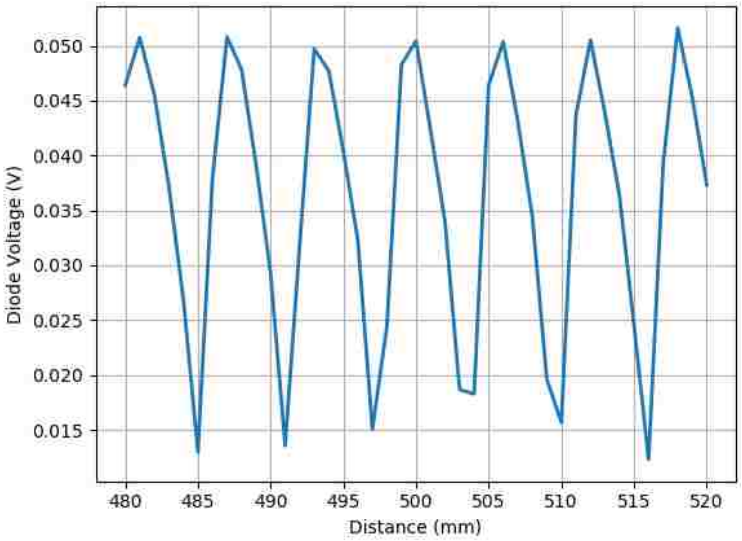


Figure 17. Measured voltage from one Schottky diode at 24 GHz from the Schottky diode voltage equalization experiment.

## 5. IMAGING RESULTS

Two basic targets were imaged to demonstrate the new camera's capabilities. The first imaging example was a manufactured defect in a dielectric material to demonstrate the camera's sensitivity to dielectric contrast. A defect was printed into a small polylactic acid (PLA) plate, which has a relative dielectric constant of ~3. The defect was a 10 mm-diameter and 2 mm-deep circular flat-bottom hole. This defect was filled with a small and thin piece of rubber, with a relative dielectric constant of ~9 placed in the hole, as shown in Figure 18. The PLA block was placed on a 40 mm-thick piece of construction foam. Foam was used, since it has similar dielectric constant to air at 24 GHz. Figure 18(b) shows the raw imaging data at 24 GHz, where the rubber cannot be seen due to the defocusing property of electromagnetic propagation. Using the CESAR algorithm, an image slice, at the location of the rubber piece, was produced, as shown in Figure 18(c). In this image, the dielectric contrast between rubber and PLA is clearly indicated as the bright spot, and the

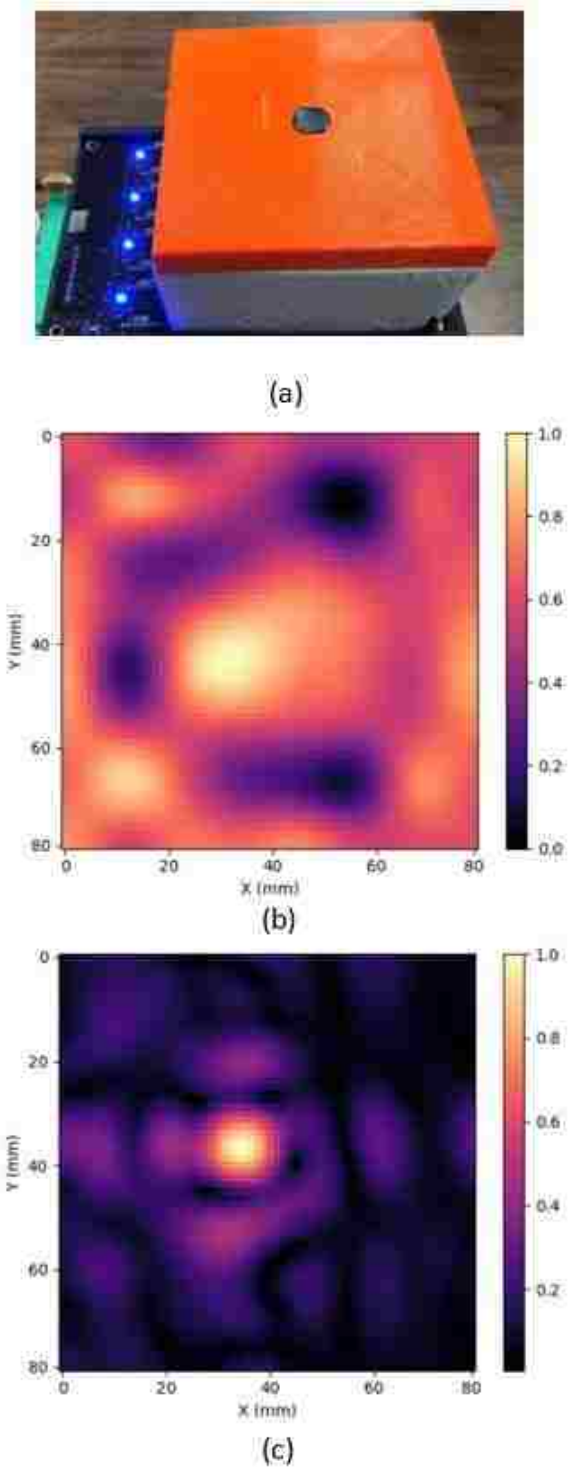


Figure 18. Imaging a rubber defect in PLA: (a) measurement setup, (b) raw imaging data at 24 GHz and (c) resulting image slice at the rubber location (depth).

indication of the rubber has the same basic shape and size compared to the actual piece of rubber. The features around the bright spot that resemble sidelobes of a two-dimensional sinc function result from the $0.78\lambda$ of sample spacing (i.e., 2D aliasing feature), as expected and explained earlier. Additionally, the low-level image distortions in the background are caused by the plane-wave approximation in the CESAR algorithm. This approximation can be removed in future versions of the CESAR algorithm by adding compensation for the magnitude and phase of the propagated *pseudo* plane-wave. Additionally, improvements can be made to account for multi-layered structures [19]. This would account for electric field propagation within the PLA structure and better focus the image of the rubber flaw. However, this imaging experiment clearly shows the camera's sensitivity to dielectric contrast as well as CESAR's ability to focus to the location and size of a flaw.

The second imaging example was a metal key to demonstrate the camera's ability to locate and reconstruct the basic shape of metal targets for security applications. Figure 19(a) shows the metal key placed over the camera, Figure 19(b) shows the raw imaging data at 24 GHz, and Figure 19(c) shows the resulting image. Here, the shape and orientation of the key is clear, indicating the focusing benefit of CESAR. The bright spot under the plastic part of the key is due to the presence of a metal plate contained within the plastic. This imaging experiment shows how the camera can be employed to identify the location and shape of a metallic target.

## 6. CONCLUSION

A new SAR-based microwave imaging methodology, defined as CESAR, was developed specifically for implementation in a microwave camera with significantly less

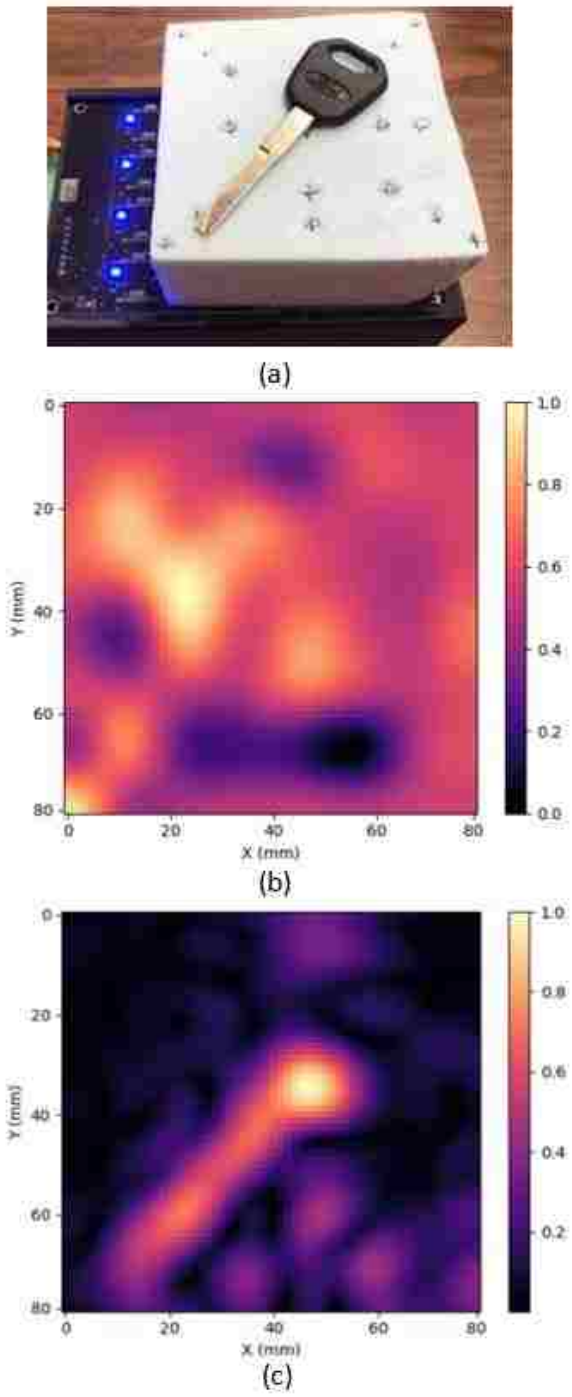


Figure 19. (a) Picture of a metal key placed in front of the imaging system aperture, (b) raw imaging data at 24 GHz, and (c) resulting image.

hardware in comparison to previous cameras. The methodology is based on *simultaneously* radiating from all antennas in an array instead of sequential radiation. As a result, the

propagated electric field from the array to the target is a *pseudo* plane-wave, which was approximated as a plane-wave in the CESAR algorithm for image reconstruction. A compact microwave camera was designed and fabricated based on CESAR. The design of the antenna array and passive power divider network in the camera were based on a corporate waveguide-fed rectangular slot array. Simulations and experimental results demonstrated the camera's ability to generate a *pseudo* plane-wave for CESAR imaging. Imaging results showed the camera's ability to locate dielectric contrast and metallic objects for NDT and security applications. Future iterations of the CESAR algorithm include compensation for the plane-wave approximation and electric field propagation modeling for multi-layered structures. Future investigations will also involve continued hardware reduction in addition to increasing frequency for expanding towards millimeter wave imaging applications.

## REFERENCES

[1] M. T. Ghasr, J. T. Case, and R. Zoughi, "Novel Reflectometer for Millimeter-Wave 3-D Holographic Imaging," *IEEE Transactions on Instrumentation and Measurement,* vol. 63, pp. 1328-1336, 2014.

[2] Y. Gao and R. Zoughi, "Millimeter Wave Reflectometry and Imaging for Noninvasive Diagnosis of Skin Burn Injuries," *IEEE Transactions on Instrumentation and Measurement,* vol. 66, pp. 77-84, 2017.

[3] D. M. Sheen, D. L. McMakin, and T. E. Hall, "Three-dimensional millimeter-wave imaging for concealed weapon detection," *IEEE Transactions on Microwave Theory and Techniques,* vol. 49, pp. 1581-1592, 2001.

[4] M. T. Ghasr, M. J. Horst, M. R. Dvorsky, and R. Zoughi, "Wideband Microwave Camera for Real-Time 3-D Imaging," *IEEE Transactions on Antennas and Propagation,* vol. 65, pp. 258-268, 2017.

[5] M. T. Ghasr, M. A. Abou-Khousa, S. Kharkovsky, R. Zoughi, and D. Pommerenke, "Portable Real-Time Microwave Camera at 24 GHz," *IEEE Transactions on Antennas and Propagation,* vol. 60, pp. 1114-1125, 2012.

[6] M. T. Ghasr, S. Kharkovsky, R. Bohnert, B. Hirst, and R. Zoughi, "30 GHz Linear High-Resolution and Rapid Millimeter Wave Imaging System for NDE," *IEEE Transactions on Antennas and Propagation,* vol. 61, pp. 4733-4740, 2013.

[7] J. T. Case, M. T. Ghasr, and R. Zoughi, "Optimum Two-Dimensional Uniform Spatial Sampling for Microwave SAR-Based NDE Imaging Systems," *IEEE Transactions on Instrumentation and Measurement,* vol. 60, pp. 3806-3815, 2011.

[8] M. Pastorino, *Microwave Imaging*, Hoboken, NJ: John Wiley, 2010.

[9] Y. Miura, J. Hirokawa, M. Ando, Y. Shibuya, and G. Yoshida, "Double-Layer Full-Corporate-Feed Hollow-Waveguide Slot Array Antenna in the 60-GHz Band," *IEEE Transactions on Antennas and Propagation,* vol. 59, pp. 2844-2851, 2011.

[10] M. A. Baumgartner, M. T. Ghasr, and R. Zoughi, "Wideband Imaging Array Using Orthogonally Fed Dual Varactor-Loaded Elliptical Slots," *IEEE Transactions on Instrumentation and Measurement,* vol. 64, pp. 740-749, 2015.

[11] Skyworks, "Surface Mount Mixer and Detector Schottky Diodes," ed, 2015.

[12] C. A. Balanis, *Antenna theory : analysis and design*, 3rd ed. Hoboken, NJ: John Wiley, 2005.

[13] D. M. Sheen, "Wide-bandwidth, wide-beam width, high resolution, millimeter wave imaging for concealed weapon detection," vol. Proc. SPIE in Passive and Active Millimeter-Wave Imaging XVI, 31 May 2013 2013.

[14] Analog Devices. (2018, November 4). *ADG1607* [Online]. Avaliable: https://www.analog.com/media/en/technical-documentation/data-sheets/ADG1606_1607.pdf

[15] Hittite Microwave Products. (2018, November 4). *HMC739LP4* [Online]. Available: https://www.analog.com/media/en/technical-documentation/data-sheets/hmc739.pdf

[16] Hittite Microwave Products. (2018, November 4). *HMC863LP4E* [Online]. Available: https://www.analog.com/media/en/technical-documentation/data-sheets/hmc863.pdf

[17] M. J. Horst, "Design of a microwave imaging system for rapid wideband imaging," M.S. Electrical Engineering, Electrical and Computer Engineering, Missouri University of Science and Technology, Missouri University of Science and Technology, 2016.

[18] M. J. Horst, M. T. Ghasr and R. Zoughi, "Effect of Instrument Frequency Uncertainty on Wideband Microwave Synthetic Aperture Radar Images," in *IEEE Transactions on Instrumentation and Measurement*.

[19] M. Fallahpour, J. T. Case, M. T. Ghasr and R. Zoughi, "Piecewise and Wiener Filter-Based SAR Techniques for Monostatic Microwave Imaging of Layered Structures," in *IEEE Transactions on Antennas and Propagation*, vol. 62, no. 1, pp. 282-294, Jan. 2014.

# SECTION

# 2. CONCLUSION AND FUTURE WORK

The research presented in this dissertation formed the necessary foundation to eventually achieve a millimeter wave camera designed for human skin inspection. This research was structured in three research papers. In the first paper, frequency uncertainty in signals generated by a microwave source was studied to determine its effect on SAR-generated images. Previous systems have employed microwave sources (e.g., free-running VCOs) as the microwave signal generator, which are prone to drift in output frequency. It was found that the level of image distortions in SAR-generated images is directly proportional to the product of frequency uncertainty and distance between measurement grid and SUT. Additionally, an HMC733 VCO was measured for its frequency uncertainty, and it was found that the frequency uncertainty of a commonly used VCO, such as the HMC733, will not contributed to visible image distortions for NDT applications.

In the second paper, a SAR-based millimeter wave imaging system was developed forming the basic building block for a millimeter wave imaging system. The system was composed of a transceiver operating in the 58-64 GHz frequency range and an antipodal Vivaldi-style antenna designed specifically for the operating frequency range. The transceiver was based on commercially available system-on-chip transmitters and receivers, and the antenna was designed based on a PCB substrate consisted of a substrate-integrated waveguide, corrugated Vivaldi-style radiators, and a dielectric lens. The system employed the mono-static $\omega$-$k$ SAR algorithm and was used to image a burn on pigskin. For future considerations, the next step of this imaging system is to integrate the transceiver with a switched antenna array with the antipodal Vivaldi-style antenna as the element, thus

creating a millimeter wave camera. Additionally, the dynamic range of the transceiver can be improved with various techniques, namely: electromagnetic interference reduction between transmitter and receiver chips, and direct coupling signal cancellation between transmitting and receiving antenna elements.

Finally, in the last paper, a completely new SAR-based microwave imaging methodology was developed specifically to create microwave cameras that are much smaller and less complex than previous cameras. The imaging methodology, named CESAR, was developed based on all antennas in a planar array transmitting and receiving simultaneously, which is different from the traditional approach of raster scanning a target with one antenna at a time. This methodology allows for much of the RF hardware in a microwave camera to be removed at the cost of image quality. A microwave camera was designed based on CESAR and operated in the 23-25 GHz frequency range. The camera was composed of a 64-element array of rectangular slot antennas fed by a corporate feed waveguide network and cavity dividers. For measuring the reflections from a target, the slots were loaded with Schottky diodes, where the baseband output was routed to data acquisition hardware. Imaging results with the camera showed it was capable of basic feature detection for NDT and security applications.

One of the issues with CESAR is the assumption that the transmitted electric field is an ideal plane-wave. However, the actual radiated electric field resembles a pseudo plane-wave. As a result, images generated with the system have low-level image distortions. For future considerations, the CESAR algorithm can be improved to compensate for the variations in the magnitude and phase of the radiated electric field. Additionally, the algorithm can be improved to compensate for electric field propagation

through multi-layered structures, which would be beneficial for NDT applications. Finally, future investigations will include continued reduction and miniaturization of RF hardware and designing for the next generation of millimeter wave applications.

## REFERENCES


[1] D. M. Pozar, *Microwave engineering*, 3rd ed. Hoboken, NJ: J. Wiley, 2005.

[2] R. Zoughi, *Microwave Non-Destructive Testing and Evaluation*. The Netherlands: Kluwer, 2000.

[3] Y. Chin-Yung and Z. Reza, "A novel microwave method for detection of long surface cracks in metals," *IEEE Transactions on Instrumentation and Measurement*, vol. 43, pp. 719-725, 1994.

[4] C. Huber, H. Abiri, S. I. Ganchev, and R. Zoughi, "Modeling of surface hairline-crack detection in metals under coatings using an open-ended rectangular waveguide," *IEEE Transactions on Microwave Theory and Techniques*, vol. 45, pp. 2049-2057, 1997.

[5] M. T. Ghasr, S. Kharkovsky, R. Zoughi, and R. Austin, "Comparison of near-field millimeter-wave probes for detecting corrosion precursor pitting under paint," *IEEE Transactions on Instrumentation and Measurement*, vol. 54, pp. 1497-1504, 2005.

[6] M. T. Ghasr, B. Carroll, S. Kharkovsky, R. Austin, and R. Zoughi, "Millimeter-Wave Differential Probe for Nondestructive Detection of Corrosion Precursor Pitting," *IEEE Transactions on Instrumentation and Measurement*, vol. 55, pp. 1620-1627, 2006.

[7] S. Kharkovsky, F. L. Hepburn, J. Walker, and R. Zoughi, "Testing of the space shuttle external fuel tank SOFI using near-field and focused millimeter wave nondestructive testing techniques," *Materials Evaluation*, vol. 63, pp. 516-522, May 2005 2005.

[8] J. T. Case, F. L. Hepburn, and R. Zoughi, "Inspection of Spray on Foam Insulation (SOFI) Using Microwave and Millimeter Wave Synthetic Aperture Focusing and Holography," in *Instrumentation and Measurement Technology Conference, 2006. IMTC 2006. Proceedings of the IEEE*, 2006, pp. 2148-2153.

[9] S. Kharkovsky, J. T. Case, M. A. Abou-Khousa, R. Zoughi, and F. L. Hepburn, "Millimeter-wave detection of localized anomalies in the space shuttle external fuel tank insulating foam," *IEEE Transactions on Instrumentation and Measurement*, vol. 55, pp. 1250-1257, 2006.

[10] J. T. Case, M. T. Ghasr, and R. Zoughi, "Optimum Two-Dimensional Uniform Spatial Sampling for Microwave SAR-Based NDE Imaging Systems," *IEEE Transactions on Instrumentation and Measurement*, vol. 60, pp. 3806-3815, 2011.

[11] D. M. Sheen, D. L. McMakin, and T. E. Hall, "Three-dimensional millimeter-wave imaging for concealed weapon detection," *IEEE Transactions on Microwave Theory and Techniques,* vol. 49, pp. 1581-1592, 2001.

[12] M. T. Ghasr, M. A. Abou-Khousa, S. Kharkovsky, R. Zoughi, and D. Pommerenke, "Portable Real-Time Microwave Camera at 24 GHz," *IEEE Transactions on Antennas and Propagation,* vol. 60, pp. 1114-1125, 2012.

[13] M. T. Ghasr, M. J. Horst, M. R. Dvorsky, and R. Zoughi, "Wideband Microwave Camera for Real-Time 3-D Imaging," *IEEE Transactions on Antennas and Propagation,* vol. 65, pp. 258-268, 2017.

[14] Y. Gao and R. Zoughi, "Millimeter Wave Reflectometry and Imaging for Noninvasive Diagnosis of Skin Burn Injuries," *IEEE Transactions on Instrumentation and Measurement,* vol. 66, pp. 77-84, 2017.

[15] F. Topfer and J. Oberhammer, "Millimeter-Wave Tissue Diagnosis: The Most Promising Fields for Medical Applications," *IEEE Microwave Magazine,* vol. 16, pp. 97-113, 2015.

[16] M. A. Abou-Khousa, M. T. Ghasr, S. Kharkovsky, D. Pommerenke, and R. Zoughi, "Modulated Elliptical Slot Antenna for Electric Field Mapping and Microwave Imaging," *IEEE Transactions on Antennas and Propagation,* vol. 59, pp. 733-741, 2011.

[17] J. H. Richmond, "A Modulated Scattering Technique for Measurement of Field Distributions," *IRE Transactions on Microwave Theory and Techniques,* vol. 3, pp. 13-15, 1955.

[18] M. T. Ghasr, M. A. Abou-Khousa, S. Kharkovsky, R. Zoughi, and D. Pommerenke, "A Novel 24 GHz One-Shot, Rapid and Portable Microwave Imaging System," in *Instrumentation and Measurement Technology Conference Proceedings, 2008. IMTC 2008. IEEE*, 2008, pp. 1798-1802.

[19] M. T. Ghasr, S. Kharkovsky, R. Bohnert, B. Hirst, and R. Zoughi, "30 GHz Linear High-Resolution and Rapid Millimeter Wave Imaging System for NDE," *IEEE Transactions on Antennas and Propagation,* vol. 61, pp. 4733-4740, 2013.

[20] M. A. Baumgartner, M. T. Ghasr, and R. Zoughi, "Wideband Imaging Array Using Orthogonally Fed Dual Varactor-Loaded Elliptical Slots," *IEEE Transactions on Instrumentation and Measurement,* vol. 64, pp. 740-749, 2015.

[21] S. Kharkovsky, M. T. Ghasr, K. Kam, R. Zoughi, and M. A. Abou-Khousa, "Microwave resonant out-of-plane fed elliptical slot antenna for imaging applications," in *Instrumentation and Measurement Technology Conference (I2MTC), 2011 IEEE*, 2011, pp. 1-4.

[22] M. T. Ghasr, J. T. Case, and R. Zoughi, "Novel Reflectometer for Millimeter-Wave 3-D Holographic Imaging," *IEEE Transactions on Instrumentation and Measurement*, vol. 63, pp. 1328-1336, 2014.

[23] M. J. Horst, "Design of a microwave imaging system for rapid wideband imaging," M.S. Electrical Engineering, Electrical and Computer Engineering, Missouri University of Science and Technology, Missouri University of Science and Technology, 2016.

[24] Hittite Microwave Products, "HMC733LP4," ed, p. 8.

# VITA

Matthew Jared Horst was born in St. Louis, Missouri and raised in southeast Missouri. He attended Southeast Missouri State University in Fall 2010 for a pre-engineering program. In Fall 2012, he transferred to Missouri University of Science and Technology (Missouri S&T) for a Bachelor's degree in Electrical Engineering. While attending Missouri S&T, he was hired as an undergraduate research assistant at the Applied Microwave Nondestructive Testing Laboratory (*amntl*). He received his Bachelor's degree in Electrical Engineering from Missouri S&T in December 2014.

In January 2015, he began a Master's degree program in Electrical Engineering with *amntl* at Missouri S&T. In April 2015, he was awarded the National Science Foundation Graduate Research Fellowship for pursuing a Master's degree. Matt received his Master's of Science in Electrical Engineering from Missouri S&T in July 2016. In August 2016, he began a doctoral degree program in Electrical Engineering with *amntl* at Missouri S&T. Matt received his PhD degree in Electrical Engineering from Missouri S&T in May 2019.